EVIDENCE FOR THE DYNAMICAL RELEVANCE OF RELATIVE PERIODIC ORBITS IN TURBULENCE

A Dissertation
Presented to
The Academic Faculty

By

Christopher J Crowley

In Partial Fulfillment
of the Requirements for the Degree
Doctor of Philosophy in the
School of Physics

Georgia Institute of Technology

August 2022

EVIDENCE FOR THE DYNAMICAL RELEVANCE OF RELATIVE PERIODIC ORBITS IN TURBULENCE

Thesis committee:

Prof. Michael F. Schatz
School of Physics
Georgia Institute of Technology

Prof. Daniel I Goldman
School of Physics
Georgia Institute of Technology

Prof. Roman O. Grigoriev
School of Physics
Georgia Institute of Technology

Prof. Predrag Cvitanović
School of Physics
Georgia Institute of Technology

Prof. Flavio H. Fenton
School of Physics
Georgia Institute of Technology

Prof. Minami Yoda
School of Mechanical Engineering
Georgia Institute of Technology

Date approved: July 21, 2022

Climbing mountains is pretty easy, step by step, and just don’t let go.

Dan Fries

To Margaret and Joe, my unreasonably supportive parents

ACKNOWLEDGMENTS

Isaac Newton once wrote in a letter to Robert Hooke "If I have seen further it is by standing on the shoulders of Giants." This is absolutely a true statement of my own *minor* progress as well; however, the imagery should be taken further in my case. There is no way I could have done any of the work presented in this thesis without the support of the many people who kept me from falling off those giants shoulders.

First, I would like to thank my advisor Mike Schatz for his patience and optimism. Every time I was 'spinning my wheels' and frustrated, Mike would find a way to help me find traction and insists that I not give up. Mike's support went beyond just trying to keep me moving, he also secured funding for me to design and build a new flow apparatus and outfit it with a very expensive laser. Without his support, this thesis could not have happened. While supporting me with encouragement as well as funding, he also helped expand my understanding of the world and brought me outside the US for the first time. I am very grateful for all he has done. In addition to Mike's support, I would like to thank my (unofficial) co-advisor, Roman Grigoriev. Roman's intuition for physics often made conversations with him a delight. His no-nonsense approach to problem solving pushes everyone around him to be better physicists and made me personally hold myself to a higher standard.

At Georgia Tech, there have been many people who were crucial in my success and I am thankful for each and every one of them. For instance, Predrag Cvitanović seemed to always make the time to explain all the highfalutin theories to a simple plumber like myself. Also, Flavio Fenton kept me well stocked with plenty of Pinguinos and side projects to keep me feeling productive. Numerous times throughout my time at Georgia Tech, Ed Greco has had to listen to me complain about the latest wobble or bubble in my experiment and every time he was there to tell me to get over it, fix the issue, and keep moving. These doses of optimism were often the antidote to my pessimism and without them I may have fallen off track.

Before my advisors at Georgia Tech, I had an amazing group of mentors at the National Institute of Standards and Technology (NIST) where I worked before and during my undergraduate schooling. One of the most influential people in my academic and professional career so far has been Michael Moldover. Mike taught me how to think like a physicist about things both in and out of the lab. Mike is also the reason I decided to attend University of Maryland (UMD). Without his "encouragement" to go to college and take it seriously, I would not have even started at UMD. Beyond twisting my arm to get me to go to school, he seemed to always be there to provide sage advice, kind and encouraging words, or seemingly whatever I needed to not give up. I will be forever thankful for all he has done for me.

In addition to Moldover, there were many other mentors at NIST that help set me up for success. For instance, without Mark Cronise taking a chance on an oddly passionate kid who reportedly misspelled 20% of the words in his job application, I would never have gotten a job at NIST. Without Aaron Johnson and his admirable desire to help people, I would not have had an opportunity to be in a lab. Aaron was also effectively my personal math tutor and without his support, I would have drowned at UMD. John Wright (Much like Mike Schatz) not only was a wonderful mentor on things scientific, but also helped make me a better person. John challenged me to apply the same brain I used in science to all areas of my life which was an invaluable lesson. I worked well with all of the people at NIST, but perhaps Iosif Shinder was a wonderful match. He has an amazing amount of creativity, which made working with him a great delight that gave me the confidence to continue to pursue research.

Along with a large number of people in my professional corner, my family has been incredibly helpful to me. My parents have been incredibly supportive of my endeavours and they are, without question, most responsible for me being where I am today. Similarly, my two brothers have always been there to keep me grounded in reality and have offered magnificent examples of the wonderful success I could have experienced had I not gone to grad school. Above all, my family has been there to keep me able to pursue my passion. My friends Marshall Hamilton, John Indergaard, and James Deitrick, though not legally in my family, are both like brothers to me. Both of them have had to listen to me whine about my experiment not working, my romantic life not working, my regret for going to grad school, or how hot it is even at night in my house without air conditioning more times than is reasonable. Without them, I would have certainly dropped out of gradschool. Along with them, I had several friends such as Benedikt Brandt, Dan Fries, Zac Enderson, and David Jackson that without their friendship gradschool would have been far, far worse than it was. Even with an army of people in my corner, I still benefited greatly from the counseling, care, and general life advice that I got over the years from Kevin Buckins. Kevin's support quite literally kept me sane and without it, I would not be the same person I am today.

The enormous number of people that are responsible for my success is far too great to be able to list here. I am grateful for all of my friends, both in and outside of science.

TABLE OF CONTENTS

LIST OF TABLES

LIST OF FIGURES

LIST OF ACRONYMS

2D-2C two dimensional, two component

3D-3C three dimensional, three component

DNS Direct Numerical Simulations

ECS Exact Coherent Structure

IPS Interpenetrating Spiral flow

KS Kuramoto-Sivashinsky

LDV Laser Doppler Velocimetry

PIV Particle Image Velocimetry

PO Periodic Orbit

PTV Particle Tracking Velocimetry

RPO Relative Periodic Orbit

STB Shake-The-Box

TCF Taylor-Couette flow

tomo PIV Tomographic Particle Image Velocimetry

TS Tollmein-Schlicting

VSC Volume Self-Calibration

SUMMARY

Despite a long and rich history of scientific investigation, fluid turbulence remains one of the most challenging problems in science and engineering. One of the key outstanding questions concerns the role of coherent structures that describe frequently observed patterns embedded in turbulence. It has been suggested, but not proven, that coherent structures correspond to unstable, recurrent solutions of the governing equations of fluid dynamics. In this thesis, I present the first experimental evidence that three-dimensional turbulent flow mimics the spatial and temporal structure of multiple such solutions episodically but repeatedly. These results provide compelling evidence that coherent structures, grounded in the governing equations, can be harnessed to predict how turbulent flows evolve.

To explore this dynamical description of turbulence, experimentally obtained turbulent flow fields in a Taylor-Couette flow apparatus need to be compared to recurrent solutions computed in numerics. To speed up the numerical computation time as well as extend the experimental capabilities, the exploration took place in a small height aspect-ratio regime of Taylor-Couette. Before investigating turbulence, the nature of the turbulent transition was explored in an intermediate height aspect-ratio. The transition to turbulence exhibited a direct, subcritical transition that was mediated by a stable intermediate flow. This intermediate flow resembled the Interpenetrating Spiral flow described in the literature of large height aspect-ratio Taylor-Couette flow, which is spatially ordered, but temporally chaotic. For certain driving parameters, it was found that there was tri-stability between the laminar flow, the temporally chaotic intermediate flow, and turbulence itself. This is perhaps the first experimental observation of a system exhibiting stability of more than one distinct chaotic behaviour for the same parameter values.

In order to turn attention to the dynamical deception of turbulence, a new Taylor-Couette flow apparatus with even smaller height aspect-ratio was constructed. This system was constructed with complete optical access to the entire flow domain. This allows for

direct comparison between numerics and experiment anywhere in the flow domain. The system was designed to be very modular, allowing for changes to the geometry to be easily made. The system was designed to provide full domain measurements of the turbulence simultaneous with torque measurements on both the inner and outer cylinder.

With this system, the first experimental observation that the time dependence of turbulent flow is captured by recurrent solutions was obtained. A framework for describing the time evolution of turbulence in terms of recurrent solutions had previously been discussed in the literature, but much of the work was focused on recovering statistical properties of the flow. The work described here, however, focused on showing that turbulence fleetingly but repeatedly co-evolves with at least one recurrent solution. This co-evolution was found to occur a surprisingly large fraction of time, suggesting this framework may be useful for time-prediction and control of turbulence.

CHAPTER 1

INTRODUCTION

Nearly every flow in the universe is turbulent. Turbulence dominates flows on a vast range of length scales in both naturally occurring and man-made settings. From the spectacular flow within a nebula to the atmospheric jet-streams in weather to the air rushing past a car on the highway to the blood pumping through the aorta with every heartbeat, the flows we interact with and are interested in understanding are all turbulent. Turbulence is the prime source of difficulty in nearly all engineering or scientific endeavors involving fluid flows such as weather prediction, aerodynamic design, and industrial chemical mixing.

Despite the extreme prevalence of turbulence in flows around us, turbulence has remained one of the longest unsolved problems in classical physics. Understanding the complicated motion of an unsteady flow has eluded scientists since the first scientific theory of turbulence was proposed by Leonardo da Vinci more than 500 years ago [1]. Nearly 300 years after da Vinci, the Navier-Stokes (NS) equations were derived, which describe the time rate of change of a fluid's velocity everywhere in the flow [2]. Physicists and mathematicians have been trying to determine ways to solve the NS equations in parameter regimes where turbulence is present. The challenge with the NS equations is that they are nonlinear partial differential equations and the mathematical machinery necessary for dealing with these types of problems is, for the most part, nonexistent.

Most existing approaches to understanding turbulence are statistical ones. Statistical theories brought some success in understanding energy and momentum transport in turbulent flows [3, 4], yet quantitative predictions, even for simple properties such as the pressure drop for turbulent pipe flow, remain elusive and require the use of empirical relations [5]. Statistical approaches tend to assume isotropic and/or highly symmetric flows, neglecting the spatial and temporal structure of turbulence. These approaches treat turbulence as a random fluctuation on top of the mean flow [6]. The fluctuations can be modeled a number of ways [7], but ultimately the stochastic nature of the fluctuations makes understanding the time evolution of turbulence difficult.

Despite the stochastic nature of classical turbulence modeling, experiments have revealed that ordered structures do, in fact, exist within turbulence suggesting it is possible to develop a model based on specific flow patterns. The structures being observed occur often enough that fluid dynamicists are able to reliably identify and name them [8, 9]. These characteristic flow patterns, called Coherent Structures, are regions of the flow that have features that persist for a significant duration of time. Many Coherent Structures have been identified, but two of the most commonly studied are quasi-streamwise rolls [10] and hairpin shaped vortices [11]. There are theories about the role Coherent Structures play in turbulence [12, 13], however they are all phenomenological and are not easily connected to the governing equations.

Recently, a new approach to understanding Coherent Structures in turbulence based on first principals and tied directly to the NS equations has been developed. This new approach relies on numerically computing special solutions to the NS equations and analyzing their dynamics. This approach has emerged from the field of dynamical systems theory and makes use of the observation that, embedded within the complicated dynamics of chaotic systems exist simpler solutions to the governing equations that guide the chaotic dynamics [14, 15, 16, 17, 18, 19, 20, 21]. These special solutions are thought to be the precise solutions to the NS equations that coherent structures observed in turbulence are mimicking [15]. These solutions, in the context of fluid mechanics, are often called Exact Coherent Structure (ECS) and can provide a better understanding of turbulence [22], describing physical mechanisms [16] not captured by statistical distributions. With a sufficient number of ECSs in hand, the time evolution of the turbulence may be approximated.

ECSs provide a direct link between the governing equations and the short-lived patterns frequently observed in turbulent flows. They also make concrete the qualitative picture of turbulence proposed in the 1940s by Eberhard Hopf [23]. Inspired by the work of Poincaré on celestial mechanics and chaos [24], Hopf's picture represents turbulence as co-evolving with (shadowing), one after another, a repertoire of unstable solutions. Shadowing implies that turbulent flow has spatial *and* temporal structure mimicking that of a corresponding unstable solution.

To investigate the use of ECS theory in an experimentally observed turbulent flow, we will be looking at a weakly turbulent flow in a Taylor-Couette geometry. Taylor-Couette flow (TCF) is the flow between two coaxial, independently rotating cylinders (see Figure 1.1). The TCF is ideally suited to study the dynamical systems approach to modeling turbulence because it is able to be investigated in the numerics without approximation or ambiguity (i.e. direct numerical evaluation of the NS equations with the actual physics at the boundary of the TCF cell). Additionally, experimental measurements of the turbulent velocity field can be made over a large portion of the flow domain. To perform analysis in a tractable way, the height aspect-ratio of the flow domain investigated in the work presented here is small. By decreasing the height aspect-ratio, the numerics become less expensive due to fewer grid points needed and, in experiment, a larger portion of the flow domain can be measured.

TCF is typically studied in configurations with cylinders that are very long compared with the annular gap width. In this long cylinder limit, the effects from the ends of the cylinders can be neglected. However, as the height aspect-ratio decreases, the end-effects begin playing a larger and larger role in the flow. The standard intuition for the route to turbulence in TCF changes in the short cylinder limit. The vast majority of the studies in TCF are carried out in the large cylinder limit and only a small number have been conducted in systems where the end-effects cannot be neglected. Before testing the framework for understanding turbulence proposed by Hopf and Poincaré, the small aspect-ratio TCF needs to be investigated.

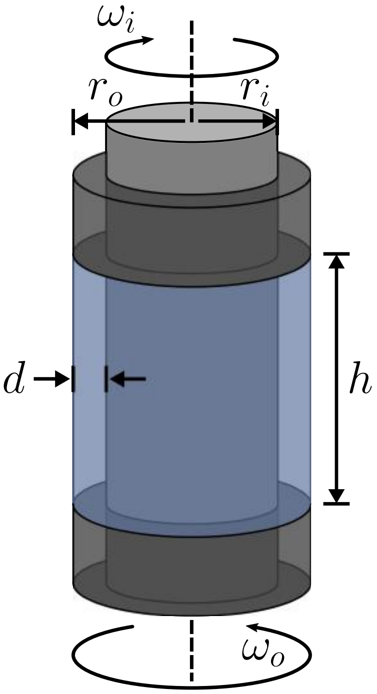

Figure 1.1: In Taylor-Couette flow, a fluid is confined between coaxial cylinders of radii r_i and r_o, which counter-rotate with angular velocities ω_i and ω_o, respectively. In the axial direction, the flow is bounded by two end caps that rotate with the outer cylinder and are separated by a distance h. In the radial direction, the separation between the cylinders is $d = r_o - r_i$. The flow is periodic in the azimuthal direction. Figure taken from Crowley et al (2020)[25].

1.1 Thesis organization

This thesis is organized as follows. In Chapter 2, an introduction to the dynamical systems approach to turbulence is presented along with a brief discussion of TCF and an overview of the image velocimetry techniques employed in this thesis. In Chapter 3, a detailed discussion of the design and construction of a new TCF experimental apparatus is provided. In addition to the design, implementation of an image velocimetry system and the experimental procedure is also discussed. In Chapter 4, an investigation of the unusual nature of the transition into turbulence for a small height aspect-ratio TCF is presented. In Chapter 5, a discussion of some of the first experiments testing the dynamical systems description of turbulence presented by Hopf and Poincaré is given. The framework investigated focuses on the dynamical similarity of turbulence and ECS and an automated similarity detection algorithm is presented. In Chapter 6 provides a discussion of conclusions that may be drawn from this work.

CHAPTER 2

BACKGROUND

In this chapter, a brief overview of three topics relevant to the work in this thesis is given. First, in Section 2.1, a pedestrian discussion of the dynamical systems approach to solving for the dynamics of complicated systems is given. Then, in Section 2.2, a condensed background of TCF literature provided. Lastly, Section 2.3 is a brief introduction to image based velocimetry techniques.

2.1 Dynamical systems theory approach to turbulence

When it comes to solving for the dynamics of a physical system, there are two different mathematical approaches commonly used. One methodology, stemming from Newton's second law, involves deriving a differential equation relating coordinates (e.g. positions and angles) to their second derivatives in time. This methodology is traditionally what is taught in introductory physics courses and therefore informs the intuition of many physicists. There are powerful techniques for deriving these differential equations (e.g. variations techniques accompanied by Euler–Lagrange relations), but often analyzing the resulting equation for complicated systems is difficult. The other methodology investigates a set of coupled, first order differential equations describing the time rate of change each coordinate and its accompanying velocity [26, 27]. That is, an equation for each coordinate and coordinates velocity describing how it changes in time. This second methodology was pioneered by Henri Poincaré in the late 19th century and is a powerful framework for understanding complicated systems [28, 29]. This formalism was largely developed in the context of the three-body problem, nonlinear oscillators, and the ergodic hypothesis [29], but its usefulness is seen across many areas of physics, most notably it is the framework of Hamiltonian Mechanics.

To demonstrate the differences in these two methodologies, consider the example of a simple pendulum confined to a plane. The traditional approach to studying this system would be to write down and investigate the properties of Newton's second law:

$$\ddot{\theta} = -\frac{g}{l}\sin[\theta] \tag{2.1}$$

where g is the local gravitational acceleration and l is the length of the pendulum. The other approach to determine a systems dynamics uses the same coordinates, but instead of deriving equations relating coordinates to their accelerations, a system of differential equations (two in this case) describing how the systems configuration changes in time is written down:

$$\begin{aligned} \dot{\theta} &= v_\theta \\ \dot{v}_\theta &= -\frac{g}{l}\sin[\theta]. \end{aligned} \tag{2.2}$$

Coupled sets of differential equations like these, together with the definition of the coordinates and velocities, is called a *dynamical system* [30, 31]. This second procedure, though mathematically equivalent to the first, is intuitively different and lends itself easily to more powerful analysis techniques.

Expressing the physics in this dynamical systems framework suggests that a natural way of understanding the dynamics is to consider a point moving around in configuration space (i.e. the space of coordinates and their associated velocities). Since the governing equations are expressed as total time derivatives of the coordinates and their velocities, each properly chosen coordinate and velocity can be thought of as its own independent variable [26, 27, 30]. This means that by constructing a space where each dimension is a different coordinate or coordinate velocity, the complete state of the system at an instant in time can be represented as a single point in it. This space is often called[1] "state space" and the governing equations (e.g. Equation 2.2) describe how this point moves in time throughout it.

---

[1] If the dynamical system is Hamiltonian, this space is often also called "phase space."

Each point in state space corresponds to a configuration of the system; however, only a subset of these points correspond to configurations that satisfy the governing equations. Similarly, some configurations would require more energy that the system has at that particular time. Therefore, only the portion of state space satisfying the dynamics is considered. As time evolves, the each point satisfying the governing equations moves along manifolds (curves).

The specific path a trajectory takes is, in general, quite complicated. However, the shape of this curve can be thought of as being 'influenced' by the special geometric objects within state space [14, 32]. When the trajectory is 'near' one of these special objects, the dynamics originating on the object can be used as a proxy for the dynamics of the neighboring trajectory. These geometric objects are closed shapes (e.g. points, loops, tori, and so on), and because they form closed shapes, they are invariant to time evolution[2].

To illustrate how the system behavior in state space is 'guided' by geometrical objects, consider an example of a purely mathematical system: the 2D Lotka-Volterra system [33]. In the Lotka-Volterra, the "coordinates" are the total population of species 1, x_1, and species 2, x_2. The specifics of the dynamical system depend on details of the two species and their interaction. One such system may look like:

$$\begin{aligned} \dot{x}_1 &= x_1 \left(3 - x_1 - 2x_2\right) \\ \dot{x_2} &= x_2 \left(2 - x_1 - x_2\right). \end{aligned} \tag{2.3}$$

In this system, the linear term is exponential growth (i.e. 2 becomes 4 which becomes 8 and so on), the $-x_i^2$ term captures intra-species competition, which prevents the population from growing indefinitely, and the cross-term $-x_1x_2$ captures inter-species competition. By knowing x_1 and x_2 at an instant in time, in principle, the time evolution of the system can be determined for all time. However, as the nonlinearity grows, the evolution of x_1

---

[2] These special geometric objects are also invariant to symmetry operations (e.g. rotation along the axis of a pipe.)

and x_2 can be very complicated and slight changes in the initial known values can result in wildly different time evolution. To see why this may be the case, consider a plot shown in Figure 2.1 where each point in the x_1-x_2 plane represents a different state of the system. The arrows and their spacing on this plot represent which direction and how fast the system will move in the next time instant. Now, consider the situation in which the starting configuration of the system is very close to (but not exactly) at $(x_1, x_2) = (1, 1)$. In the vicinity of this location, the dynamics can be linearized and the directions along which the dynamics push or pull trajectories towards this point (i.e. eigendirections) can be determined. If the initial condition was not on the point $(1, 1)$ or along either of its eigendirections, then depending on which eigenvector it was closest to, the time evolution would race off to different regions of state space.

In state space, the special geometrical objects correspond to key solutions to the governing equations which are simpler in time than the neighboring trajectory. The point (1,1) is an example of one such solution such that if the system is found with that configuration, then it will remain in that configuration as time evolves. These special points are called fixed points and their time evolution is invariant to the dynamics of the system (i.e. they remain unchanged by the dynamical systems governing equation). These invariant solutions to the governing equations help shape the structure of state space. Linearized dynamics in the neighborhood of these invariant solutions generically fall into three types[3]: stable (an attracting solution), unstable (a repelling solution), and a saddle (hyperbolic solution). In Figure 2.1, the equilibrium A is an unstable equilibrium solution that repels all trajectories in its vicinity. Similarly, the equilibrium solutions B and D are stable equilibria that attract nearby trajectories along all directions. The dynamics in the neighborhood of these two types of solutions are relatively simple and as far as dynamics are concerned, boring. The equilibrium solution C, however, attracts trajectories along some directions and repels them along others; this type of solution is a hyperbolic equilibrium (or a saddle). Invariant

---

[3] There is also a fourth type of solution called marginal. These are solutions that neither push nor pull in any direction. These solutions are not particularly common, so they will be left out of the current discussion.

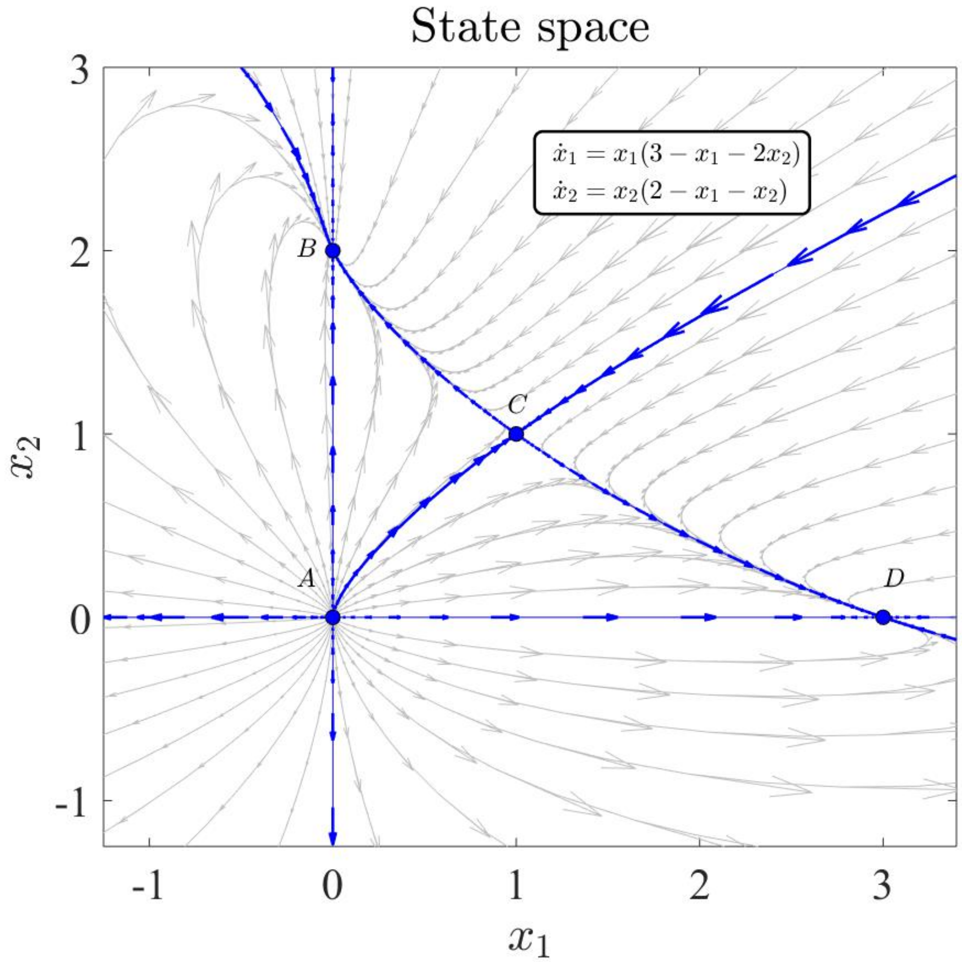

Figure 2.1: Example 2D state space of a nonchaotic flow map. The dynamics shown here are from the Lotka-Volterra (competition model) relations. The equilibrium A is a repeller, while equilibria B and D are attractors and C is a unstable hyperbolic equilibrium (or, saddle). The blue lines with arrows indicating flow direction, are dynamical connections between the solutions.

solutions, in general, are solutions whose dynamics are ‘simple’ (or recurrent) in time. Another common example of an invariant solution is a periodic orbit in which the state returns to itself after a fixed, finite amount of time T (i.e. $x_i(t) = x_i(t + T)$). In general, invariant solutions come in many different topologies, but the present research is only focusing on the simplest of these topologies.

Beyond the solutions themselves, stable/unstable manifolds form dynamical connections linking regions of state space. That is, an initial condition placed along certain unstable directions of an invariant solution will move away from the solution beyond the linear neighborhood and eventually land on the stable direction of another solution. One class of these special curves, known as heteroclinic orbits are shown in blue in Figure 2.1. This means that a trajectory that visits the neighborhood of one hyperbolic unstable solution could get kicked away from it and travel along its unstable direction and continue along its nonlinear extension. If the state space geometry along the heteroclinic orbit is not too unstable itself, the trajectory could travel along the orbit until it reaches the neighborhood of the invariant solution on the other end of the connection. In this way, the invariant solutions not only shape the local geometry of state space, but their connections form a network that ties together different regions of state space. As the dimensionality of state space grows, these lower dimensional entities (i.e. invariant solutions and their connections) are believed to remain the objects that guides the dynamics in state space.

Nonlinear dynamical systems in three or more dimensions[4] can exhibit a phenomenon qualitatively different than what is illustrated in Figure 2.1. Some nonlinear dynamical systems in higher dimensions, exhibit dynamics that are apparently disordered and two initial configurations of the system that look indistinguishable eventually look remarkably different from each other as time evolves. This high degree of complexity is called “chaos” and is the main difficulty with predicting the weather [34], peoples decision making [35], and turbulent evolution [36].

To illustrate chaotic dynamics, consider the Lorenz system, which is an approximate model of atmospheric convection. This model captures the rescaled rate of convection, x, the horizontal temperature variation, y, and the vertical temperature variation, z. The

---

[4] So far the discussion has only been about systems that evolve continuously in time. For discrete systems (i.e. where the next time step is determined from a function of previous time steps) chaos can be observed in systems with only one degree of freedom. In continuous systems, however, the Poincaré-Bendixson theorem implies that chaotic dynamics (or, more specifically a strange attractor) requires more than two dimensions to exist.

model can be written down as:

$$\begin{aligned}\dot{x} &= \sigma\left(y - x\right)\\ \dot{y} &= x\left(\rho - z\right) - y\\ \dot{z} &= xy - \beta z\end{aligned} \tag{2.4}$$

where σ is the rescaled Prandtl number (ratio of thermal to viscous diffusion), ρ is the rescaled Rayleigh number (ratio of thermal transport via diffusion to convection), and β is a quantity that is related to the aspect ratio of the convection rolls. For a given initial condition, the trajectory in state space traces out a figure-eight shaped path[5] that is warped in all three dimensions (See the grey point cloud in Figure 2.3).

The complicated path that a long trajectory takes is also extremely dependant on (sensitive to) the initial condition. If the system starts out with two starting points that are arbitrarily close, over time they will separate and their distance will grow. In Figure 2.2, two trajectories are plotted that started with only a 10^{-2} separation on the x coordinate and the same values for the other two. After about four time units, the trajectories are noticeably different and by about eight time units, the two trajectories are no longer correlated. This extreme dependence on the initial condition means that in order to predict the dynamics of the system, a measurement of the state at the current moment needs to be exactly perfect. Perfect certainty of a measurement is impossible, therefore, systems that exhibit this feature are unpredictable in the traditional sense.

Embedded within the complicated chaotic dynamics, however, are special trajectories that are exactly recurrent in time. These trajectories form closed loops, each called a Periodic Orbit (PO) and their dynamics repeat in time. Figure 2.3 shows the shortest three periodic orbits POs. These POs are conceptually the same as the fixed points in the Lotka-

---

[5] The path resembles Mario Kart's Rainbow Road more than a Formula 1 track. The path of a long trajectory looks like a different figure-eight track depending on the angle it is viewed from. To get a good sense of what the long chaotic trajectory looks like, it needs to be viewed from multiple angles. Additionally, the Lorenz system is not 'structurally stable,' meaning that the shape of a long chaotic trajectory in state space depends on the parameters (i.e. σ, ρ, and β).

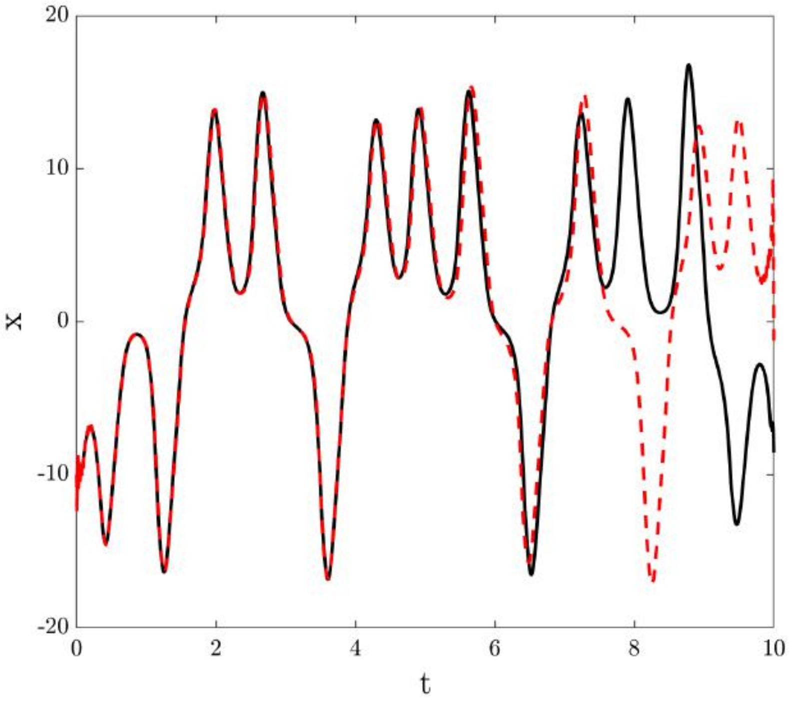

Figure 2.2: Example of sensitive dependence shown in the time series of x coordinate of the Lorenz system . In black is a trajectory starting with a state space location of $(x, y, z) = (10, 0.5, 10)$. The red dashed curve is a trajectory started out at a very close initial location of $(x, y, z) = (10.001, 0.5, 10)$. Note that after about 8 time units, the two trajectories look nothing alike. This figure was computed for a Lorenz system with $\sigma = 10$, $\rho = 28$, and $\beta = 5/8$.

Volterra, but they now have time-dependance. Just like in the 2D example, they have attracting and repelling dimensions, but instead of being described by simple vectors, they are more complicated directions that are parameterized along the orbit. Though the dynamics are complicated, there remains some semblance of the same order that was seen in the nonchaotic example above.

In dynamical systems theory, there is a rigorous proof that for "uniformly hyperbolic" dynamical systems, there are an infinite number of POs and a chaotic trajectory is always infinitesimally close to one of these POs [37]. The Lorenz system, strictly speaking, is not hyperbolic everywhere [38]; however, it has been proven that the system is chaotic and therefore has an infinite number of POs [38, 39, 40]. With a large number of POs embedded within the complexity, the statistics of the chaotic dynamics (e.g. averages and probability distributions) can be described in terms of an expansion of the POs [41]. All 10^6 POs whose period is less than or equal to 20 have been found numerically [42], which makes this expansion practically accessible in this system. In addition to the statistics, POs can be used to approximate the dynamics itself by developing a probabilistic progression from mimicking one solution to another, then another [43]. Unfortunately, as the dimensionality of state space increases, many of the tools developed in systems like the Lorenz are of little use; however, the presence of POs remains.

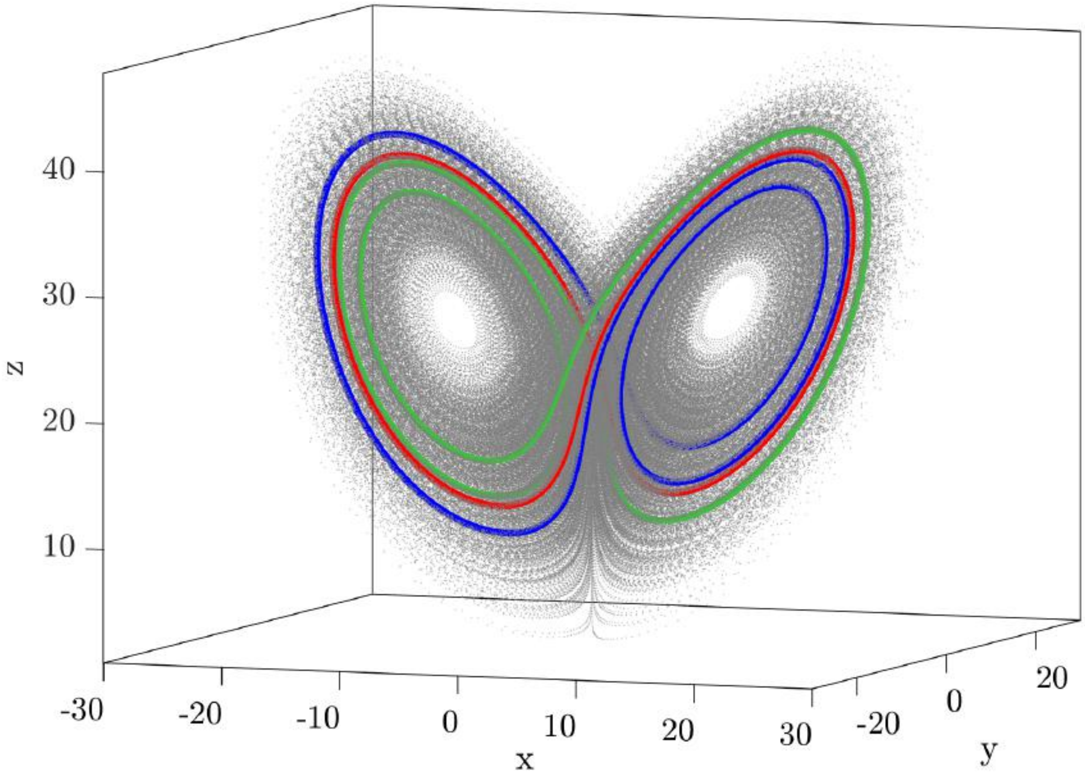

Figure 2.3: The Lorenz attractor (grey) has embedded in it, trajectories that are periodic in time, called periodic orbits. The three simplest periodic orbits are plotted. The three (i.e. red, green, and blue) curves ploted are the three shortest POs. This figure was computed for a Lorenz system with $\sigma = 10$, $\rho = 28$, and $\beta = 5/8$.

For a fluid, every fluid element in the flow has its own velocity. This means that describing its dynamics requires a coordinate and velocity for every point in the flow. The resulting state space is very high dimensional. In principal, a fluid is a continuum of fluid elements and thus would need an infinite number of coordinates and velocities and therefore an ∞-dimensional state space. In practice, however, viscosity causes structures with short length scales to dissipate very quickly. This means that there is a smallest length scale, set by the viscosity, that is relevant in the fluid flow so state space does not need to be ∞-dimensional, but rather, just a very large number of dimensions [44].

Many dynamical systems, with both high- and low-dimensionality, also exhibit other, more complicated closed structures such as tori (donut shaped surfaces). These more complicated structures can arise various ways, but one of the most important ways is through symmetries of the system. Intuitively these shapes are easy to understand if you imagine a system with a continuous symmetry such as a system in a circular domain. Since the system is equivalent if the system is rotated along the azimuth, a periodic structure can also have a drift along this dimension and still remain a solution to the governing equations. The shape of this solution in state space would be a closed loop smeared along the direction corresponding to the azimuthal rotation, forming a closed tube-like structure. These higher dimensional structures can be generalized to just closed structures (sets) in state space that are invariant to time evolution (i.e. points on the structure remain on the structure forever) and to symmetry operations (i.e. a translation along the symmetry direction keeps it on the structure).

The invariant solutions in the high dimensional state space describing a fluid corresponds to flow patterns in the 3D physical space the fluid lives in [15, 16, 17, 18, 19, 20, 21, 45]. These special flow patterns are the ECS discussed in Chapter 1. They are unstable flows, similar to the POs in the Lorenz example above, and therefore will not be exactly present in a turbulent flow, but the turbulent flow may come near to them in state space temporarily. This means that a turbulent flow will fleetingly resemble one ECS then another as seen in the cartoon in Figure 2.4. A primary objective of the proposed work in this thesis is to test this conjecture about the role of ECS in laboratory turbulence that takes place in three spatial dimensions—specifically, in the turbulent flow between rotating cylinders–turbulent Taylor-Couette flow.

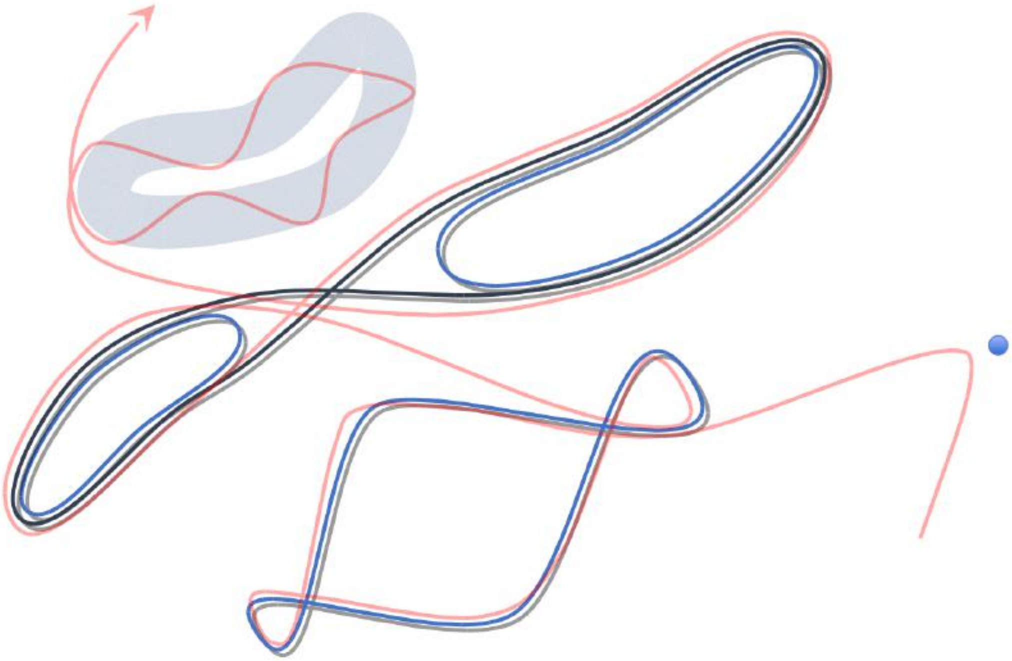

Figure 2.4: A schematic representation of the hierarchy of state space structures. The red curve represents a turbulent trajectory and the blue structures represent ECS; an equilibrium (dot), POs (loops), Relative Periodic Orbit (RPO) (torus), etc.

2.2 Taylor-Couette flow

Taylor-Couette flow, or the flow between two coaxial, independently rotating cylinders (see Figure 1.1), is can be characterised by its geometric and fluid properties. Specifically, TCF can be uniquely characterized by four nondimensional parameters. Two parameters characterize the geometry of the system: the radius ratio $\eta = r_i/r_o$, where r_i and r_o are the radii of the inner and outer cylinders, respectively, and the aspect ratio $\Gamma = h/d$, where $d = r_o - r_i$ is the radial separation distance between the cylinders and h is the axial height of the flow domain. The other two parameters, the inner and outer Reynolds numbers $Re_{\mathrm{i,o}}$, describe the cylinders' rotation rates and are given by[6]

$$Re_{i,o} = \frac{r_{i,o}\,\omega_{i,o}\,d}{\nu}, \tag{2.5}$$

where ν is the kinematic viscosity of the fluid and $\omega_{i,o}$ are the angular velocities of the inner and outer cylinders, respectively. By convention Re_{i} is always taken to be positive, whereas Re_{o} is positive when the cylinders are co-rotating and negative when they are counter-rotating.

Centrifugal effects can cause the flow to become unstable. If the inner cylinder rotates, there will be a centrifugal force acting on the fluid. If the radial pressure gradient is greater than or equal to this force, a fluid element displaced in the radial direction experiences a restoring force and the fluid flow is stabilized. If, however, the pressure gradient cannot balance the centrifugal force, a fluid element displaced in the radial direction will not experience a restoring force, but instead, continue to be forced away from its original position. This criterion for stability is known as the Rayleigh criterion [46, 47] and if the fluid does not meet this criterion it is considered to be centrifugally unstable. In TCF this criterion works out to be $Re_{\mathrm{i}} \geq \frac{1}{\eta} Re_{\mathrm{o}}$ for the base flow. This criterion, however, implies that for a stationary outer cylinder and just a very slow inner cylinder rotation, the base flow would be unstable. The Rayleigh criterion neglects viscosity which was found by Taylor to have a stabilizing effect [48]. Using linear stability analysis Taylor calculated when the base flow becomes unsteady as a function of Re_{o} and Re_i. This calculation also showed that the base flow was stable for all values of Re_{o} and a stationary inner cylinder.

When the cylinders' rotation rates increase beyond the initial stability threshold, additional instabilities cause the formation of numerous different, non-turbulent flow states. These flow states were first predicted and experimentally studied by G. I. Taylor in is seminal paper published in 1923 [48]. Taylor investigated these flow states by photographing

---

[6] There are several definitions of the Reynolds number used in the literature, but for the entire discussion in this thesis, the Reynolds number defined by the cylinder walls velocity is used.

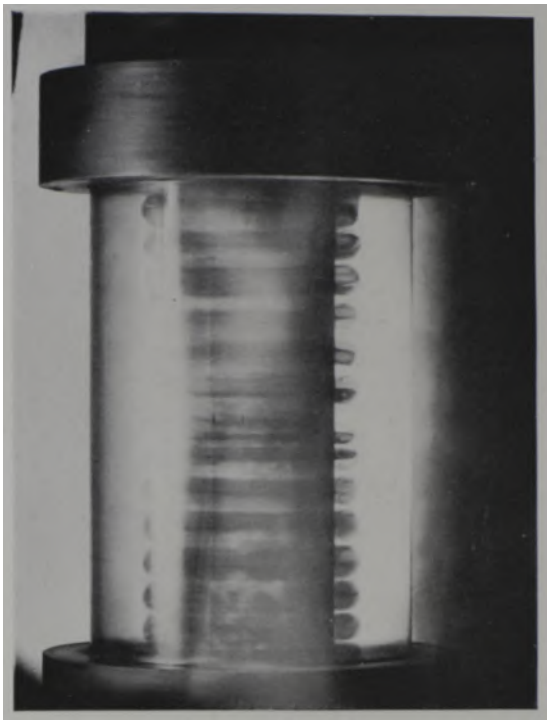

Figure 2.5: Photograph of streamlines of a stable flow state discovered by G. I. Taylor. This flow state, now referred to as Taylor Rolls, is stable when the inner cylinder is rotated above a critical rotation rate and the outer cylinder is held at rest. The flow structure seen is visualized by dye injected into the flow. This figure is taken from G. I. Taylor 1923 [48].

the stream lines traced out by fluorescent dye injected into the flow (an example photograph is shown in Figure 2.5). In Taylor's own words, when implementing this technique "considerable difficulty was experienced," a phenomenon observed by nearly every graduate student working in this system to this day. In 1956, to further understand what was going on within the flow, Schultz-Grunow and Hein seeded the flow with aluminum flakes they extracted from hammer paint [49]. Due to their anisotropic shape, the aluminum flakes preferentially align with the gradient in the flow resulting in regions of the flow that reflect more or less light depending on the local gradient in the flow. This technique allowed Schultz-Grunow and Hein to visualize transitions in the flow beyond the initial stability threshold. This same technique was later used by Andereck et al (1986)[50] to discover a myriad of stable, non-turbulent flow states (see Figure 2.6 for examples) for different rotation rates (see Figure 2.7). This flow visualisation technique has come to be known as rheoscopic flow visualization with modern experiments being carried out very similarly with the use of more neutrally buoyant particles [51].

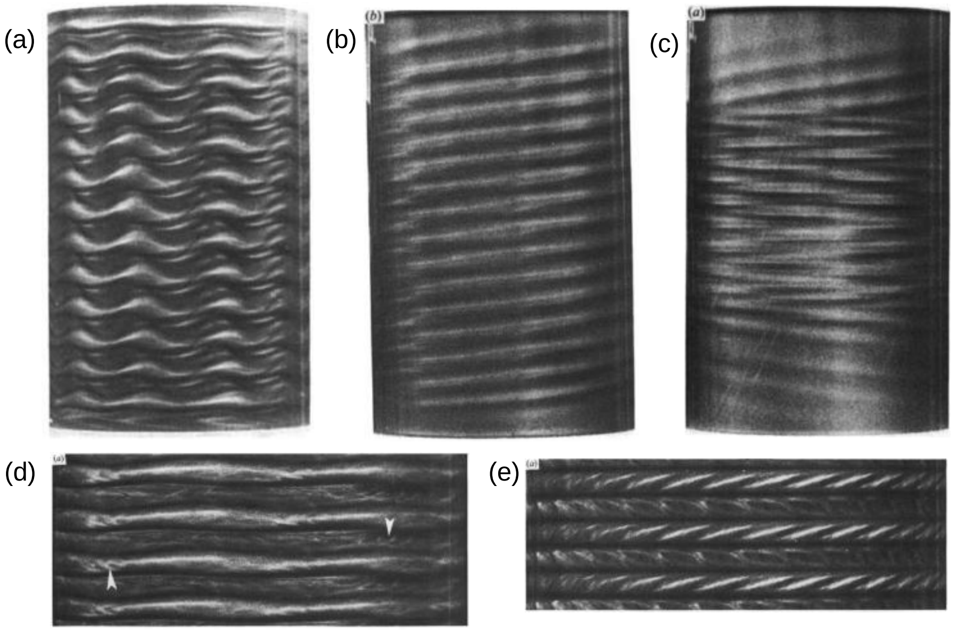

Figure 2.6: Example flow visualizations of non-turbulent stable flow states observed in TCF. (a) Modulated wavy vortex flow. (b) Laminar spiral flow. (c) Interpenetrating spiral flow. (d) Rippled wavy-Taylor-vortex flow with arrows pointing to the ripples. (e) Twisted Taylor vertices. To see what values of Re these flow states occur, refer to Figure 2.7. These images are taken from Ref. [50].

When the rotation rates are sufficiently fast, the flow transitions into turbulence through one of two ways: either through a series of intermediate, non-turbulent states, or directly from laminar. TCF has mostly only been studied in the large Γ limit with inner cylinder rotation dominating. The transition to turbulence in the large Γ limit is not directly from laminar, but instead the flow passes through a series of stable flow states. Perhaps the most famous turbulent transition in TCF is when the outer cylinder is at rest and the inner cylinder is rotated. In this transition scenario, first there are several transition into non-turbulent flows that can be characterized by distinct frequency spectral lines, then as the Reynolds number continues to be increased, discrete spectral peaks suddenly disappear as the flow transitions into turbulence[7] [52]. If the outer cylinder is also rotated, the turbulence that

---

[7] This was the first experimental demonstration that the Landau theory of turbulence was incorrect [52].

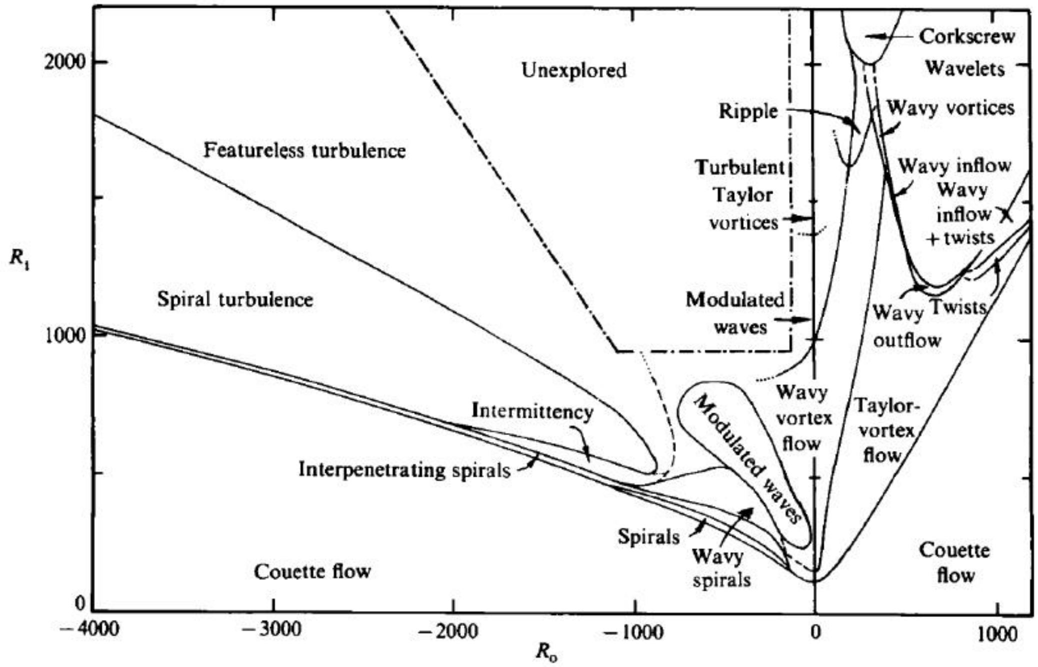

Figure 2.7: Flow state transition map for a TCF with a large Γ and $\eta = 0.883$. The horizontal axis corresponds to Re_o and the vertical corresponds to Re_i. This diagram was generated by first setting the Re_o, then quasi-statically increasing Re_i and recording when the transition occurred. This figure comes from [50].

is present exhibits spatio-temporal intermittency [53, 54]. This type of turbulent transition that occurs after a series of non-turbulent flow states is unlike the turbulent transition observed in most shear driven flows such as in pipes or over an airplane wing which is directly from laminar. Because of this, TCF turbulence is not often studied in the transitional region; it is typically studied in the high Re regime where the transition dynamics are not important [55, 56, 57].

TCF also does exhibit turbulent transitions that are directly from laminar, akin to those observed in wall-bounded shear flows. If, for example, the outer cylinder rotation dominates, linear stability analysis of the symmetric flow suggests that no transition will occur. At sufficiently high Re_o a spontaneous transition to turbulence is observed [58, 59, 60]. This transition is not due to the change in stability of a base flow, but rather due to the nonlinear growth of finite amplitude disturbances. These studies have all been in systems with a large Γ where end effects from the top and bottom end caps can mostly be ignored.

The small Γ regime is important in the work investigated here, however, little is known about how TC becomes turbulent in small Γ systems. In order to make comparisons between fully resolved numerical simulations with the same boundary conditions as in the experiment, the flow domain must be small to enable tractable calculations. In the discussion above, the description of turbulence has focused on the regime where the aspect ratio is large. There have been few studies focused on turbulence when Γ is small. In the small-aspect-ratio regime ($\Gamma \approx 1$) of TCF, there have been several studies with stationary outer cylinder and rotating inner cylinder [61, 62, 63, 64, 65, 66, 67, 68, 69]; however, only one study examines the co- and counter-rotating scenarios [70], and none investigate turbulence. As Γ decreases, the end effects begin playing a more substantial role in the dynamics and the overall picture changes. The presence of the top and bottom end caps result in a global secondary flow in the r-z plane analogous to geophysical Ekman circulation. This secondary flow acts to redistribute angular momentum and as Γ becomes small, this happens so much that the base flow no longer resembles the base flow in the large Γ system. The transition away from the laminar base flow occurs at a larger value of Re_i as Γ decreases [71]. An exploration of how this transition changes for a system with a small Γ is presented in Chapter 4.

Much of the understanding of TCF discussed so far has relied heavily on the intuition afforded to researchers by flow visualization. In order to test the dynamical systems description of turbulence described in Section 2.1, a more quantitative observation technique is needed.

2.3 Overview of velocimetry techniques

2.3.1 Velocimetry

The discussion of fluid dynamics experiments so far has largely relied on qualitative observations of the flow, mostly using rheoscopic flow visualization techniques[8] However, a technique is needed to capture quantitatively, the time-resolved, instantaneous state of a turbulent flow that is present in the dynamical systems picture of turbulence. There are numerous quantitative measurement techniques that offer velocity information about the flow.

Quantitative flow velocimetry techniques can be split up into two categories: techniques where the velocity is either inferred from measurements of intrinsic fluid properties or measurements of movement of tracer particles dispersed in the fluid. Techniques based on intrinsic fluid properties measure, for instance, the fluid's instantaneous pressure (e.g. pitot tubes), the ability for the fluid to absorb heat (e.g. hot-wire), the speed of sound (e.g. acoustic techniques), or the index of refraction (e.g. schlieren). These techniques typically obtain time dependant velocity information that is localized in space which requires approximations to extrapolate to obtain a spatially extended flow state. Additionally, many of these techniques require physically inserting a device into the flow, thereby interacting with the flow [72]. Though, many of the techniques that use tracer particles, obtain spatially localized velocity information (e.g. LDV and acoustic particle Doppler) as well, there are tracer based techniques which rely on imaging the instantaneous distribution of particle locations via a camera. There are numerous image velocimetry techniques such as Optical Flow [73], Motion Magnification [74], Particle Tracking Velocimetry (PTV) [75], and Particle Image Velocimetry (PIV) [76]. Because image velocimetry techniques offer instantaneous, spatially extended velocity information, they are ideal candidates for exper-

---

[8] Even the famous Gollub and Swinney result demonstrating the Landau theory of turbulence is incorrect analyzed time series data of light passing through the rheoscopic flow visualization seeding in their apparatus [52].

iments exploring the dynamical systems description of turbulence. The work discussed in this proposal will utilize several variants of PIV.

PIV is a measurement technique where successive images of flows that have been seeded with tracer particles are analyzed in order to obtain particle displacements. The displacement of the tracer particles are assumed to track well with the fluid volume surrounding the particle. There are many considerations that need to be thought of before implementing this technique and are discussed in many useful books [77, 78]. A successive pair of images obtained from a camera capture light intensity distributions from the flow impinging on the cameras' sensors at two neighboring instants in time. PIV does not capture the specific locations of individual particles, but instead, works entirely with the light intensity field obtained on the camera image.

Regardless of the implementation, all PIV algorithms operate on the same principle. The PIV algorithm splits the light intensity distribution from the flow at one instant in time up into sub-regions and performs a cross-correlation of that sub-region with the full light intensity distribution obtained in the next instant in time in order to determine the light intensity patterns' local spatial shift. The standard implementation of PIV relies on the particle pattern – and therefore the light pattern – remaining largely undeformed between two frames with only a lateral shift between them.

Since particles seeded in a 3D flow will be distributed throughout the whole 3D volume, the location of the particles in the dimension perpendicular to the image needs to be known in order to obtain accurate particle displacement. Without this additional spatial information, there is no way to obtain a coherent light intensity pattern displacement. Obtaining the additional spacial information can be achieved in several different ways. In the following subsections two of these methods will be discussed; one method to obtain the two components of velocity within a two dimensional sheet (two dimensional, two component (2D-2C)) and a method to obtain the full three components of velocity in the full flow volume.

2.3.2 Two dimensional, planar PIV (2D-2C)

In 2D-2C PIV, the particles being used to probe the velocity field are confined to a single plane (or, thin curved surface in some cases [79]) typically by confining the illuminating light to a thin sheet. With only a single plane of particles being illuminated, the camera can be setup perpendicular to this illumination sheet, removing the ambiguity of the particles position in the third dimension. Two successive images obtained in this way can be directly split into sub-regions and cross-correlations performed in the standard PIV implementation. Like with any PIV algorithm, the quality of the input images is crucial. High quality images can be obtained by image preprocessing where filters are implemented to enhance signal-to-noise ratios of the particles. The highest quality PIV occurs when the raw images themselves have high a signal-to-noise ratio which can be achieved with careful setup of the illuminating optics. For best results with PIV, the images will have uniform lighting, clear separation between particle and background intensities, and particle intensities that remain constant in time (e.g. they are not anisotropic and tumbling or moving perpendicular through the light sheet).

By establishing the plane by simply cropping the illuminating light into a sheet, particles are only illuminated when they are in the light sheet and therefore will only contribute to the correlations when they are in the plane. As long as the velocity is mostly in line with the plane, then particles will remain in the illumination long enough for a correlation to be determined. If, however, there is a substantial component of the velocity perpendicular to the plane, particles will appear and disappear on the image in a seemingly random way making a correlation impossible. This can be mitigated by either increasing the thickness of the light sheet, aligning the illumination plane with the maximum velocity, or by increasing the frame rate of the camera.

2.3.3 Three dimensional tomographic PIV

Tomographic Particle Image Velocimetry (tomo PIV) is a velocimetry technique where a 3D volume of light intensity is first reconstructed, then 3D cross-correlations are carried out to find the most likely displacement. In tomo PIV, multiple cameras simultaneously image a particle seeded flow from various angles. A 3D light intensity distribution is then calculated from these images using an iterative reconstruction algorithm [80, 81]. A 3D cross-correlation is then performed against two successive in time subregions of the reconstructed intensity field and a 3D grid of 3-component velocity vectors are produced [82]. If the density of particles on each individual image is too high, the reconstruction algorithm will produce erroneous peaks in the reconstructed field called ghost particles. Since these ghost particles have nothing to do with the flow and are just artifacts of the reconstruction, they diminish the quality of the measurement. As the seeding density is increased the number of ghost particles also increases [83] and in practice the highest seeding density that is possible for tomo PIV is about 0.5 particles per pixel [81].

Though tomo PIV is a high fidelity technique, it is a few serious draw backs. tomo PIV is a high quality technique for computing 3D velocity fields; however, it requires not only reconstructing a 3D intensity array at each timestep, but it also requires performing many cross-correlations in the 3D space. These calculations are demanding, requiring a lot of computational power to determine a single snapshot in time, let alone an entire time series. Similarly, each snapshot in time produces a 3D array of velocity measurements which takes up a lot of disk space and is cumbersome to analyze. If adequate computational power is available, there are still drawbacks such as the increased noise from ghost particles [82] and by representing the light intensity field on a 3D gridded voxel space, there are discretization errors on the particles locations [81] Additionally, cross-correlation applies spatial averages over the subregion volumes and therefore smooths out velocity gradients and fine flow structures. This effect can be slightly mitigated with the use of Gaussian [84] or adaptive [85] weighting in the correlation process, but cannot be fully removed.

CHAPTER 3

A NEW TAYLOR-COUETTE FLOW APPARATUS

TCF has become one of the most studied flow geometries in fluid research, making it one of the canonical geometries along side Rayleigh–Bénard convection, plane-Couette flow, channel flow, and pipe flow. Over the years there have been many TCF apparatuses designed and built, from ones whose cylinders are driven by torsion wires [86] to ones driven with powerful electric motors coupled through gear boxes producing incredible rotation rates [87, 88]. The long and rich history of TCF apparatus designs and their uses is covered in more detail by Daniel Borrero-Echeverry [89] and by Donnelly [86] but of little relevance to the work here.

Most TCF apparatuses are designed with investigating idealized, centrifugally driven flows in mind and, therefore, attempts to mitigate the finite size effects introduced by the axial end caps. Many designs achieve this by making the axial extent of the system much larger than the annular gap width.[1] However, there are questions that are ideally studied in a closed, three dimensional flow with a continuous symmetry that are not affected by the end effects. This flexibility allows for a flow domain with a short axial extent that both makes full flow domain numerical investigation more tractable as well as allowing for measurements over the entire flow domain.

In the past two decades there has been tremendous advancement in multi-view, image based velocimetry techniques. To fully make use of these techniques, an experiment should be designed with this in mind. Modern image velocimetry techniques are capable of providing time-resolved, high fidelity three dimensional velocity fields in a volume [91, 92, 93]. To achieve this, they use cameras viewing tracer particles dispersed in the flow from

---

[1] There are also ambitious designs that attempt to remove end effects with split end caps, allowing for a more complicated boundary condition [90].

several points of view. To maximize the volume these techniques operate over, there are two main considerations: (1) optical access to the flow from many unique angles should be maximized and (2) the depth of field of the cameras should be large enough that the region of overlapping focus is maximized. Constructing a TCF cell with completely transparent cylinders and end caps, this allows for the flow domain to be imaged either from the top or bottom. If the axial extent of the flow domain is the same size or smaller than the depth of field of the cameras, velocimetry can be carried out in the entire flow domain.

The TCF design described in this chapter is focused on investigating a dynamical systems description of turbulence, however, versatility for use with future research is also kept in mind. To be useful for dynamical systems studies, this system needed to allow for large portions of the flow to be measured simultaneously, minimizing the reliance on data extrapolation techniques such as Taylor's frozen turbulence approximation when making comparisons to numerics performed in the entire flow domain. Additionally, the flow domain needed to be small, making computation less time-consuming. These considerations led to the development of a TCF with very short axial extent compared to typical TCF geometries. To allow for versatility, there were several design choices that needed to be made such as the drive shafts allowing for incorporation of torque sensors and the material of the cylinders and end-caps allow for easy, inexpensive modification.

The rest of this chapter is organized as follows: Section 3.1 describes the design and construction of the TCF apparatus. Section 3.2 describes the design and implementation of the image-based velocimetry techniques. Section 3.3 lays out a procedure for setting up, running, and analyzing raw data from the system.

3.1 Design and construction of the apparatus

3.1.1 The TCF cell

A new TCF[2] experimental system was designed and built with the unusual quality of complete transparency, giving optical access to the full turbulent flow. This makes possible, for the first time in TCF, direct comparison of measurements anywhere in the flow domain with theoretical/numerical predictions. All surfaces bounding the flow (cylinders and axial end caps) were constructed out of transparent acrylic, precision-built in-house and hand polished to optical quality. The cell was built with a radius ratio of $\eta = 0.71$ and height aspect ratio of $\Gamma = 1$; however, its design allows for relatively easy exchange of cylinders, which provides the possibility of a wide variety of η and Γ configurations.

The specific dimensions the cell were chosen in order to optimize several design criteria. First and foremost, the dimensions of the cylinders were chosen to minimize the frame rate of the image acquisition system by decreasing the maximum velocity scale. This significantly reduces the cost and increases the easy of assembly of the image acquisition system for velocimetry described in subsection 3.2.3. The outer cylinder's radius was also chosen so that it took up nearly the full field of view of the cameras in the image acquisition system. The outer cylinder's size was also restricted to ensure that the entire flow domain could fit inside of the depth of field of the cameras viewing from an angle of 30° without the use of a Scheimpflug lens mount, further decreasing cost and increasing simplicity of implementation. By comparing costs of the parts to build the velocimetry system for different size cells, the dimensions that best satisfied these criteria while also minimized cost were an inner cylinder radius of 50 mm and an outer cylinder radius of 70.42 mm. Using the aforementioned acquisition system, the dimensions of the cylinders allow for velocimetry

---

[2] Predrag Cvitonavić suggested the name "Taylor-Couette duct flow" to describe the geometry of the new system. He said this because the geometry is a square duct wrapped onto itself. Since the end-effects are a dominant contributor to the flow, the intuition gained from larger aspect-ratio Taylor-Couette systems is of little use and giving this geometry a unique name may be helpful.

measurements up to a maximum Reynolds number $Re_{\text{max}} \approx 4300$ on either cylinder.[3]

The choice of material to fabricate the TCF cell was guided by three criteria: low refractive index, optical transparency, and ease of construction. Constructing the cell out of glass was ruled out due to the difficulty associated with manufacturing a cell with symmetry along the rotation axis. Fusing the endcaps to the cylinder wall would likely cause the cylinder wall to bend slightly.[4] Therefore, constructing the cell from plastic was all that was left if we were to avoid using seals, which would obstruct the view of the flow domain. There are number of transparent plastics (e.g. SMMA, PET, PETG, and ABS), but polycarbonate (PC or Lexan) and poly(methyl methacrylate) (PMMA or acrylic) stand out on the list. Most other transparent plastics either are not rigid, too hazy, or their index or refraction is too high. PC is easier to machine than PMMA, but PMMA has a refractive index of 1.49 while PC has a refractive index of 1.58. PMMA has the added benefit that it is relatively easy to polish, making it the obvious best choice.

The specific value of refractive index n of PMMA, however, varies from batch to batch [94] due to slight variations in the specific conditions present while the polymer cures. Therefore, to allow for the best refractive index matching, the entire cell was constructed from the same block of PMMA. The quality of the PMMA is important, so a 4 in×12 in×24 in slab of PMMA was purchased from ePlastics (San Diego, CA), an online plastics manufacturer.

Figure 3.1 shows a CAD model of the cell. The top and bottom end caps are attached to the outer cylinder and, together with the outer cylinder wall, form the enclosure containing the working fluid. The outer cylinder's shaft attaches to the top cap which is attached to outer cylinder by a flange. The working fluid is kept from leaking out of the cell by a rubber O-ring seal in the flange.[5] A tight tolerance pocked was made in the flange on the top cap

---

[3] This Re_{max} was calculated assuming a max particle displacement of 8 px and a nominal kinematic viscosity of 1.5 $\text{mm}^2 \cdot \text{s}^{-1}$ as described in subsection 3.2.2. If either a lower viscosity fluid is used or a larger particle displacement is acceptable, Re_{max} could be increased.

[4] It may be possible to construct the cell out of glass, but after consulting with the Glass Shop in the Georgia Tech chemistry department, it was decided that it was too challenging to pursue a glass cell.

[5] The seal was chosen to be a Nitrile (Buna-N) rubber O-ring with a 152.07 mm inner diameter (ISO 3601

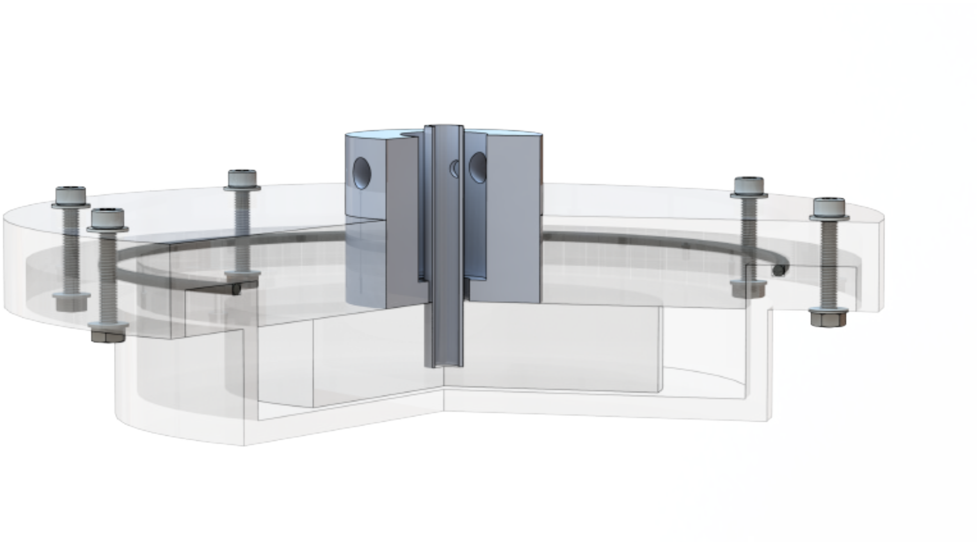

Figure 3.1: CAD model of the TCF cell. The cell is made of transparent PMMA allowing for unobstructed, optical access to the entire flow domain. 316 stainless steal shaft sleeves are pressed into outer cylinder top cap and the inner cylinder.

for the outer cylinder to fit in, ensuring it remain coaxial with the top cap.

Though PMMA is a relatively rigid plastic, with repeated disassembly/assembly its dimensions can change. In our system, this manifests as a slight wobble of the cylinders due to the shaft no longer fitting properly in the hole. To avoid this, 316 stainless steal[6] metal shaft sleves are pressed (with a 50 µm press fit) into the plastic. To avoid cracking the plastic and to ensure perpendicularity, the metal receivers were chilled in an acetone and dry ice bath, then inserted with ease. For the outer cylinder top cap, the receiver and end cap were placed on a granite slab and allowed to warm back up, ensuring the two faces were flush and parallel. Mechanical drawings for the components of the cell can be found in Section D.3.

#163). The groove it sits in was designed to provide a 4 % compression.

[6] The ammonium thiocyanate based working fluid is extremely reactive with ferrous alloys as well as a few other metals (e.g. brass and copper). Aluminum holds up well against the working fluids corrosion, but it was found to be too soft to be used as the shaft sleves. 316 stainless steal is chosen for its resistance to corrosion from the working fluid and its rigidity, but the working fluid nevertheless causes pitting to these parts over time.

3.1.2 Driving

The cylinders are rotated under computer control using two high-performance stepper motors. Both motors are five-phase stepper motors with 125000 steps per revolution (Oriental Motor Co. LTD, Tokyo, Japan, model PKP544N18A).[7] The motors are controlled by universal stepper controllers (Oriental Motor, model SCX11), which are programmed over a serial port. Each controller drives the motors with a Oriental Motor driver model CVD518-k that can provide 1.8 A per phase. All together, this driving setup provides a constant rotation rate from 0 Hz to 595 Hz with a max torque of 0.2542 N·m at low rotation rates, dropping to 0.05 N·m as the rate reaches its maximum.

The motors are coupled to the cylinder shafts via timing belts to minimize the already small vibrations introduced by the motors. The timing belts are fitted onto pulleys which allow for the possibility of driving the cylinders with mechanical advantage. The current configuration provides a gear ratio of 4:1, further minimizing vibrations from the motors' steps. The belts and pulleys are T-series[8] timing belt/pulleys purchased from McMastar-Carr (McMaster-Carr Supply Co., Elmhurst, Illinois).

This driving assembly is able to provide near constant rotation over a wide range of rotation rates with relatively fine resolution in rotation rate. The SCX11 controllers have an output frequency resolution of 1 Hz which corresponds to a motor rotation rate resolution of 0.0288 Hz. With the gear ratio of 4:1 provided by the pulleys, the driving is able to control the cylinders rotation rates to a resolution of 0.0072 Hz.

3.1.3 Split shaft for *in situ* torque measurements

Angular momentum transport plays a key roll in many flows. A better understanding of angular momentum transport has implications in understanding how galaxies form [95], the formation of compact objects [96], and predicting the persistence of tropical storms [97],

---

[7] The factory default is 500 steps per revolution, but with five-phase driving and "microsteping," they can achieve 125000 steps per revolution.

[8] The belts and pulleys are 10 mm wide and have a pitch of 5 mm.

to mention a few. The investigation of angular momentum transport has a long standing history of being studied in TCF, from the early work of Couette (1890) [98], Mallock (1896) [99], and Taylor (1923) [48] to present day studies (see Refs. [100, 101, 102] for examples).

There are a few ways of quantifying angular momentum transport. Some measurement techniques are local such as the use of orthogonal, 2D Laser Doppler Velocimetry (LDV) probes to measure $\langle v_\theta v_r \rangle$ correlation which is related to angular momentum [100] and the observation of the rotation of mirror-encapsulated particles [103], or particles with internal markers [104]. There are also studies that calculate angular momentum transport from 2D-2C PIV measurements [105]. However, the most common way angular momentum is measured in TCF is through torque measurements.

In the limit as $\Gamma \rightarrow \infty$, the angular momentum transport from the inner cylinder to the outer cylinder (and *vice versa*) is the sum of the torque on the outer cylinder. The TCF apparatus used in this thesis was originally designed with the possibility of torque measurements in mind. Both inner and outer cylinders are driven by shafts that are split, allowing for a torque measurement to be made in the shaft itself. For more details on this design see Appendix C. Mechanical drawings of both the inner and outer shafts are given in Appendix Section D.2.

3.1.4 Temperature regulation

Making quantitative comparisons between experiment and theory/numerics requires precise control over Re_i and Re_o. In addition to a careful construction and smooth, constant driving, the temperature needs to be held constant. The working fluid's viscosity changes by ≈ 1.77 % per °C and the room temperature changes by as much as 3.5 °C throughout the day, which would mount to a 6.2 % change in Re_i and Re_o. To mitigate this, temperature stability is achieved in the flow domain by controlling the temperature of the refractive index matching reservoir the cell is submerged in.

The index matching reservoir is a custom-built acrylic liquid bath that was constructed to encase the inner and outer cylinders in order to remove distortions associated with imaging[9] through the curved surfaces of the cell. The temperature is held constant to within 0.02 °C using a heat exchanger coupled to a ThermoFisher Haake A25/AC200 temperature bath (Thermo Fisher Scientific, Waltham, Massachusetts). Together, with careful consideration of the working fluid's temperature-dependent viscosity, this system provided Re control to better than 1 %.

The fluid properties (i.e. viscosity and thermal conductivity) of the index matching fluid needs to be considered to achieve optimul termperature control. The easiest index matching fluid to work with is mineral oil since it does not evaporate or react with metals, but its thermal conductivity is relatively low (0.136 W·m C^{-1}), and its viscosity is relatively high (80 cSt); this makes for poor thermal contact between the temperature bath and the working fluid. To achieve the more effective thermal contact, aqueous NH_4SCN can be used. Aqueous NH_4SCN has $\approx 50\times$ lower viscosity and $\approx 4\times$ higher thermal conductivity.

3.2 Design and implementation of velocimetry system

3.2.1 Seeding particles

Many modern fluid velocimetry techniques rely on the use of tracer particles suspended in the flow. For these techniques to accurately measure the fluid's velocity, the tracer particles need to reliably advect along with their surrounding fluid element. To ensure this happens while also being able to be imaged on a camera, there are many things that need to be considered such as buoyancy, response time, optical scattering cross section, and the affect the presence of the particles have on the fluid's rheology [106, 78].

In addition to general considerations, when performing image based velocimetry near a surface of any kind, removing artifacts in the images associated with the illuminating light

---

[9] Since the illuminating light enters from the side, to illuminate the entire cross-sectional area, index matching is necessary for 2D-2C as well.

is essential. In some experiments, this can be done either by giving great care to choices of angles of illumination and observation; however, in the TCF geometry it is impractical to remove all reflections if velocity is to be probed near any wall. By using fluorescent particles with proper optical filters and illumination source, the illuminating light can be blocked while the fluorescence from the particles makes them easy to distinguish on the image. The use of fluorescent particles has the added benefit of improving the signal to noise ratio on the particle images. The following is a brief discussion on choosing optimal seeding particles for the TCF experiment and details pertaining to particles obtained from two different sources (i.e. home made and commercially acquired).

Choosing the optimal tracer particles

The choice of tracer particles used to seed the flow is an important parameter in an experiment employing particle-based velocimetry. Ideal tracer particles accurately advect along with the surrounding fluid and affect neither its rhoelogical properties nor its motion. These particles must also show up clearly on the cameras sensor and appear distinct from the surrounding fluid. Choosing the proper tracer particles requires finding a balance between lightweight particles small enough to passively track the flow yet large enough that they can clearly be seen on an image.

For the particles to be clearly seen on an image, the power of the light coming from the particles must be large enough to overcome sensor noise while also being noticeably greater than the ambient lighting and scattered illuminating light. This can typically be done by either increasing the illumination power or by increasing the particle size.[10] For non-fluorescent particles, the scattering cross section, C_s, for a spherical, dielectric particle is giving by Lorenz-Mie scattering [107, 78, 108]. The dependence of the cross-section on particle diameter d_p widely varies depending on the size range of the particles. For instance, the dependence changes from $C_s \propto d_p^4$ at $d_p = 1$ µm to $C_s \propto d_p^2$ at $d_p = 10$ µm illuminated

---

[10] In the case of fluorescent particles, more fluorescent dye concentration within each particle can also be increased to achieve brighter particles.

at 532 nm [109]. Therefore, it is typically much easier to increase the scattering power by increasing particle size than increasing illuminating power.

For experiments performed near walls or in confined geometries, reflections of the illumination light off walls and choice of the camera's viewing angle are difficult to control. The intensity of light scattered off small particles is very anisotropic with scattering intensities varying by a factor of 10^3 over just several degrees in some cases [107, 78, 108, 77]. This means that the angles made between the illumination source, particle, and camera are a critical parameters in experiments with small particles. If the camera is placed in a forward or backward scattering configuration, ambient illumination light is often difficult to control. By using tracer particles that are fluorescent, these challenges can be overcome. Fluorescent particles absorb illumination light at one wavelength and isotropically emit light at a different wavelength. The particles can viewed through optical filters that block out the illuminating light and pass through the fluorescence, allowing for near-uniform intensity regardless of viewing angle. The power of light emitted from the particles scales with d_p^2, making larger particles appear brighter in images [106, 78].

The size of the particle affects many aspects of the experimental setup beyond the apparent particle brightness on an image. Particle sizes must be chosen small enough that their size is not comparable to or larger than the smallest length scale in the flow. If they are comparable in size to the length scale in the flow, not only will they not simply advect with the flow, their presence in the flow will alter the flow itself. Even for particles much smaller than the smallest length scale in the flow, the particle size affects their settling time and response time to changes in the flow. The settling velocity in a stationary fluid can be calculated from a Stokes flow approximation to a spherical[11] particle as

$$|\mathbf{V}_{\text{settling}}| = \frac{g(\rho_{\mathrm{p}}/\rho_{\mathrm{f}} - 1)}{18}\frac{d_{\mathrm{p}}^2}{\nu}, \tag{3.1}$$

---

[11] The settling time also depends on the location of the center of mass within the sphere [110]. This calculation assumes the center of mass of the sphere is in the geometric center of the sphere as well.

where g is the gravitational acceleration, ρ_p is the particle's density, ρ_f is the fluid's density, and d_p is the particle's diameter. This shows that settling can be minimized by either making the particles small or making them neutrally buoyant. Although the strongest mechanism causing particles to accumulate in regions of the flow is buoyancy (either gravitationaly or centrifugally driven), even neutrally buoyant particles are known to accumulate near the walls in channel flow [111], in coherent structures in thermocapillary flows [112, 113], or on the boundary of vertices in TCF [114]. However, for most fluid flow experiments, these effects can probably be ignored.

In addition to ensuring that the particles remain suspended, it is also important to ensure that the particles will respond to changes in the fluid velocity quickly enough to be a good indicator of the fluid's velocity. A particle's response to an accelerating velocity field is quite complicated in general, but a response time can be estimated by considering a particle suspended in a sinusoidally varying flow [78, 77]. For small, neutrally buoyant particles, the response time is rather small and can often be neglected. For approximately neutrally buoyant particles ($0.56 < \rho_p/\rho_f < 1.63$) that range in size from 10 µm to 100 µm, the response time is smaller than 10^{-7} s [115].

A very important aspect of optimizing the use of a fluorescent tracer particle in a velocimetry system is properly choosing illuminating source and filters for the cameras. To best use the fluorescence, the particles should be illuminated at, or as close to, the peak of the fluorescent dye's absorption spectrum. A filter should then be chosen to block out the illuminating light sufficiently (often this requires a filter with OD 4 or higher) and pass as much of the fluorescent spectrum as possible. One important thing to keep in mind that is almost always neglected in the literature is that the fluorescence absorption and emmision spectra are strong functions of the substrate the fluorescent dyes are dissolved/doped in as well as the dye's concentration. For example, the emission spectrum of Rhodamine B doped PMMA is peaked between 570 nm and 620 nm depending on the concentration [116, 117]. Therefore, it is important to know the spectrum of the particles before designing the rest of the optics.

Producing in-house fluorescent tracer particles

Finding fluorescent particles that are the right size and mass density for a particular working fluid is typically challenging and often cost prohibitive. In the experiments performed with a working fluid that was refractive index matched to the cylinder walls, the fluid's mass density was large enough that particles suitable for use with water either centrifuge into regions of high vorticity or float to the top of the domain. To produce more suitable particles, batches of particles were made in-house.

The procedure followed to produce the fluorescent particles in-house is very similar to Borrero-Echeverry's method [89] which was itself adapted from Pedocchi et al. [118]. A batch of a casting resin is first doped with fluorescent dye (e.g. Rhodamine 6G) and allowed to cure into a block. The block is then ground into a fine powder and sieved to select particles in a range of sizes desired. This procedure is simple enough that changing material, fluorescent dye concentration, and/or grinding method is relatively easy.

Borrero-Echeverry's method employs a 120 grit silicon carbide sandpaper grinder to produce particles from the block of plastic. This grinding method is very time consuming, produces few particles large enough to use, introduces sand from the paper into the particle batch, and produces large clouds of fine particulate during the grinding process. Examples of particles produced from polyester resin using this method are shown in Figure 3.2(top). The particles produced with this method are anisotropic in shape and have significant particle to particle variation in fluorescent dye doping.

To speed up the production of particles, eliminate the non-fluorescent sand particles from the batch, and to avoid breathing in a cloud of Rhodamine doped, plastic particulate, a blade style coffee bean grinder can be used.[12] Producing particles from blocks of plas-

---

[12] In principle, a conical burr grinder or perhaps even a ball mill can also be used and likely would produce more monodisperse particle sizes. A blade style grinder was used here due to the large price difference between the two types of grinders.

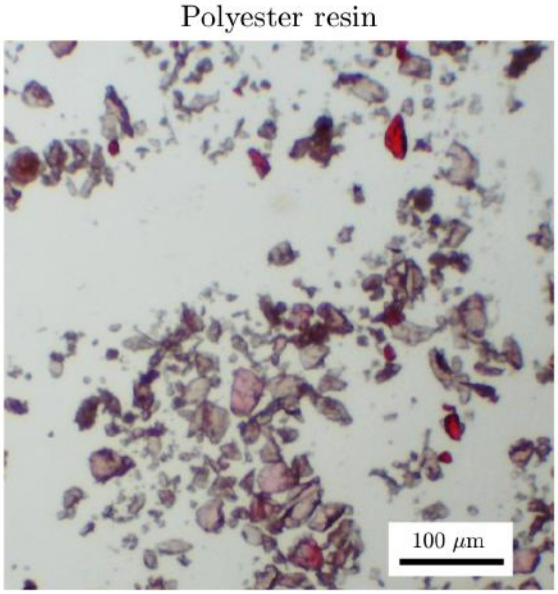

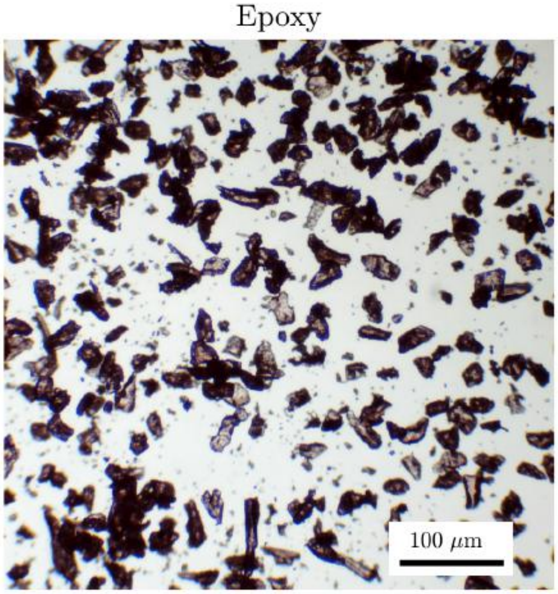

Figure 3.2: Brightfield microscope images of fluorescent tracer particles produced in-house. The polyester resin particles shown (top) were produced by Borrero-Echeverry and used for the studies described in his thesis [89]. Note the apparent nonuniformity in fluorescent dye doping from particle to particle. The epoxy particles shown here (bottom) were made from Fibre Glast 2000/2020 epoxy system, doped with Rhodamine B, then ground into particles in a coffee grinder. Both images were taken using a microscope with a calibrated 5 Mpx camera with 960 $\mu\text{m}\cdot\text{px}^{-1}$ magnification and illuminated with white light.

tic using a coffee grinder presents a significant speedup and produces particles of similar quality as can be seen in Figure 3.2(bottom). Coffee grinders are not designed to pulverize plastic blocks and this process eventually destroys the grinder, but they are relatively inexpensive.

The density of the particles that the in-house method produces depends on the plastic used.[13] Both Borrero-Echeverry and Pedocchi et al. used polyester resin to produce their particles. The bulk mass density of the Aristocrat Deep Clear Polyester Casting Resin (BDC Epoxy Systems, Santa Fe Springs, California) reported by Borrero-Echeverry is 1.24 $\mathrm{g{\cdot}cm^{-3}}$. Reproducing the same protocol with Castin Craft Clear Polyester Casting Resin (Environmental Technology Inc., Galesburg, Michigan) produces a bulk mass density of 1.2142 $\mathrm{g{\cdot}cm^{-3}}$ ± 0.0013 $\mathrm{g{\cdot}cm^{-3}}$, suggesting that the specific density of the particles produced depends not only on material used but also the supplier of the material. The density of a few plastics that can be easily doped with fluorescent dyes[14] are listed in Table 3.1. To better match the density of the working fluid that was index matched to the PMMA walls ($\rho_f \approx 1.14\ \mathrm{g{\cdot}cm^{-3}}$), epoxy plastic was explored as an alternative to Polyester resin. The epoxy chosen was purchased from Fibre Glast (Fibre Glast Developments Corp., Brookville, Ohio) which had a reported density of $1.125\ \mathrm{g{\cdot}cm^{-3}}$.

When choosing accompanying optics to be used with the fluorescent particles (i.e. illuminating light source and band pass filters for the cameras), it is important to know the absorption and emission spectra of the particles. As with any fluorescent dye, the specific material the dye is doped in can significantly affect both the absorption and emission spectra. Spectra for dyes in the Rhodamine family are typically reported when dissolved in ethanol. As Figure 3.3 and Figure 3.4 show, there are significant changes to the spectra[15]

---

[13] The density of the resulting particles may also depend on the method used to 'grind' them. Since plastic is malleable, the thermal and physical stresses introduced during grinding/pulverizing the block may affect the density.

[14] The mixing time for the fluorescent dye into the various plastics varries widely from plastic to plastic. For instance, Rhodamine B mixed into Fibre Glast system 2000 overnight, while their system 1000 took weeks.

[15] A phenomena is made clear in fluorescent techniques outside of PIV [119].

Table 3.1: Mass density of various cast plastics. The density was determined by measuring the volume using Archimedes principle and measuring the mass of the block. Each plastic was only mixed once, so batch to batch variations could still exist.

Material	ρ [g·cm^{-3}]
Castin Craft Clear polyester Resin	1.2142 ± 0.0013
Fibre Glast 2000 epoxy with 2020 hardener	1.1724 ± 0.0116
Fibre Glast 1000 epoxy with 1010 hardener	1.1992 ± 0.0145
J-B Weld 50112 ClearWeld Epoxy	1.1682 ± 0.0026
Loctite Epoxy High Strength Epoxy	1.2076 ± 0.0014
Loctite Epoxy Instant Mix	1.1973 ± 0.0025
Gorilla Glue Clear Epoxy	1.1806 ± 0.0016

for Rhodamine B dissolved in ethanol as compared to Rhodamine B doped in PMMA. To optimally use either the Epoxy or Polyester resin particles produced in-house, the absorption and emission spectra should be measured to best determine cut-off wavelengths of filters.

Although particles produced by this method are very inexpensive and quite customizeable, they are rather anisotropic. For particles not doped with fluorescence, the scattering cross section changes significantly depending on the orientation [123]. Similarly, for fluorescent particles, the power of light emitting from the particles scales as the cross-sectional area which is significantly different from one orientation to another. Variations in particle intensities on images from frame to frame is a source of uncertainty even for standard planar PIV [124], but for particle tracking or for 3D techniques the problem is a limitation [125]. In many PIV systems, the particle size is small enough that particles show up as just a few pixels wide in the images. In these setups, perfectly spherical tracer particles may not be necessary. For experiments performed in our Taylor-Couette system, the anisotropic nature of the particles produced in-house was problematic enough that commercially obtained, highly spherical particles needed to be procured.

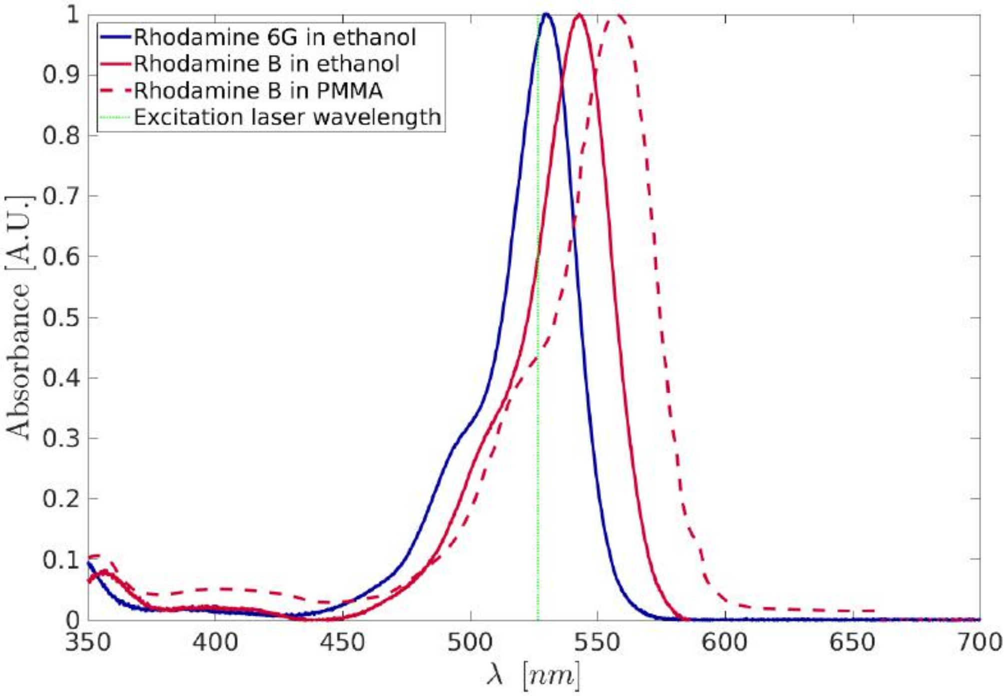

Figure 3.3: Absorbance spectra from Rhodamine 6G and Rhodamine B dyes. The absorbance/emittance spectra for fluorescent dyes dissolved in ethanol are some of the most readily available; however, the substance being doped plays a significant role. Note that Rhodamine B dissolved in ethanol (red solid) has an absorption peak at 542.5 nm while Rhodamine B doped PMMA (red dashed) is peaked at 558 nm. Spectra for Rhodamine 6G/B disolved in ethanol taken from [120, 121] and Rhodamine B doped PMMA was adapted from [122].

Tracer particles used

The particles produced by the procedure described in subsubsection 3.2.1 work great for experiments where optical setup are chosen to minimize the anisotropic effects, but they are not suitable for experiments in the new Taylor-Couette system where more than one viewing angle is required. Intensity variations, both particle to particle as well as from frame to frame, significantly reduce the fidelity of any PIV or PTV measurement, but the anisotropic shape of the in-house manufactured particles can be a show-stopper for 3D particle tracking techniques.[16] These techniques require computing a representative 2D Gaussian ellipse

---

[16] Tomographic PIV techniques that implement Iterative Particle Reconstruction (IPR) to compute the 3D intensity field will have the exact same pitfall as that of 3D particle tracking with the use of anisotropic particles.

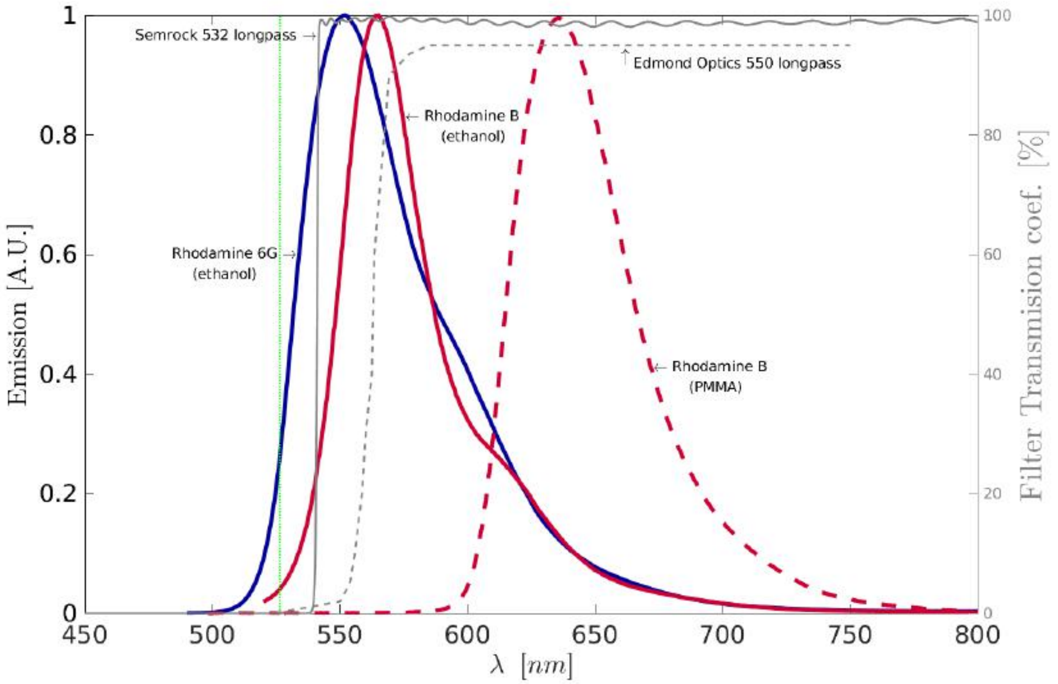

Figure 3.4: Emittance spectra of Rhodamine B/6G dyes and transmission spectra of longpass filters. The absorbance/emittance spectra for fluorescent dyes dissolved in ethanol are some of the most readily available; however, the substance being doped plays a significant role. Note Rhodamine B dissolved in ethanol (red solid) has an emission peak at 565 nm while Rhodamine B doped PMMA (red dashed) is peaked at 636 nm. Spectra for Rhodamine 6G/B dissolved in ethanol taken from [120, 121]. The Rhodamine B doped PMMA spectrum was observed from Dantec seeding particles (Dantec Dynamics, Inc., Skovlunde, Denmark) excited with a frequency doubled ND:YLF laser at 526.5 nm and measured using an Ocean Optics FLAME-T spectrometer (Ocean Optics, Inc, Orlando, Florida, USA).

that can be fit to particles in the 2D images [81]. If the particles look substantially different when viewed from one angle compared to another, the parameters of the estimation of the representative Gaussian will be of poor quality, leading to an inability to fit the representative particles to the imaged particles. Therefore, highly uniform, isotropic or spherical particles are desired.

Unlike non-fluorecent tracer particles, procuring spherical particles in the right size and density that are fluorescent is difficult. Adding to that the criteria for the fluorescence to be compatible with your illumination source and cameras makes it even less likely that particles will be commercially available. For the Taylor-Couette experiments, the index matched, aqueous ammonium thiocyanate working fluid has a density of $\rho_f \approx 1.14$ g·cm^{-3} and our illuminating laser emmits $\lambda = 526.5$ nm (green) light. These two criteria practically narrow the search parameters to acrylic (PMMA) particles doped with a Rhodamine family dye. PMMA has a nominal density of $\rho_{\text{PMMA}} \approx 1.18$ g·cm^{-3} which is only 3.5 % more dense than the working fluid.

Although it is an unfortunately uncommon tracer particle to use, Rhodamine B doped PMMA particles can be purchased in a range of sizes. Dantec (Dantec Dynamics, Inc., Skovlunde, Denmark) sells these particles ranging in size from 1 µm to 50 µm. The particle range centered around 35 µm was chosen (Dantec part number 80A8401, PMMA-RHB-35). As can be seen in Figure 3.5, the particles are highly spherical and seemingly uniformly doped.

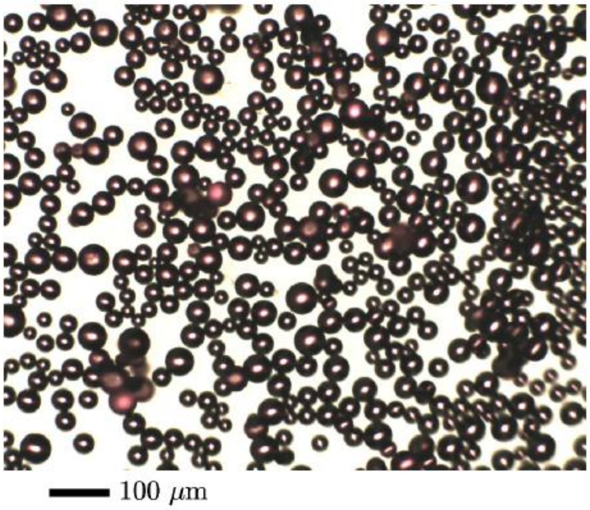

Figure 3.5: Brightfield microscope images of Rhodamine B doped PMMA particles acquired from Dantec (Dantec Dynamics, Inc., Skovlunde, Denmark). Image was taken using a microscope with a calibrated 5 Mpx camera with 960 µm·px^{-1} magnification and illuminated with white light.

Ideal tracer particles would be monodisperse in size in order to make their appearance uniform on an image. The particles obtained from Dantec are labeled as 35 µm but have a size distribution ranging from about 20 µm to 55 µm. To determine the size distribution, microscope images of dried particles were placed on a microscope slide and imaged. Those images were then analyzed and the particle diameters were measured yielding the size distribution shown in Figure 3.6.

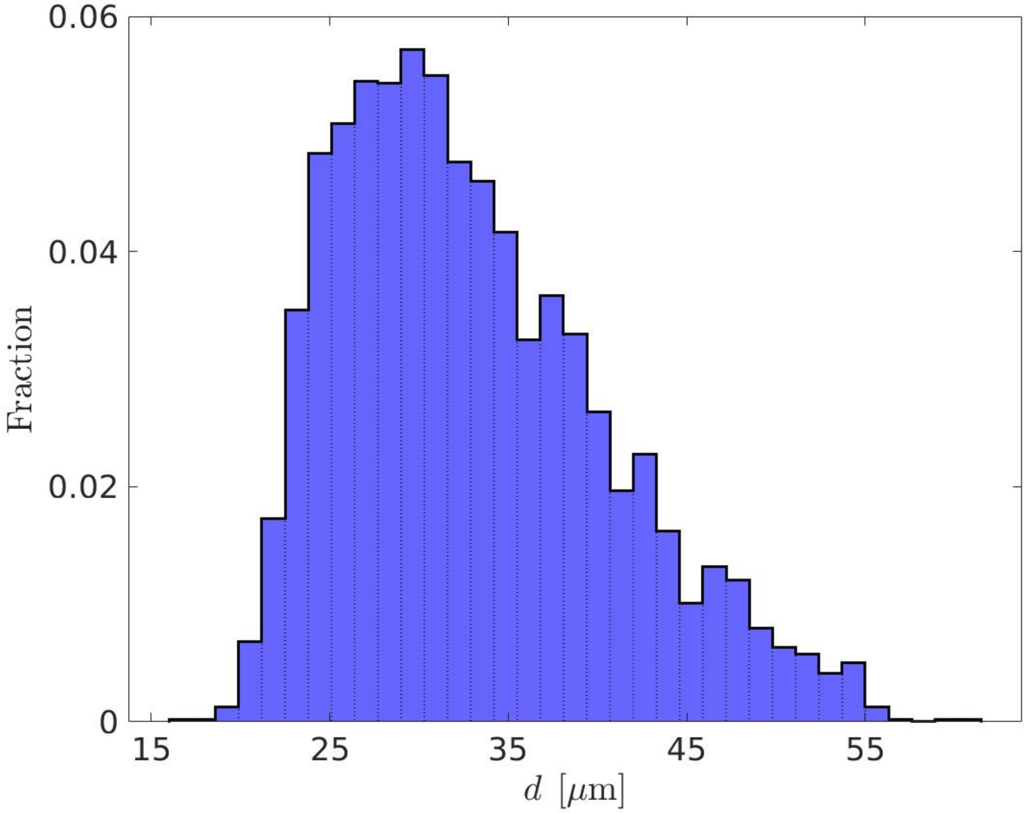

Figure 3.6: Size distribution of Rhodamine B doped PMMA particles from Dantec (Dantec Dynamics, Inc., Skovlunde, Denmark). Distribution measured from particles spread out on a microscope slide using a microscope with a calibrated 5 Mpx camera with 960 µm·px^{-1} magnification, see Figure 3.5.

In order to design a velocimetry system that best uses the fluorescence, the absorption and emission spectra of the particles need to be known. With the absorbtion and emmission spectra in hand, proper filters can be acquired whose cut-on wavelengths fall between the illuminating light source and the particles' fluorescence peak. To measure the emission spectrum, the Rhodamine B doped particles were excited with a frequency doubled ND:YLF laser at 526.5 nm and measured using an Ocean Optics FLAME-T spectrometer (Ocean Optics, Inc, Orlando, Florida, USA). The resulting emission spectrum is shown in

Figure 3.4. Given the fluorescence spectrum, a suitable filter for these particles would have a cut-on wavelength that is between 530 nm and 600 nm.

The particles are stored suspended in water when shipped from Dantec. Since PMMA, like all plastics, is porous, it will absorb small amounts of the liquid it is suspended in. The particle size will change by a small amount, but its mass will change by an even larger amount [126] resulting in a change in the particles mass density.[17] Since the particles are stored in water, the particles will have a density slightly higher than dry PMMA. For careful density tuning, this should be accounted for.

3.2.2 Working fluid

The ideal working fluid is a transparent Newtonian fluid that has a refractive index carefully matched to the cell walls and mass density equal to that of the seeding particles. A fluid with the same refractive index as the cell walls would eliminate refraction from the inner cylinder, allowing the illuminating light as well as the lines of sight for a camera to pass through the inner cylinder without distortion, thereby increasing the portion of the flow effectively seen by each camera. The working fluid must also have a mass density close to that of the tracer particles in order to avoid inertial effects from the particles themselves. Additionally, the more precisely tuned the fluid's density is to the particles, the longer the duration of time before the flow needs to be agitated to mix the particles back in.

The optical and mass properties of the fluid need to be tuned while also remaining relatively low viscosity. If the viscosity of the working fluid is increased, the velocity scale needed to achieve the same physical regime also increase. This means that the motors need to spin the cylinders faster resulting in the cameras and laser needing to operate at a higher rate in order to achieve the same apparent particle displacement between two successive images. Therefore, keeping the working fluid's viscosity low, allows for smaller motors and slower cameras, keeping the design relatively inexpensive. For a relatively large range

---

[17] The timescale for this is on the order of a month as can be seen on Figure 3 of Drotning and Roth, 1989 [126].

of design parameters, a working fluid that can meet all of these criteria can be achieved with an aqueous solution of salts. In the following, the considerations for choosing the optimal working fluid for the new Taylor-Couette setup is discussed.

Refractive index matching

In order to minimize the optical distortions from the cylinder walls, the working fluid's index of refraction must be matched to the polymethylmethacrylate (PMMA) the cell is constructed from. Aqueous solutions of ammonium thiocyanate (NH_4SCN) at concentrations relatively close to saturation have been shown to have refractive indexes, n, in the range of that of PMMA [94, 127, 128, 129]. The specific value of n for PMMA, however, varies from batch to batch [94] due to slight variations in the specific conditions while the polymer cures. Therefore, a measurement of the specific refractive index of the specific batch of PMMA used to construct cell walls was needed to achieve the best index matching.

To measure the index of refraction of the PMMA used to construct the cell walls, the angle of deviation of light passing through a prism was measured. A prism with an interior angle of $\Theta_{\text{prism}} = 45^\circ \pm 0.1^\circ$ was made out of the same block of PMMA the cell was constructed from. The angle of deviation of light passing through the prism was measured as a function of the angle of incidence using two goniometers attached to each other providing an angular uncertainty of 0.08°. From geometric optics, it can be shown that the refractive index is related to the angle of deflection (δ), the interior angle of the prism (Θ_{prism}), and the angle of incidence (θ_{i}) as

$$\sin\left[\delta - \theta_{\text{i}} + \Theta_{\text{prism}}\right] = n \sin\left[\Theta_{\text{prism}} - \arcsin\left[\frac{\sin\left[\theta_{\text{i}}\right]}{n}\right]\right]. \tag{3.2}$$

A χ^2 regression of Equation 3.2 to measured δ and θ_i can then be used to determine the value of n.

The optimal wavelength at which the refractive index should be matched corresponds to the peak of the fluorescent emission spectrum of the dye doping the tracer particles (if fluorescent particles are not being used, then the index matching should occur at the wavelength of the illuminating light). As with any fluorescent dye, the emission spectra for Rhodamine B and 6G depends strongly on its surroundings as well as concentration and excitation wavelength [117]. Most spectra reported for Rhodamine B and 6G are captured from the dye dissolved in ethanol [120, 122, 130] and excited precisely at its peak absorption, however the spectra changes drastically when doped in solids [117]. The Rhodamine B doped tracer particles obtained from Dantec being used in the current experiment, give off red light (peaked around 636 nm) when excited with a frequency doubled ND:YLF laser (526.5 nm) (see Figure 3.4).

Determining the index of refraction of the PMMA at the most relevant[18] wavelength was done by mixing a large concentration of the Dantec tracer particles in a container, illuminating the container from above with green LEDs peaked around 524 nm, and passing the fluorescence escaping from the side of the container through a slit in front of the prism centered on the goniometer. The angle of deviation through the prism was then measured for the fluoresced light. This resulted in a refractive index of $n(636\,\text{nm}) = 1.4921 \pm 0.0021$. These measurements were performed at an ambient temperature of 22 °C, but since $\frac{dn}{dT} \approx 10^{-4}\,^{\circ}\text{C}^{-1}$ [111, 131, 132] (which corresponds to changes in n that are smaller than the experimental uncertainty of our current measurements), the variation in temperature can be neglected.

In order to produce a transparent fluid of relatively low viscosity and a refractive index of $n(636\text{ nm}) = 1.4921$, NH_4SCN is added to water with a mass concentration of approximately 3/2 to that of water (for more information about index matching using aqueous NH_4SCN, see [127]). This results in a fluid with nearly the correct refractive index;

---

[18] Here, the most relevant wavelength is taken to be the wavelength of the light emitted from the fluorescent doped tracer particles, as this is what the cameras are seeing. In three dimensional, three component (3D-3C) measurements, this is the wavelength that index matching needs to happen at to reduce refraction. It should be noted that for the 2D-2C measurements taken at a constant z-height, the relevant wavelength to index match to is 526.5 nm, since the index matching is to allow the light sheet to illuminate the entire plane in the flow domain.

however, deviations in the concentration needed vary with NH_4SCN supplier and purity. Additionally, NH_4SCN is hygroscopic, so the true mass of the salt is practically unknown unless it is stored in a perfectly dry environment. In practice, a mixture with an approximate mass concentration of 3/2 is produced then tweaked until the refractive index is obtained. Since the amount of NH_4SCN that is being added is near the saturation point, the mixture needs to be heated to overcome the cooling from the endothermic dissolution of the salt.

As the mixture is being prepared, the index need to be measured using a refractometer. Because the temperature of the mixture will be quite different from room temperature during preparation, it is important to wait until the fluid sample has come into thermal equilibrium with the refractometer before making a measurement. Measurements of the liquid's temperature while sitting on the Atago 3850 PAL-RI hand-held refractometer (Atago Company, Tokyo, Japan) used in while preparing working fluid in all studies presented here suggest that it takes about a minute for the temperature to come to equilibrium.

The refractive index of both the working fluid and the PMMA cell walls vary with wavelength. Most digital refractometers measure the index around 589 nm which is the sodium D-line. In the case of the Atago 3850 PAL-RI refractometer, the refractive index is measured around 593 nm (see Figure 3.7 for the spectrum from Atago 3850 PAL-RI handheld refractometer). To use this refractometer in the most optimal way, the wavelength dependence of the refractive indices of the cell wall and working fluid would need to be known to calculate a correction for the refractometer's reading. Though this dispersion relation for PMMA is published in the literature [132], it is yet to be determined for the working fluid discussed here. However, this correction is likely to not matter for two reasons. First, the derivative with respect to wavelength of the refractive index of PMMA in the range of our particles emittance is -3.954×10^{-5} nm^{-1} [132] (i.e. $\Delta n \approx 0.0017$ from 593 nm to 636 nm) which is a very small correction. Second, if we take the working fluid to be water, the derivative with respect ro wavelength of the refractive index is -3.065×10^{-5} nm^{-1} [133], which is very similar to that of PMMA. Therefore, if the working fluid has a comparable dispersion to that of water in this range, the correction to the refractometers reading would be significantly smaller than the uncertainty in the Atago refractometer's measurement.

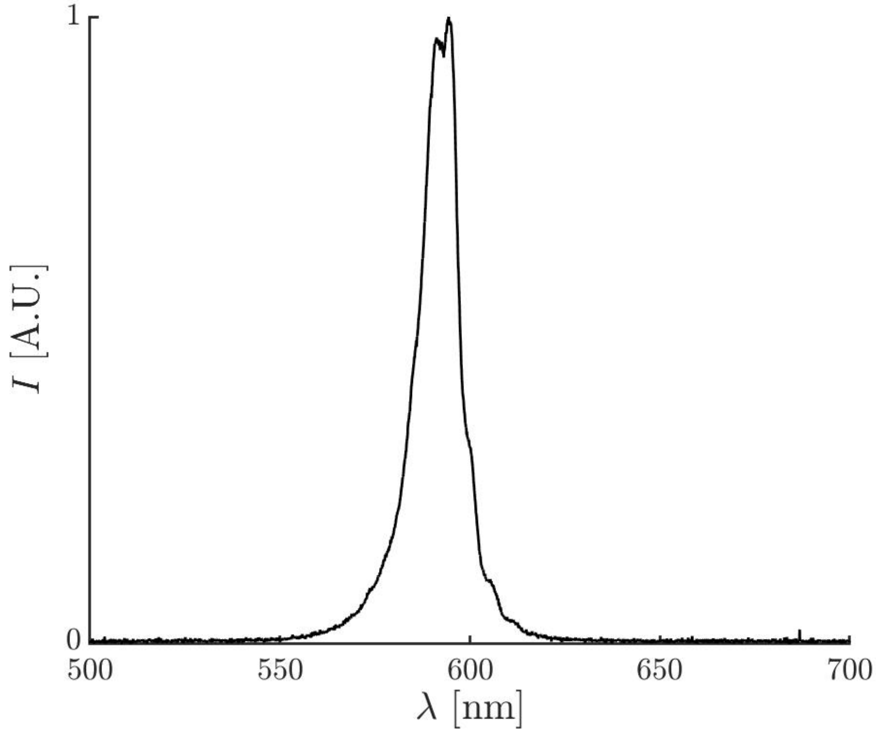

Figure 3.7: Spectrum of the test light used in Atago 3850 PAL-RI hand-held refractometer (Atago Company, Tokyo, Japan). Note that the peak intensity is in a narrow band centered around 593 nm which is approximately the Sodium D-line. The intensity of the light is reported here in arbitrary units. Spectrum was measured using an Ocean Optics FLAME-T spectrometer (Ocean Optics, Inc., Orlando, Florida, USA).

The cooling reservoir fluid along with the working fluid must also be index matched in order to remove optical distortions caused by the outer cylinder walls. To completely match the index requires the use of an aqueous solution of NH_4SCN; however, Mineral Oil (Equate brand) was measured to have an index of $n(T = 26\,°\mathrm{C}) = 1.4798 \pm 0.005$, which is sufficiently close to that of the PMMA walls for many types of experiments. To avoid using corrosive salts or oils in the temperature bath, a reservoir box is filled and a heat exchanger is used. The reservoir box size is then made as small as possible to minimize the amount of index matched fluid needed. During experiments that require the precise index matching provided by NH_4SCN mixtures, the cooling tank fluid is initially prepared to have the same index of refraction as the walls. Since there is significant contact with the room air, evaporation occurs, resulting in the refractive index changing. Depending on the room conditions, the cooling fluid needs to be tweaked from week to week, or even day to day. With both the TCF cell and the cooling tank filled with index matched fluid, the walls become nearly invisible (see Figure 3.8).

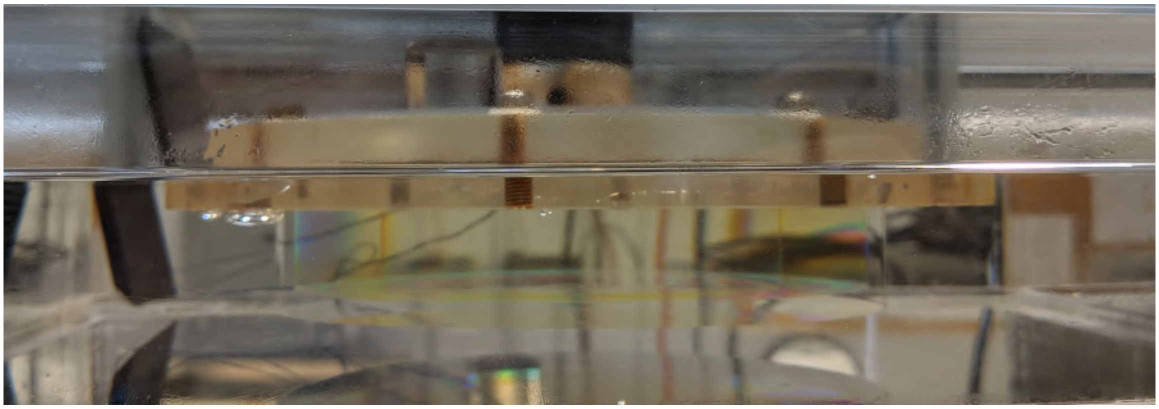

Figure 3.8: Typical quality of refractive index matching. Both the working fluid (a mixture of H_2O, NH_4SCN, NaI, and l-ascorbic acid) and cooling reservoir (a mixture of of H_2O, NH_4SCN, and l-ascorbic acid) are prepared to have a similar refractive index to the walls of the TCF cell. For 3D velocemitry measurements, the index matching should be no worse than what is seen here.

Aqueous ammonium thiocyanate rapidly corrodes ferrous alloys, making its implantation in index matched experiments challenging (even stainless steels rust rapidly in the presence of aqueous NH_4SCN). The SCN-radical, in conjunction with atmospheric oxygen, acts as cathodic depolarizing agent in the oxidation of iron [134]. This corrosion has been shown to be inhibited with increasing the pH above about 10 [134] and may be an easy solution to many of the corrosion-related challenges. In addition to corroding any ferric metals in contact with the fluid, Fe(III) forms a complex with SCN (iron(III) thiocyanate) that is deep red in color [135]. As the fluid continues to react with iron, the red pigmentation intensifies, making the fluid more and more opaque. The iron thiocyanate complex can be broken and the reddening removed with the addition of ascorbic acid [136]. For this reason, a small amount of l-ascorbic acid is added to every batch of index matched working fluid.

In addition to the working fluid being index matched to the cell walls, it also should be density matched to the density of the tracer particles. This can be achieved by adding an already index matched aqueous solution of sodium iodide (NaI) to the NH_4SCN solution. By adding small amounts of index matched aqueous NaI, the density can be tuned while maintaining the same refractive index.

Mass density matching

A high fidelity measurement of the fluid's velocity over an extended duration of time requires the fluid and particle mass density to be matched. Velocimetry measurements based on the motion of tracer particles assume that the particles advect along with the surrounding fluid element. For this to be true, the effect of the buoyant force acting on the particle must be small compared to flow forces from the fluid. The buoyant force is proportional to mass, so reducing either the particle's size or matching their density to the surrounding fluid will mitigate buoyancy effects. However, since the particles need to be seen on images, the particle size cannot be made arbitrarily small. This means that the fluid-particle density difference must be close to zero [78, 77]. Additionally, measurements of the fluid velocity that occur over a long duration of time require the tracer particles to remain uniformly suspended. If the density is not matched, the particle settle out or accumulate in high-vorticity regions due to centrifugal forces, leaving regions with sparse tracer seeding and making velocimetry challenging or even impossible.

The particles used in most experiments presented in this thesis were purchased from Dantec (Dantec Dynamics, Inc., Skovlunde, Denmark) and are made of PMMA, which has a nominal density of $1.188\ \mathrm{g\cdot cm^{-3}}$ at 20 °C, according to the supplier. However, since PMMA is a porous polymer plastic, the particles will over time absorb a small amount of the fluid they are suspended in. As the particles absorb the fluid, their size remains relatively unchanged, but their mass increases, resulting in an increased particle density.

To avoid this change in density, the particles would ideally be stored in the fluid that is matched to the particle's density after they have been saturated with that density matched fluid. Finding the proper density of this fluid can be done by maximising settling time of saturated particles. The time over which the particles become saturated is, however, rather long and this optimization has not yet been performed. Additionally, the working fluid is easily contaminated, making it poorly suited to store the particles in. Instead, the Dantec particles are stored suspended in water and the working fluid's density is matched to the density of particles saturated with water. This means that if a batch of working fluid is made to have very accurate density matching, over time it will become less density matched (particles become more dense with time).

The density tuning of the already index matched working fluid is done by mixing in a premixed, heavy aqueous salt solution that is also index matched to the PMMA. Aqueous sodium iodide (NaI) solutions can have a refractive index[19] of $1.33 \lesssim n \lesssim 1.67$, kinematic viscosity of 1 $\mathrm{mm^2{\cdot}s^{-1}} \lesssim \nu \lesssim 1.21\ \mathrm{mm^2{\cdot}s^{-1}}$, and densities of 1 $\mathrm{g{\cdot}cm^{-3}} \lesssim \rho \lesssim 2.5\ \mathrm{g{\cdot}cm^{-3}}$ [137], making NaI an ideal salt for density tuning. By producing an index matched solution of NaI and adding it to the index matched NH_4SCN solution, the refractive index can remain approximately unchanged while augmenting the density. The density of the aqueous NH_4SCN solution was measured using a 500 ml class A volumetric flask filled and placed on a mass balance (Autogram 1000) with a resolution of 0.1 g at room temperature (measured to be nominally 23 °C). The density at room temperature of the index matched NH_4SCN is $\rho_{\mathrm{NH_4SCN}} \approx 1.1398 \pm 0.0005\ \mathrm{g{\cdot}ml^{-1}}$, which is only a 4 % difference from the nominal particle density as reported by Dantec, meaning only a small amount of NaI is needed to density match. Mixing NaI to H_2O in a mass ratio of $m_{\mathrm{H_2O}}/m_{\mathrm{NaI}} = 0.55$ results in an approximately index matched solution with a density of $\rho = 1.83\ \mathrm{g{\cdot}ml^{-1}}$ measured using the same setup as the NH_4SCN solutions density.

The procedure to tune the density of the ternary mixture of aqueous NaI and aque-

---

[19] Saturated mixtures of NaI and H_2O in the lab at 21.8 °C yielded $n = 1.5025$ which is notably lower than the max value reported in [137].

ous NH_4SCN is an iterative, add-and-check method. The nominal volume fraction of the mixture is $V_{\text{NaI}}/V_{\text{NH}_4\text{SCN}} = 0.0615$ (e.g. to produce 200 ml total, mix 11.6 ml of the NaI solution to 188 ml of the NH_4SCN solution). Once the nominal mixture has been made, the Dantec tracer particles should be mixed in. The mixture then needs to be tuned by adding more NaI solution or more NH_4SCN solution until the settling time of the suspended particles is sufficiently long. There are a number of ways to monitor the settling time, but the most straight forward way is to wait a set amount of time, shine light on the container, and look near the top and bottom for gaps in particle concentration.[20] The density of the fluid is dependent on temperature, so the temperature of the mixture should be controlled and monitored so the cooling reservoir on the TCF apparatus can be adjusted to match these conditions.

Example: producing 250 ml of working fluid

To summarize, let's consider an example where we want to produce 250 ml of density and index matched working fluid. First, we need to figure out how much of each solution is needed. The volumes of the two solutions are mixed in a volume ratio of $V_{\text{NaI}}/V_{\text{NH}_4\text{SCN}} = 0.0615$, so

$$\begin{aligned} V_{\text{NaI}} &= 0.0579 V_{\text{tot.}} = 14.48 \text{ ml} \\ V_{\text{NH}_4\text{SCN}} &= 0.9421 V_{\text{tot.}} = 235.52 \text{ ml} \end{aligned} \tag{3.3}$$

Once we know how much of each is need, we can make the individual solutions. To make the ammonium thiocyanate solution, we will want to start with mixing m_{A} of

---

[20] The particles become much easier to see if illuminated with green light and viewed through either the camera's longpass filter or laser safety glasses intended for use with a green laser.

NH_4SCN into $V_{H_2O,\text{A}}$ of water and

$$\begin{aligned} V_{H_2O,\text{A}} &= \frac{\rho_n(C,T)}{\rho_{H_2O}} \frac{V_{\text{NH}_4\text{SCN}}}{1+R} \\ &= 0.4571 V_{\text{NH}_4\text{SCN}} = 107.65 \text{ ml} \end{aligned} \tag{3.4}$$

where $\rho_n(C,T)$ and $V_{\text{NH}_4\text{SCN}}$ are the density and volume of the index matched NH_4SCN solution and R is the ratio of mass of NH_4SCN to water of the solution. Similarly, the volume of water that is needed for the sodium iodide solution is

$$V_{H_2O,\text{S}} = 0.651 V_{\text{NaI}} = 9.43 \text{ ml} \tag{3.5}$$

where V_{NaI} is the volume of total index matched sodium iodide solution. Once the two solutions are made, they can be mixed to produce the final working fluid. A small amount of l-ascorbic acid should be added to improve longevity of the working fluid.

3.2.3 Image acquisition

For experiments in the new TCF system using 3D-3C velocimetry, the tracer particles were imaged simultaneously with eight, 10-bit monochrome, 1.3 Mpixel CMOS cameras (iDS Model UI-3140CP-M-GL) with a maximum frame rate of 224 frames per second. The cameras were fitted with 50 mm Nikon Nikkor fixed focal length lens at a working distance 1.2 m. Because the dimensions of the cell were chosen to optimize the velocimetry system, the entire depth of the flow domain is able to fit into the depth of field of the cameras when an aperture setting of $f/11$ was used. This allows for the full flow domain to be imaged in focus without the use of Scheimpflug lens mounts that are typically required for 3D-3C measurements. The field of view for a given camera was less than the full domain; however, all eight cameras, in aggregate, could view the entire flow domain such that by careful calibration, camera views could be stitched together to enable velocimetry over the complete flow domain. The camera configuration is demonstrated in Figure 3.9. For experiments using 2D-2C velocimetry, tracer particle time series in the new TCF system were captured using a single 10-bit monochrome camera.

The cameras were mounted on Manfrotto MHXPRO-BHQ2 ball head mounts (Vitec Imaging Solutions, Ramsey, NJ). These Manfrotto mounts are designed to attached to larger format cameras with a single 1/4 inch screw. To attach the small iDS cameras, adapters were made. Mechanical drawings of the camera adapters can be found in Section D.1. The ball mounts are fastened to the optical table via a 3/8 inch to 1/4-20 thread adapters. Figure 3.9 illustrates the angles each camera is oriented.

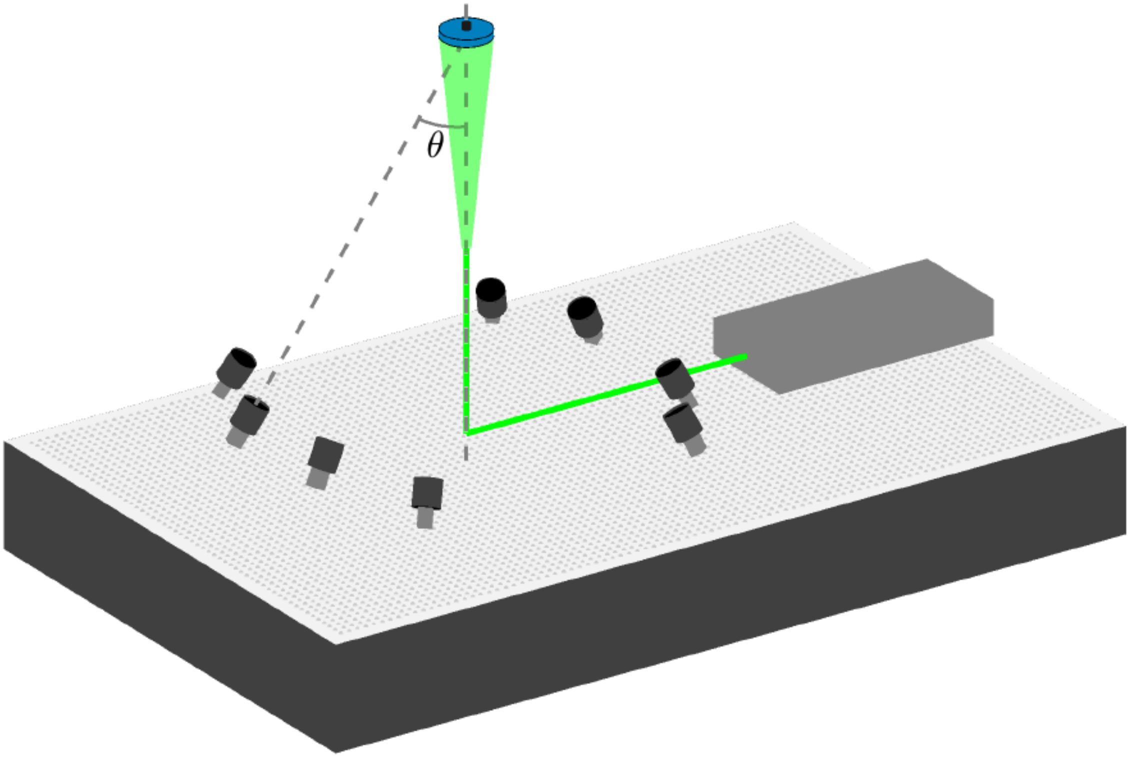

Figure 3.9: Camera configuration for 3D-3C measurements. The viewing angle, θ, is the angle between the camera and the z-axis of the TCF cell.

For all data collected from the new TCF system, image data were streamed real-time to a custom-built image acquisition system (1st Vision Inc. Model DVR-T994-31-8020) that features eight, 1 TB solid state drives in a RAID-0 configuration. Frame grabbers are driven by NorPix StreamPix 7 acquisition software and save the images in a single .seq file format. The raw images from each camera are stored into a single .seq file that is then passed through custom software written to convert image data from the NorPix proprietary format to a lossless format (.tiff) suitable for importing into other software packages.

The cameras and illuminating laser need to be synced to ensure a particle is illuminated once per exposure. The iDS cameras have an external trigger signal pin, isolated via an electro-optical coupler.[21] The cameras can be triggered off either the rising or falling edge of a TTL square wave signal.[22] Similarly, the Photonics DM30-DH laser driver can be externally triggered on either the rising or falling edge of a 0 V to 5 V signal. Both the laser and cameras are triggered by a Siglent SDG 1062X, 60 MHz dual channel arbitrary waveform generator.

For all experiments, noise from undesired laser light scattering is significantly reduced by fitting each camera with a long-pass edge filter (Semrock Model BLP01-532R-50) to collect fluorescence with 99+ % transmittance while attenuating scattered laser light by a factor of 10^7. Figure 3.4 shows the transmission curve for the long-pass filters as well as the emission spectra of the fluorescent tracer particles used in velocimetry experiments.

3.3 Experimental procedure

The procedure for setting up and conducting experiments that implement image velocimetry in the TCF apparatus depends on the type of velocimetry being used. The following discussion is split up into procedures related to planar, 2D-2C measurements in subsection 3.3.1, procedures related to volumetric 3D-3C measurements in subsection 3.3.2, and data post-processing steps in subsection 3.3.3.

---

[21] This allows for a max trigger voltage of 24 V.

[22] The signal does not need to be a square wave, but for most reliable performance, a signal with a sharp edge should be used.

3.3.1 2D-2C

Setting up the illuminating light

2D-2C PIV measurements require illuminating a thin slice of the flow. To produce a thin sheet of light, the laser beam needs to be shaped and located at the proper plane. There are several methods often employed to achieve a planar sheet of light [78, 77, 138]. The typical laser sheet used for 2D-2C measurements is first columnated with a pair of properly chosen lenses, then fanned out using a fast cylindrical lens (see for example section 3.3.2 of Fries 2020 [139]). Columnating the beam requires two lenses spaced an exact distance apart. This lengthens the optical beam path. Increasing the beam path would require additional mirrors and both take up more space on the crowded optical table and increase the complexity of the alignment procedure. Due to the geometry of the domain needing to be illuminated, it is possible to avoid columnating the beam and produce an approximately uniform thickness light sheet.

By using a converging, long focal length lens, the laser light can be focused in the center of the cylinders resulting in a symmetrical, thin wedge of light. Figure 3.10 illustrates how a long focal length lens can achieve this. To achieve a laser sheet whose thickness[23] is approximately 1 mm, an 85 mm spherical lens is placed in the beam 85 mm before the exact center of the cylinders. The typical 2D-2C light sheet thickness is sub-millimeter [139]; however, because the smallest length scale present in the somewhat low Re flows investigated here, the relatively thick illumination sheet is acceptable.

To spread the light out into a sheet, a negative focal length cylindrical lens is used. The focal length of the lens was chosen such that the laser beam (approximately 1 cm diameter at the cylindrical lens) would fan out to illuminate the entire width of the TCF cell. Due

---

[23] If the laser beam is columnated coming out of the laser, the Rayleigh length [140] of the focal point is 7.3 mm which yields a beam thickness from 0.48 mm at the inner cylinder and 0.67 mm at the outer cylinder. The laser beam coming out of the Photonics DM30-DH Nd:YLF laser is actually expanding with $\theta_1 \approx 0.27°$. This divergence decreases the Rayleigh length and thereby increasing the thickness of the sheet to about 1 mm.

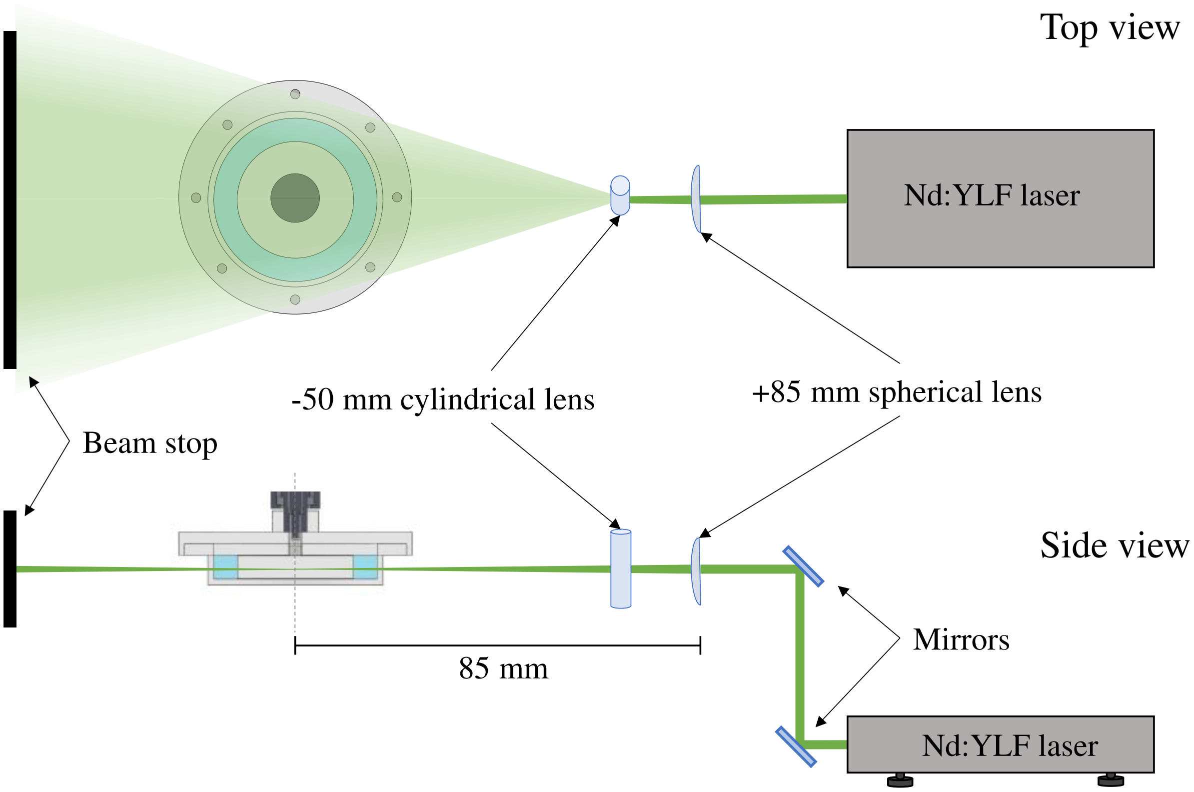

Figure 3.10: Schematic of illuminating light configuration for 2D-2C measurements. The laser light is brought to the height of the desired measurement plane with properly placed mirrors. The beam then passes through an 85 mm focal length spherical lens that is placed so that the beam is focused in the center of the inner cylinder. Immediately after the light passes through the spherical lens, it is passed through a -55 mm cylindrical lens that fans the beam out into a sheet. The laser sheet is ultimately scattered by a beam stop placed on the back side of the TCF

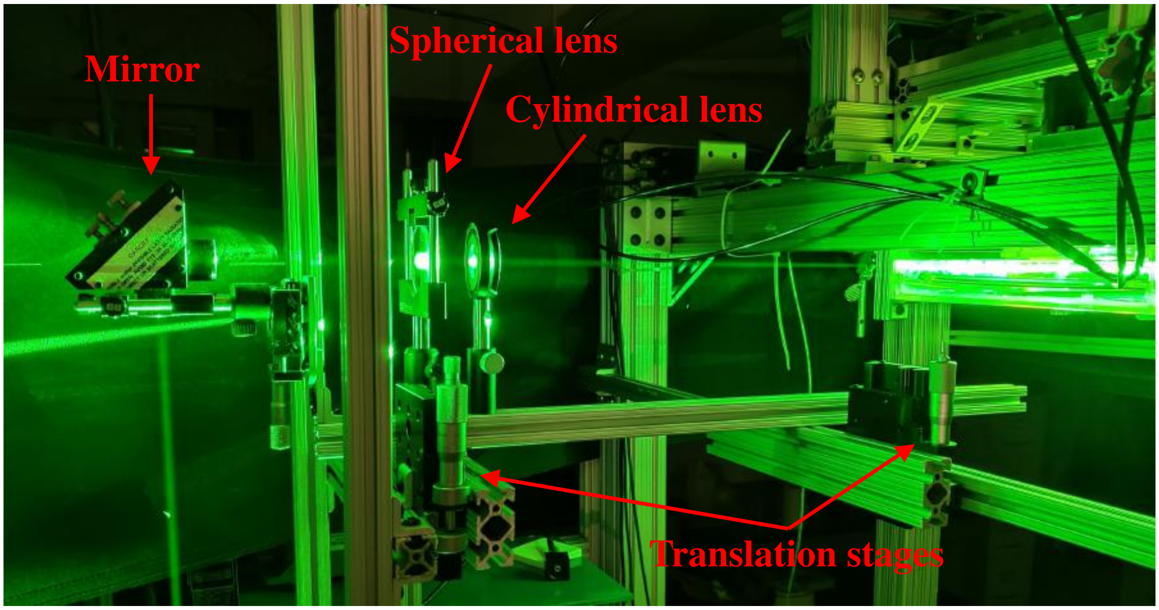

Figure 3.11: Picture of illuminating light sheet forming light optics for 2D-2C measurements. The mirror, spherical lens, and cylindrical lens are all mounted to the same bar that is suspended by two optical translation stages with micrometer adjustment screws.

to the relatively short optical path length, the optimal cylindrical lens focal length was chosen to be -50 mm. The cylindrical lens is held in a lens holder with a rotation mounting goniometer ring (see Figure 3.11) which allows for precision orientation of the optical axis of the lens.

The light sheet determines the plane of the 2D-2C measurement and therefore needs to be carefully aligned. The sheet forming optics are all mounted on the same bar that is suspended by two optical translation stages with micrometer adjustment screws. This allows for the pitch and height of the sheet to be adjusted independently. The alignment procedure begins by nominally adjusting the mirror so the laser beam passes through the exact center of the TCF cell. Once the beam is nominally adjusted, the spherical lens is added to the beam path ad adjusted until the beam is focused in the center of the cell. Next, the Cylindrical lens is added to the beam path after the spherical lens and adjusted until the laser sheet fully illuminates the entire width of the flow domain.

Once the light sheet is nominally adjusted to the desired plane, a more careful alignment needs to be performed. The coordinate system in the TCF experiment is defined relative to the bottom end cap and center of the axis of rotation of the two cylinders. This means that the bottom of the cell itself can be used as the reference plane for $z = 0$. To utilize this reference plane, blocks of known thickness can be used to temporarily raise the bottom of the cell up by the thickness of the blocks. The laser sheet can be adjusted until the plane is skimming the bottom of the cell which can be easily determined when the fluorescent tracer particles are settled to the bottom. Once the laser sheet is precisely aligned with the bottom of the cell, the blocks can be removed and the cell can be suspended by the registration pins. In principle, this alignment procedure allows for a placement of the plane to about 1 mm accuracy, however, for optimal comparisons the actual height needs to be determined from the data (see bellow for more details).

Identifying the axis of rotation in the data

PIV measurements require both space and time scale factors (i.e. to convert px/frame to m/s) as well as a proper choice of origin to be useful. The natural coordinate system for the TCF is a cylindrical coordinate system with its origin placed along the axis of rotation. PIV measurements perform correlations of pixels and typically provide image displacement fields in a uniform Cartesian coordinate system with the origin in the corner of the images. Therefore, a careful alignment of the origin is needed before the velocities can be transformed from Cartesian to cylindrical. To identify the center of the domain as well as provide a nominal spatial scale factor, the particle images are analyzed and an ellipse is fit to the edge of the flow domain.

To identify the boundary of the flow domain on the images, a few thousand images of the particles taken from the data set are superimposed to produce well defined region. Canny edge detection is then performed on the stacked image to produce well defined edges of the flow domain. the edge detection image is then cleaned up to remove all edges except the ones corresponding to the inner and outer cylinder. An ellipse is then fit to the two edges with a modified version of Fit_ellipse from the MATLAB File Exchange [141]. The choice of origin is then taken to be the average of the four focal points of the two ellipsis. Since the camera is placed very nearly exactly along the axis of rotation, the eccentricity of the two ellipsis are typically smaller than 0.06 which corresponds to a ratio of the semi-minor to semi-major axis of 0.9982 (or, 0.18 % out of round). An example of the resulting fit is shown in Figure 3.12. The code that performs this origin identification can be found in Section A.1.

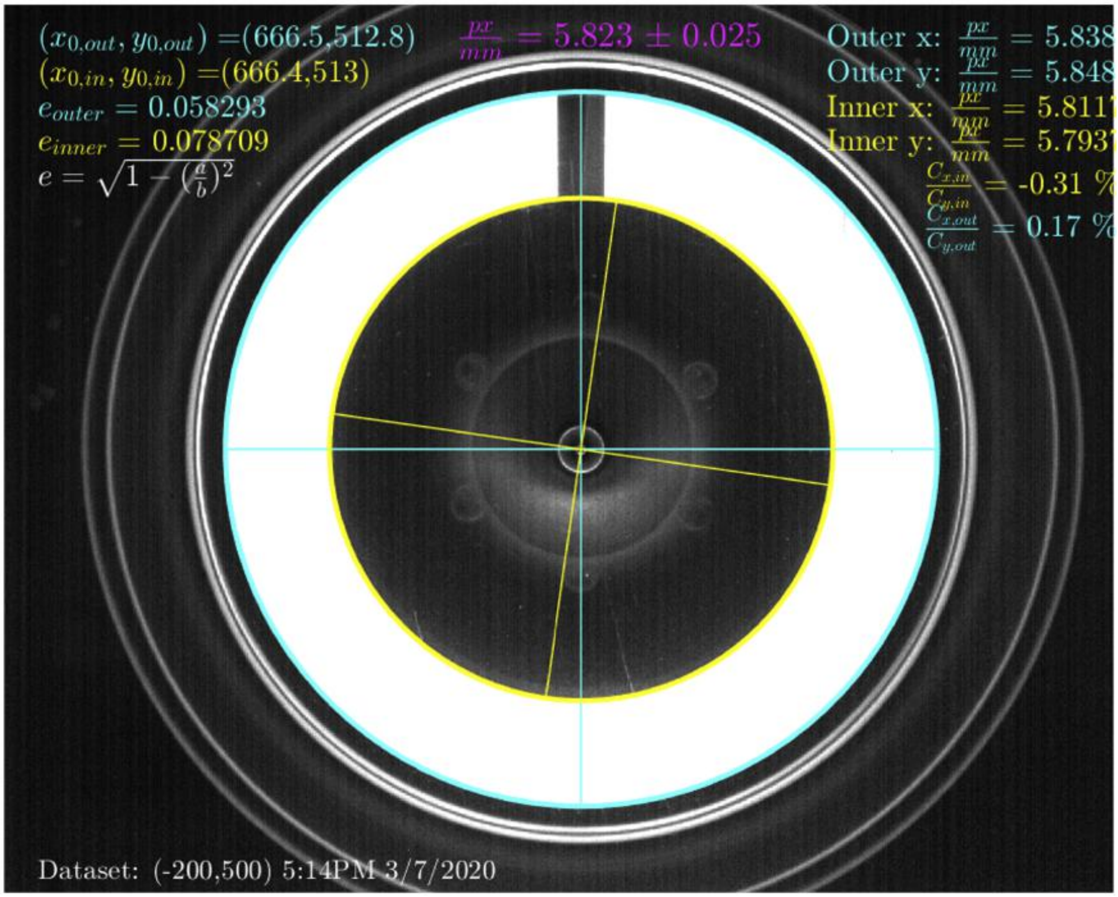

Figure 3.12: Example coordinate system origin determination by fitting an ellipse to the particle images. A few thousand images of the particles were superimposed giving a well defined boundary of the flow domain. The inner and outer edges of the domain are then fit to an ellipse and the eccentricity and origin is determined.

Find z-height

Making comparisons between the 2D-2C measurements and numerically computed flow fields requires the location of the measurement plane to be precisely known. The alignment procedure described above allows for the plane to be determined to about 1 mm accuracy, however the exact height needs to be known to better than 1 mm to make the best quality comparisons. The height and slight inclination of the plane can be relatively accurately determined by comparing the velocity profile of a laminar state with the numerically computed flow at the same $Re_{i,o}$ as a function of height.

The ideal laminar flow field to use for this comparison would be azimuthally symmetric and asymmetric about the mid-plane so that determined position is not degenerate in z. Additionally, at the $Re_{i,o}$ there would be only a single stable flow state. After a quick exploration, the laminar flow at $Re_i = 300$ and $Re_o = 0$ was found to be a suitable flow for this comparison. The θ-component of the velocity field as well as the radial velocity field is asymmetric about the mid-plane (see Figure 3.13).

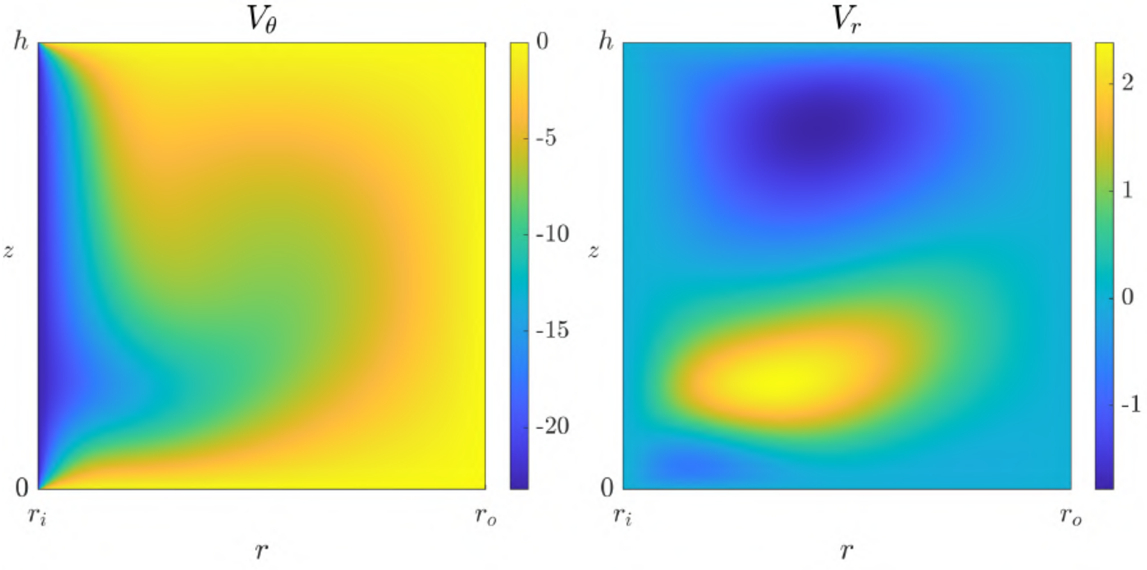

Figure 3.13: Numerically computed azimuthally symmetric, laminar flow at $Re_i = 300$ and $Re_o = 0$. Colors correspond to the magnitude of v_θ and v_r in units of mm$\cdot$s^{-1}.

Whenever making 2D-2C measurements of turbulence, the system is also prepared in the $Re_i = 300$ and $Re_o = 0$ laminar flow and a flow field is captured. The PIV velocity field, $\mathbf{v}_{\text{PIV}} = (v_{r,\text{PIV}}, v_{\theta,\text{PIV}})$, is then converted into cylindrical coordinates and compared with the laminar flow, $\mathbf{v}_{\text{Sim}} = (v_{r,\text{Sim}}, v_{\theta,\text{Sim}})$, computed in numerics. The height is determined by minimizing

$$F(z) = \left\| \left(\frac{v_{\theta,\text{PIV}} - v_{\theta,\text{Sim}}(z)}{U_{v_\theta}} \right)^2 + \left(\frac{v_{r,\text{PIV}} - v_{r,\text{Sim}}(z)}{U_{v_r}} \right)^2 \right\| \tag{3.6}$$

where U_{v_θ} and U_{v_r} are the uncertainty in the PIV measurements of the θ-component and r-component respectively and the $\| \cdot \|$ means summed over the entire plane. To greatly simplify the search for the measurement plane, the plane is assumed to be in good alignment with the cylinders. This allows $\mathbf{v}_{\text{Sim}}(r, z, \theta)$ to be evaluated only on planes of constant z. If the alignment of the plane is off from this assumption, Equation 3.6 would need to be modified to allow for searches over all possible planes.

An example of the resulting fit is shown in Figure 3.14. In this figure, the velocity profile of the numerical flow evaluated at the best fit height is shown in black. The black dashed lines are from the simulation velocity profile evaluated ±1 mm from the best fit height. In blue is the PIV data averaged around the entire azimuth. The PIV data clearly falls within the ±1 mm profiles for both the v_θ and v_r components in the center of the domain, but the uncertainty grows near either cylinder wall. This is due to a combination of several sources of PIV errors. The main source of increased uncertainty in the PIV is introduced by correlation windows near the wall partially laying outside of the domain where there are no particles, resulting in lower quality cross-correlations. Also, especially near the inner cylinder, the PIV fidelity drops in regions of higher shear due to the strong velocity gradient across the correlation window. This can be mitigated by implementing a deformable correlation window PIV algorithm [142], but the results of the z-height fit are adequate for the current purpose.

The slight angle that the PIV plane forms with the plane of constant z can be approx-

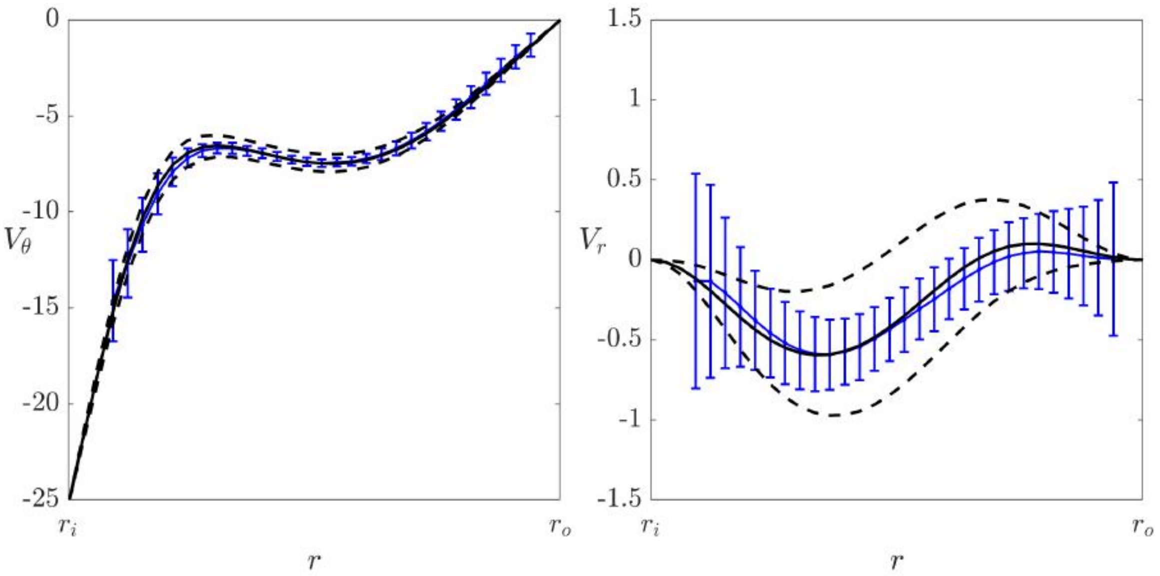

Figure 3.14: Example fit of experimentally obtained laminar flow to numerically computed flow to find optimal z-height. The black curve is the best fit, the dashed black curve is the best fit ± 1 mm, The blue data points and curve are the velocities obtained from 2D-2C PIV measurements.

imated by determining the optimal height of the plane as a function of θ. By fitting the optimal height as a function of θ to

$$z(\theta) = \frac{1}{2}\left(r_i + r_o\right)\left(m_x \cos\left[\theta\right] + m_y \sin\left[\theta\right]\right) + z_0 \tag{3.7}$$

as a function of the slopes m_x and m_y in the lab frame and the optimal height z_0, the deviation from the constant z assumption can be evaluated. If the slopes m_x and m_y are large, the optics can be easily adjusted to correct for this, as the degrees of freedom on the sheet forming optics are aligned with x and y. In the example shown in Figure 3.14, $m_x = 4.03 \times 10^{-3}$ and $m_y = 3.04 \times 10^{-3}$ corresponding to a $0.4°$ deviation from the plane of constant z. An example code that performs this height and inclination determination from simulation data is given in Section A.3.

The uncertainty in the value of z_0 determined by this optimization method depends on the uncertainty in the PIV, the uncertainty in the fit to Equation 3.7, and the uncertainty viscosity of the working fluid. Noise in the PIV manifests as noise in the determined value of $z(\theta)$. The uncertainty in $z(\theta)$, labeled U_{z_i}, are treated as uncorrelated with the uncertainty in the fit, U_{fit}. Therefore, they can be added in quadrature to estimate the uncertainty from the algorithm itself [143, 144, 145]. In addition to the uncertainty from the algorithm, the uncertainty in the measured value of viscosity, U_ν, corresponds to uncertainty in the velocity scaling of the numerically computed laminar solution, which in turn corresponds to an uncertainty in $z(\theta)$.

In order to calculate the total uncertainty in z_0, how changes in each of these three parameters affects the reported value of z_0 needs to be known. An uncertainty in the PIV translates to uncertainty in $z(\theta)$ in a complicated way through a series of interpolations and nonlinear fits. Additionally, the uncertainty in PIV, $U_{\text{PIV}}(\theta_i, r_i)$, is spatially dependant, but for the purposes of estimating the total uncertainty in z_0, it is taken as the spatial mean of the uncertainty $\langle U_{\text{PIV}}(\theta_i, r_i)\rangle_{\theta,r} = U_{\text{PIV}}$. A Monte Carlo study[24] was performed to determine the correspondence between U_{PIV} and U_{z_i} and found a linear relationship with a slope of $\dfrac{\partial U_{z_i}}{\partial U_{\text{PIV}}} = 0.706\,\text{s}$ between the two up to at least $20\,\%$ noise in the PIV. Similarly, the change in $z0$ due to a change in ν was computed numerically (up $10\,\%$ changes in ν) and found to be $\dfrac{\partial U_{z_0}}{\partial U_\nu} = 5.878\,\text{mm}\cdot\text{cSt}^{-1}$. To estimate U_{fit}, the square root of the $\sigma^2_{z_0}$ term of the co-variance matrix for the least-squares fit is used [146]. Combining these uncertainty estimates, the total uncertainty in the z-height is

$$\begin{aligned} U_{z_0}^2 &= \left(\frac{\partial z_0}{\partial z_i}\frac{\partial z_i}{\partial v_{\text{PIV}}}U_{\text{PIV}}\right)^2 + U_{\text{fit}}^2 + \left(\frac{\partial z_0}{\partial \nu}U_\nu\right)^2 \\ &= \left(1.775\times 10^{-3}\,U_{\text{PIV},\%}\right)^2 + \sigma^2_{z_0,\text{fit}} + \left(0.1005\,U_{\nu,\%}\right)^2, \end{aligned} \tag{3.8}$$

where $U_{\text{PIV},\%}$ is the uncertainty in the PIV expressed in % of the inner cylinder wall speed, $U_{\nu,\%}$ is the uncertainty in viscosity expressed in %, and $\sigma^2_{z_0,\text{fit}}$ is the uncertainty in the fit expressed in mm. The uncertainty in z_0 of the example shown in Figure 3.14 is 0.1068 mm.

---

[24] The Monte Carlo study was performed in two ways: adding Gaussian noise to a numerical laminar flow as an input to the algorithm and by adding Gaussian noise to actual PIV laminar data. The Monte Carlo simulation used more than 15,000 instances, which was found to be more than adequate to resolve the distributions of resulting z_0. The results of the study showed only slight differences between the numerical and experimental base flows used.

3.3.2 3D-3C

Setting up the illuminating light

Volumetric image velocimetry requires each particle to show up in the images as bright as particles in images for 2D-2C measurements. This means that the illumination intensity needs to be comparable to that of a light sheet throughout the entire measurement volume. 3D-3C measurement volumes are typically rectangular in shape and a powerful laser beam is expanded to cover the measurement volume. The geometry of the TCF cell, however, is not well suited for this illumination configuration and a more sophisticated illumination setup is required.

An annular beam can be produced with an axicon [147] lens inline with optics to produce a slight divergence of the laser beam. An axicon lens produces cone of light from a single beam in the far field. For columnated light, the thickness of the ring produced by the axicon is approximately equal to half the thickness of the incoming beam [148]. For slightly diverging beams, the thickness of the ring grows with the distance, z, from the lens. Similarly, the diameter of the ring grows as $d_{ring} \approx 2z\tan\left[(n-1)\,\alpha\right]$, where n is the index of refraction of the lens and α is the angle the surface of the axicon makes away from the lens plane. Given the distance between the optical table and the TCF cell and readily available axicon lenses, an axicon with $\alpha = 20°$ and $n = 1.457$ was chosen.

The thickness of the annular beam is adjusted by a pair of lenses placed just before the axicon lens. The beam coming out of the laser is not columnated, but has an angular divergence approximately $0.275°$ [149]. To produce a divergence such that the annular thickness large enough cover the gap width of the TCF cell, a single lens can be used[25]. Unfortunately, the single lens configuration would require an axicon lens with an aperture that is larger than any readily available. Therefore, a two-element variable focal power lens

---

[25] This can be done by treating the divergence of the laser beam as a columnated beam that has gone through a synthetic lens placed at a calculated distance before the outlet of the laser and using a two lens equation to calculate the geometric optics.

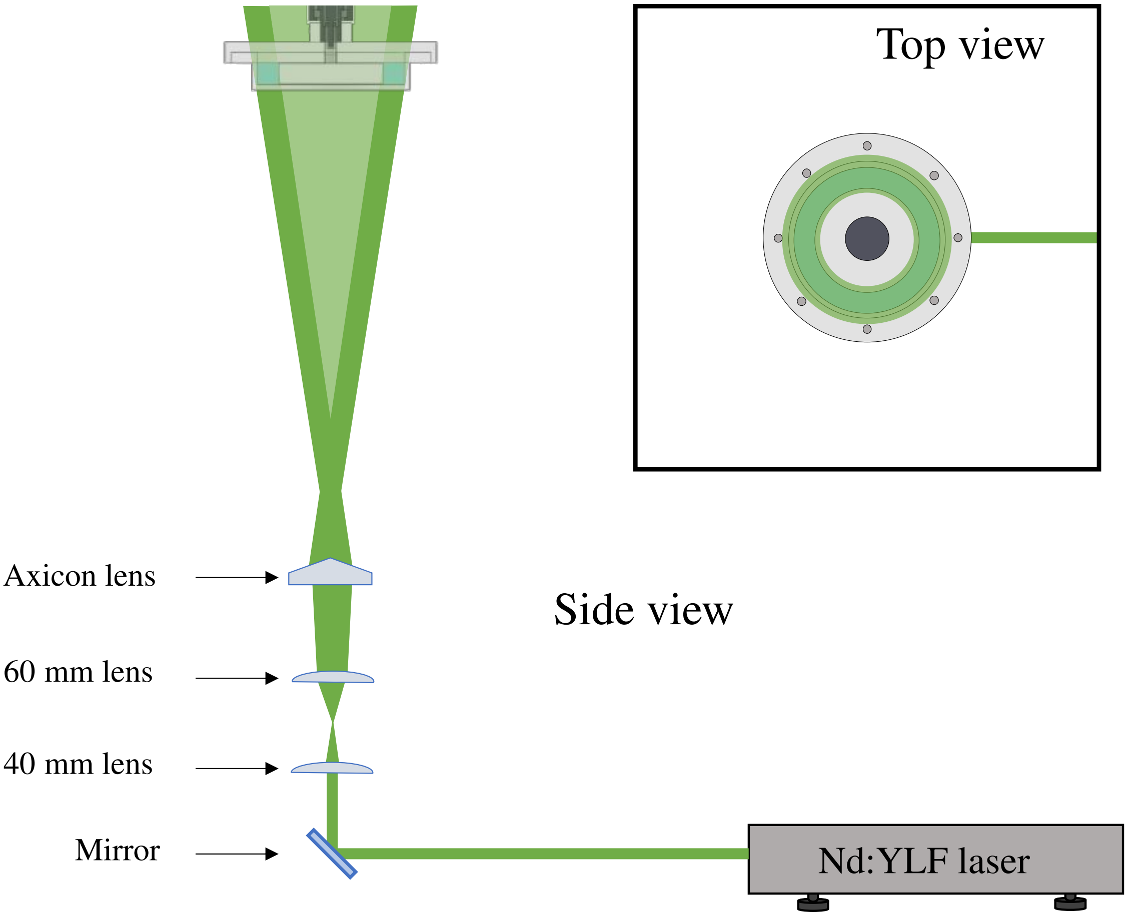

Figure 3.15: Schematic of illuminating light configuration for 3D-3C measurements. An annular shaped light beam is produced with a 20° axicon lens in conjunction with two positive focal length lenses. The two positive focal length lenses are positioned such that they produce a slightly diverging beam.

configuration [138] needs to be used. The two lenses used are a 40 mm focal length convex lens and a 60 mm focal length convex lens spaced at nearly the sum of their focal lengths apart. A schematic of this optical arrangement is shown in Figure 3.15. By adjusting the two convex and the axicon lenses, the annular illumination ring can be fitted to the flow domain. In practice, it is difficult to adjust the illuminating light since the working fluid and the cell walls are all transparent. To overcome this, a piece of printer paper can be used since it fluoresces at wavelengths that can be seen through the safety glasses (see Figure 3.16).

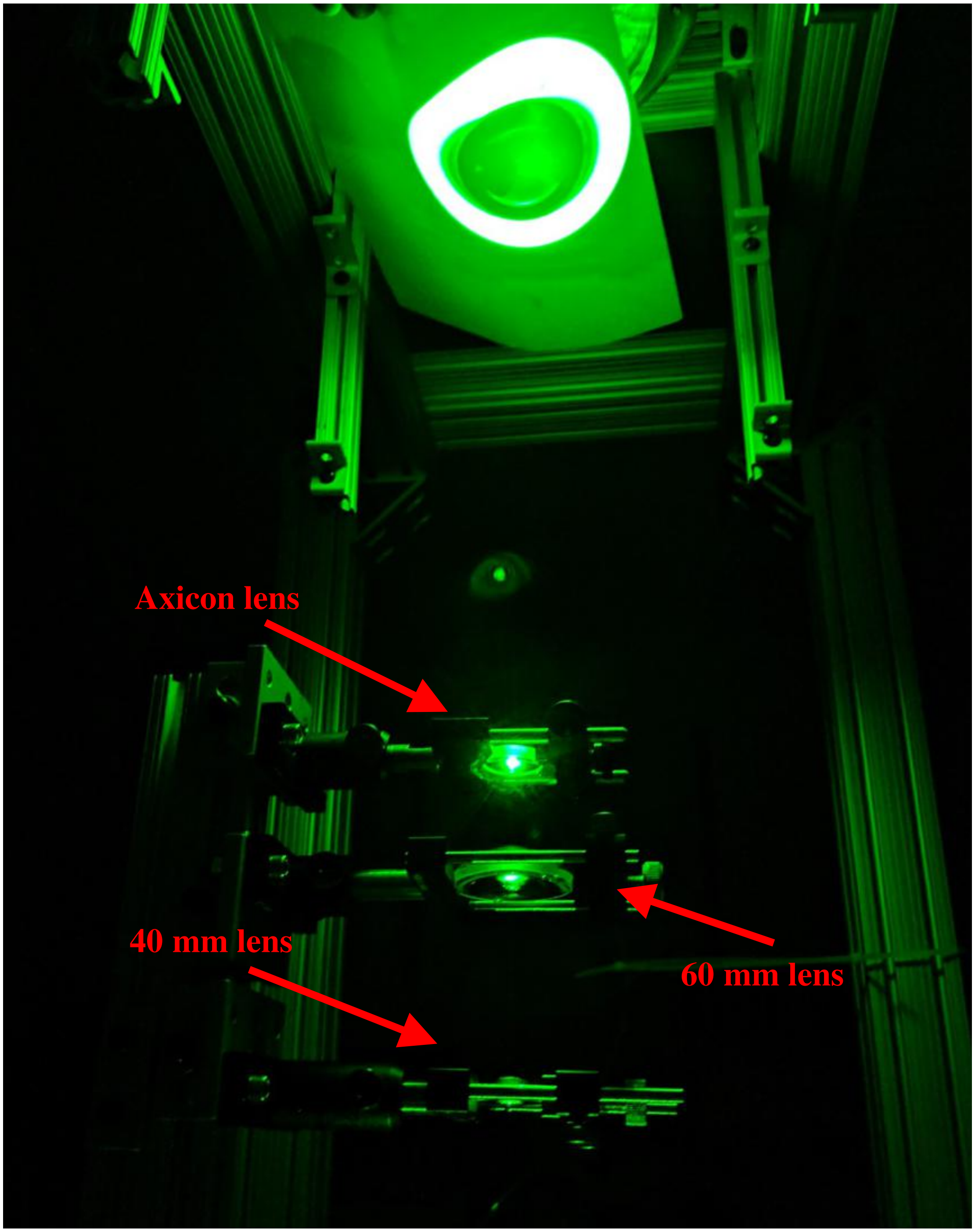

Figure 3.16: Picture of illuminating light optics for 3D-3C measurements. Note that the illuminating light produces an annular ring the same dimensions as the TCF cell.

Camera placement

3D-3C image velocimetry relies on images of tracer particles suspended in the flow taken from unique points of view. If the line of sight of each image transecting the flow is nearly co-linear to each other, the ability to reconstruct the dimension perpendicular to the images rapidly decreases [150]. Therefore, increasing the angle between the cameras improves the ability to identify the tracer particles position in all three dimensions. However, as the viewing angle increases, slight miss-alignments of the line of sight of the images due to calibration errors or camera movement become more important. At large viewing angles, the number of intersections of each line of sight ins creases, resulting in "ghost particles" [151, 82].

The ideal cameras viewing angle is a balance between increasing linear independence of each line of sight and decreasing the possibility of ghost particles. For a typical tomographic based experiment, the optimal camera viewing angle has been studied by Elsinga et al. 2006 [82]. They defined a metric, Q, that is the normalized correlation coefficient of the exact and reconstructed intensity distribution. Their results showed that the optimal viewing angle is $\theta_{\text{optimal}} \approx 30^\circ$, where θ is the half the angle between a camera, the measurement volume, and another camera (see Figure 3.9). The reconstruction quality doesn't change very rapidly around θ_{optimal} (see Figure 3.17), so viewing angles between 20° and 35° are ideal.

The cameras used in the TCF experiment are mounted on Manfrotto MHXPRO-BHQ2 ball head mounts (Vitec Imaging Solutions, Ramsey, NJ). The mounts are fastened to the 1 inch spaced threaded holes on the optical table. When the cameras are properly placed, the viewing angle between the camera sensor and the TCF cell is 30° and the angle in the plane of the table is maximized to still have the cameras fit on the table. The positions of the threaded holes that the camera mounts are attached to are given in Table 3.2. Each cameras field of view is not large enough to capture the entire flow domain, so the domain is split into two sides (A and B) and half the cameras view one side while the other cameras view

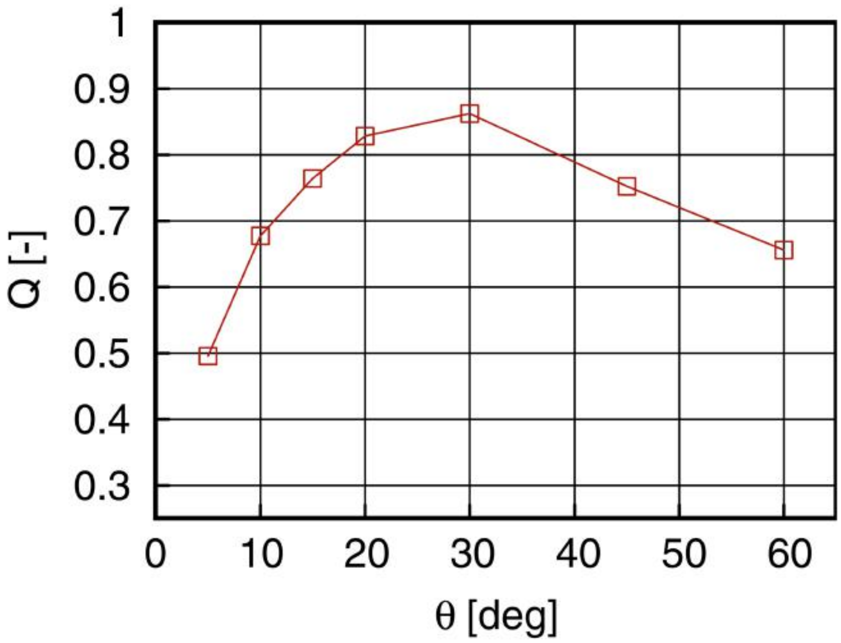

Figure 3.17: Quality of tomographic reconstruction of particle images for 3D-3C measurements as a function of viewing angle, see Figure 3.9. Q is defined as the normalized correlation coefficient of the exact and reconstructed intensity distribution and θ is the half the angle between a camera, the measurement volume, and another camera. Note that the optimal angle is closer to $30°$ than the intuitive $45°$. Figure taken from Elsinga et al. 2006 [82].

the other. The two sides are then stitched back together in post-processing so the entire flow domain can be analyzed. An example of the reconstructed particle tracks are shown in Figure 3.18.

calibration target design

All 3D-3C image velocity techniques require knowing the viewing angle of each pixel of every image. The uncertainty of this angle needs to be small enough to correspond to sub-pixel placement on the other cameras images[26] [82]. Determining each pixels line of sight is done in two stages; first, a perspective calibration using a calibration target to provide relatively precise angles followed by a calibration refinement performed on images of the

---

[26] The sub-pixel placement is defined in terms of the pixels "disparity" [152]. The disparity is determined by back-projecting the position of an object (e.g. a particle or dot on a calibration target) as determined by other cameras onto the image and comparing the difference in position between the two.

Table 3.2: Camera positions for 3D-3C velocimetry. Coordinates x and y correspond to number of threaded holes away from the axis of rotation of the experiment.

Camera	Side	x	y
1	B	-16	-17
2	A	-19	-4
3	B	-20	8
4	A	-15	18
5	B	15	18
6	A	20	9
7	B	19	-8
8	A	14	-17

particles. Together, these two calibration methods allow each pixels line of sight to be determined to less than 0.1 px.

The initial perspective calibration is performed by imaging a calibration target placed in the measurement volume. Multi-camera perspective calibrations have been practiced for several decades [153, 154, 155, 156]; however, the sub-pixel requirement is fairly recent. There are two traditional approaches to performing the target calibration, but one of them is more widely implemented. One method is to print a pattern that is random in space on a target and take images of it in the flow domain. The images are then cross-correlated with the pattern image itself to produce an image warping matrix [157, 158]. The other, and more common method is to produce a regular pattern of dots on a target and warp the image until the dot pattern becomes regular again [159, 160, 161]. In principal, both methods can be adapted to work for three dimensional calibrations, but the method involving regular dots is much simpler to implement.

For 3D-3C measurements, the calibration needs to provide information about the cameras perspective in all three dimensions. For the initial target calibration to do this, the calibration target needs either be precisely moved through the domain or be a three dimensional object itself [162]. A two dimensional, dot style calibration target can be imaged a several different regularly spaced depths of the measurement volume and the images can be ‘dewarped’ until the dot pattern is regular in all three dimensions. This method requires

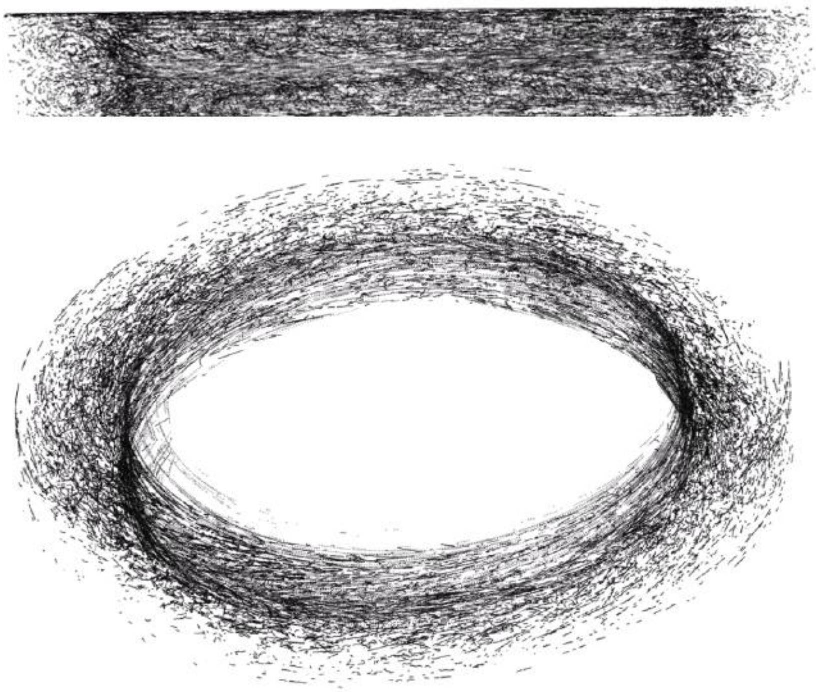

Figure 3.18: Example reconstructed particle tracks from turbulent flow at $Re_{\mathrm{o}}= -200$ and $Re_{\mathrm{i}}= 500$ using Shake-The-Box (STB). Each dot being shown represents the location of a reconstructed particle. This image was produced by superimposing several neighboring time-steps. A side view (top) shows that particles are reconstructed throughout the entire height of the flow domain and a top view (bottom) shows that the entire azimuth of the flow domain can be reconstructed.

a way to precisely place the target at several depths which is not always feasible. Alternatively, a calibration target that is itself three dimensional can be used. There is a large amount of freedom in the specific geometry of the three dimensional target that can be used for the three dimensional calibration and a brief discussion of the practical considerations of manufacturing a target is given in Appendix B.

Target calibrations are capable of providing perspective calibrations to the length scale of $\sim$1 pixel, but 3D-3C velocimetry techniques require $\leq$0.1 pixel. To achieve the sup-pixel calibration, a calibration refinement technique based on images of the particles called Volume Self-Calibration (VSC) has been developed [152, 163, 164]. The goal of the calibration is to identify a mapping, M, the image coordinates, (x_i, y_i), to the three dimensional space (X, Y, Z) for each of the N cameras:

$$(x_i, y_i) = M_i\,(X, Y, Z) \tag{3.9}$$

where the subscript i represents the i-th camera [159, 156, 162, 163]. VSC uses $N - 1$ cameras to identify the location of a particle and back projects that location onto the remaining camera. By searching in the vicinity of the back projected particle location for a particle, a small correction to M_i can be made. By iterating this procedure over many particles and over each camera, the mapping function M_i for each camera can be brought into agreement with the consensus from the other cameras. Although VSC provides a correction to the calibration, it is perhaps not strictly correct to refer to it as a calibration step since it allows for deviations from the calibration grounded in measurement.

3.3.3 Post-processing image velocimetry data

Both PIV and PTV produce velocity measurements with noise present. If the velocities are to be used for anything quantitative, minimizing the noise level is essential. Even in experiments where great effort has been spent to mitigate the sources of noise, there will still be noise in the data that lowers the fidelity of any analysis being performed on the data. Therefore, post-processing the velocity data is always needed. In general, there are a large number post-processing steps that can or need to be performed, but there are some operations that are applied to all velocimetry data. Bellow is a discussion of these operations.

Outlier detection and spatial smoothing

Velocity data determined from PIV is prone to erroneous or spurious velocity vectors. These vectors are caused by either an insufficient number correlated particles in the interrogation window or by a low signal-to-noise ratio in the particle images. This leads to a poor quality correlation and, as a result, the peak detection step finds an incorrect peak. Care can be taken in the setup and during data collection to minimize the number of these vectors, but it is almost impossible to completely eliminate them. Therefore, removing these erroneous vectors can substantially enhance the quality of the velocimetry.

The erroneous vectors can often be characterized by large deviations from surrounding vectors. In the case of a large deviation from surrounding vectors, outlier detection techniques [165, 166, 167, 168] can be implemented to remove the spurious vectors[27]. The removal of the local outliers leaves wholes in the velocity field that typically need to be filled in. To fill them in is a problem of data assimilation, but for relatively high quality PIV, this can be done by simply using polynomial interpolation without much loss of fidelity.

Outlier detection and removal is a relatively common among modern PIV implementations. For instance, LaVision's DaVis 10 (LaVision GmbH, Göttingen, Germany) has a built-in implementation of the Westerweel and Scarano 2005 method [167]. Some variant of outlier detection is an almost essential step in modern high quality PIV measurements [170] and therefore should be performed on every PIV data set.

Anisotropic denoising

After erroneous velocity vectors have been removed, PIV data still has noise present. The noise produced by PIV is not spatially uniform; therefore, to efficiently reduce the noise, a denoising approach that is anisotropic in space is needed. In order to inform an anisotropic denoising algorithm, an estimate of the quantification of the spatially dependant uncertainty of the PIV is needed. There are many contributions to the uncertainty of a single velocity vector such as the PIV algorithm itself, the particle response to the flow, particle seeding density, particle scattering cross-section distribution, and collection optics to name a few. A proper quantification of the uncertainty would use *a priori* estimates for all sources related

---

[27] Though the technique is most developed in the context of PIV data, implementations of outlier detection has been formulated to work for PTV data as well [169].

to the experiment and would combign that with a *a posteriori* estimate of the uncertainty introduced by the algorithm itself.

There are many approaches that have been introduced to estimate the uncertainty of PIV. Some of these approaches have been based on *a priori* estimates [106, 171], but they have been shown to not capture well the variations from experiment to experiment [172]. There are a variety of approaches that calculate an estimate of the uncertainty from the data itself such as the uncertainty surface approach [173], the particle disparity method [174], the peak ratio method [175] and the correlation statistics approach [172, 176, 177, 178]. In principal, all of these *a posteriori* methods are suitable for use with an anisotropic denoising algorithm.

To date, there is only one published approach to anisotropic denoising of PIV data. This approach was published in 2017 by Wieneke [179] and uses the local variation in the uncertainty to adapt the kernel of a smoothing algorithm. The algorithm has been found to provide a huge improvement to the quality of the PIV data captured in the studies presented in this thesis and should be considered an essential post-processing step for all PIV data.

Putting data on a spectral grid

PTV produces velocity vectors nonuniformly distributed in space which can make comparing to numerics difficult. For velocity data captured from PTV, it is useful to represent the data on a grid for easy comparison with numerics. There are many approaches for interpolating data which lies on a grid onto another grid [180], however, none of the standard methods can put the data on a spectral grid.

A spectral grid has two possible advantages: the numerics are computed on a spectral grid and a spectral grid allows for data everywhere in the domain to contribute to the value even in regions with sparse velocity data. The latter is both an advantage and a possible disadvantage since it allows for higher mode numbers to blow up. This means that whenever putting the data on the spectral grid, care must be taken to ensure that modes are not blowing up.This can be done by balancing a minimum fit residual with reducing the number of modes used.

For easy comparison with numerics, the grid used in the numerics should be used. In the numerics each component (e.g.. $v_{r,\theta,z}$) is calculated on its own spectrum:

$$v_{r,\theta,z}(r,\theta,z,t) = \mathrm{Re}\left\{ \sum_{k=0}^{N_r} \sum_{n=0}^{N_z} \sum_{m=0}^{N_\theta/2} V_{r,\theta,z}^{knm}(t) T_k(x) T_n(y) e^{im\theta} \right\}, \tag{3.10}$$

where $x = (2r - r_{in} - r_{out})/d$, $y = 2z/d - 1$ (where $0 < z < d$), $\mathrm{Re}\{\cdot\}$ is the real part, and $T_n(\cdot)$ is the Chebyshev polynomial (of the first kind) of order n. The data can be put into this representation by fitting the data to determine $V_{r,\theta,z}^{knm}$.

The data is fit to the grid with a simple least squares approach. This method allows for the data to be weighted by the vector-wise uncertainty, but makes enforcing the boundary conditions challenging. In order to enforce the the boundary condition, synthetic data points are generated at the location of the inner and outer cylinders and given the boundary condition velocity. The boundary condition enforcing synthetic data points are appended to the velocity data and assigned a weight factor 100 times larger than the weight of the rest of the data. An implementation of this spectrum fitting method is given in Section A.2.

CHAPTER 4

TRANSITION TO TURBULENCE IN $\Gamma = 5.26$ TAYLOR-COUETTE FLOW

The transition to turbulence in TCF is typically thought of as occurring through a series of bifurcations of simpler, non-turbulent states. However, as Γ gets smaller, the end effects begin playing a key role and the transition begins resembling the transitions to turbulence observed in shear driven flows (e.g. pipes, channels, and boundary layers). To explore this, lets first look at at a TCF system where the end effects are important but do not dominate the flow. In $\Gamma = 5.26$ TCF exhibits a novel transition to turbulence that is mediated by an intermediate, stable flow state. In the following sections we will discuss the methods used to probe this transition as well as briefly describing some of our findings in this system.

4.1 Methods

Our TCF apparatus with $\eta = 0.905$ was composed of a glass outer cylinder with a radius of $r_o = 80.03$ mm± 0.02 mm and a brass inner cylinder of radius $r_i = 72.39$ mm± 0.01 mm with a black powder coat to enhance optical contrast in flow visualization studies. The aspect ratio, $\Gamma = 5.26$, was set by two end caps, separated axially by $h = 40.2$ mm± 0.05 mm and attached to rotate with the outer cylinder. The cylinders were driven by stepper motors; to reduce vibration and to ensure uniform cylinder rotation, timing belts connected the cylinders to the motors, which were mounted separately from the TCF apparatus. Additionally, a transmission with a gear ratio of 28:1 was used with the inner cylinder stepper motor to increase the resolution in Re_i. While the cylinders were rotating, the rate of temperature variations in the flow was kept below 0.5 °C throughout the duration of the experiments by surrounding the outer cylinder with a liquid bath. With these measures, the total systematic uncertainty for Re_i and Re_o was below 1 %.

In the tomo PIV results discussed here, determination of 3-D velocity fields were made throughout a flow volume with an approximate size of d radially, $0.75h$ axially, and $2\pi r_o/10$ azimuthally. Custom-made, density-matched polyester particles (25 µm to 32 µm in diameter) were doped with Rhodamine 6G and suspended in the flow. A more detailed discussion of these particles is given in subsubsection 3.2.1. The particles were illuminated with a Quantronix 527/DP-H Q-switched Nd:YLF laser. Fluorescent light emitted from the particles was collected by four Vision Research Phantom V210 high speed cameras synchronized with the laser illumination. Each camera was fitted with a 105 mm Nikon Nikkor fixed focal length lens attached via a Scheimpflug adapter (LaVision Inc.). A low pass optical filter (Semrock BLP01-532R-25) on each camera lens attenuated, by a factor of 10^7, the scattered 527 nm wavelength laser illumination and passed, with 80 % efficiency, fluorescent light at wavelengths $>$532 nm. The images were then analyzed using LaVision Inc.'s DaVis tomographic PIV software package. To reduce optical distortion from the outer cylinder's curved surfaces, the index of refraction of both the working fluid and the bath liquid were matched to the index of refraction of the glass outer cylinder. Index matching of the working fluid was achieved by using an ammonium thiocyanate solution prepared with a specific gravity of 1.13 and a kinematic viscosity of $\nu = 1.37\,\mathrm{mm}^2{\cdot}\mathrm{s}^{-1}$ at 23° C [127]. A small amount of ascorbic acid was added to the ammonium thiocyanate solution to mitigate reaction with trace metals [136]. Index matching of the bath liquid was achieved by a binary mixture of two mineral oils with a 68.8 % heavy viscosity oil (McMaster-Carr part no. 3190K632) to 31.2 % light viscosity oil (McMaster-Carr part no. 3190K629) ratio. Further details about the implementation of tomo PIV measurements in our TCF apparatus are reported elsewhere [89].

Fully resolved direct numerical simulations (DNS) of TCF were conducted using the code developed by M. Avila and his collaborators [181, 182, 183]. This code uses a pseudospectral scheme to solve the Navier-Stokes equation in cylindrical coordinates subject to physical (no-slip) boundary conditions at the surface of the rotating concentric cylinders and top and bottom end caps. Details of how this code works can be found in Crowley *et* *al.* 2020 [25].

To quantify flow fields in both simulations and experiments, the perturbation flow field

$$\widetilde{\mathbf{v}}(t) = \mathbf{v}(t) - \mathbf{v}^{\mathrm{lam}}, \tag{4.1}$$

characterizes the deviation of the full flow $\mathbf{v}(t)$ from an axially symmetric laminar flow $\mathbf{v}^{\mathrm{lam}}$ computed numerically at the same Reynolds numbers. The numerically computed $\mathbf{v}^{\mathrm{lam}}$ was used to compute the perturbation flow field for both simulations and experiments since the laminar flow is unstable for some Re_i considered in this study, and, therefore, unobservable in the laboratory experiments.

4.2 Results

First, we briefly describe a coarse experimental exploration of laminar-turbulent (turbulent-laminar) transitions that occur as Re_{i} is slowly increased (decreased) while maintaining Re_{o} fixed in the counter-rotating regime. We then focus on the case of $Re_{\mathrm{o}} = -1000$ and examine in detail the transitions associated with increasing and decreasing Re_{i} using both laboratory experiments and numerical simulations.

4.2.1 Laminar-Turbulent Transition: Dependence on Re_{o}

To coarsely map out the transition boundaries for TCF in the geometry studied here, we performed flow visualization experiments by first spinning up the outer cylinder from rest (with the inner cylinder stationary) to a specific value of Re_{o}; then, with Re_{o} held constant, Re_{i} was increased in steps of $\Delta Re_{\mathrm{i}} = 10$ by slowly stepping up the rotation rate of the inner cylinder until a qualitative change in the flow was observed. We waited a time interval of $3.2\,\tau$ between steps to ensure that the flow had reached equilibrium. The turbulent-laminar transition boundary at the same Re_{o} was then determined by starting in the turbulent regime and slowing the inner cylinder down by $\Delta Re_{\mathrm{i}} = 10$ every $3.2\,\tau$ until the flow was observed to be in the laminar state. The experiments were repeated for different fixed values of Re_o.

The experimental studies revealed instability of the azimuthally symmetric smooth laminar flow always leads to turbulence over a range of Re_o from -3500 to -500 (Figure 4.1). The transition back to laminar flow was always observed to be hysteretic; the range in Re_i over which hysteresis occurs increases as the magnitude of Re_o increases. Our results indicate that transition from laminar flow is suppressed by the moderate aspect ratio of our apparatus, i.e., for fixed Re_o, the transition occurs at Re_i larger than that predicted by linear stability analysis with $\Gamma = \infty$ (gray line in Figure 4.1). This observation is consistent with earlier experiments at larger values of Γ (and somewhat smaller values of η) where, like our studies, the end caps rotated with the outer cylinder [71]. In that work, the delay of laminar flow transition was found to increase with decreasing Γ, most likely due to the end-wall effects (e.g. dissipation and Ekman pumping) that become more pronounced as Γ decreases.

4.2.2 Flow Transitions at $Re_\mathrm{o} = -1000$

A detailed experimental and numerical investigation at fixed $Re_\mathrm{o} = -1000$ led to the observation of an intermediate state that plays an important role in the laminar-turbulent transition. The transition from turbulence to laminar flow was found to involve an aperiodic stable intermediate state (interpenetrating spirals) that persists over a range of Re_i. Moreover, IPS were found to appear – albeit transiently – during the transition from laminar flow to turbulence. Transitions between different flow states are described in detail below.

Transitions in Laboratory Experiments

Transitions were determined in flow visualization studies by first spinning up the outer cylinder to $Re_\mathrm{o} = -1000$ (with the inner cylinder at rest), and then increasing the inner cylinder's counter-rotation in steps of $\Delta Re_\mathrm{i} = 0.5$ every $3.2\,\tau$, until the flow became turbu-

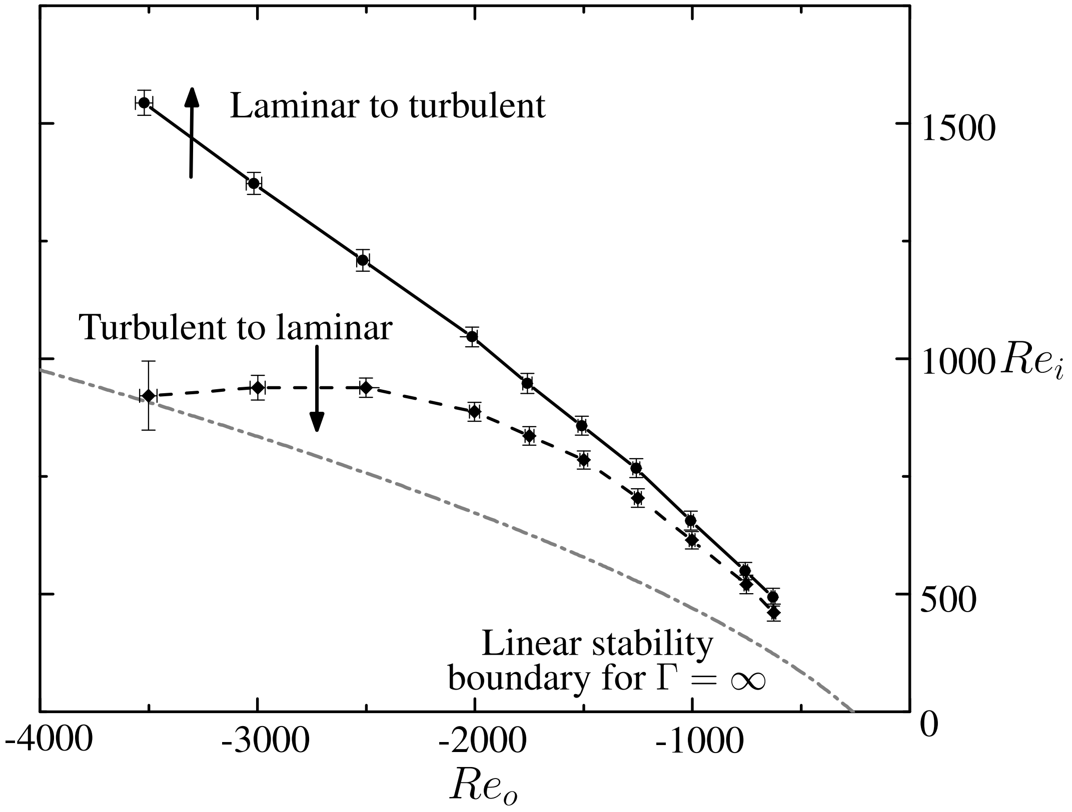

Figure 4.1: Phase diagram illustrating the hysteretic laminar-turbulent transition in experiments on counter-rotating ($Re_\mathrm{o} < 0$ and $Re_\mathrm{i} > 0$) Taylor-Couette flow with $\Gamma = 5.26$ and $\eta = 0.905$. The diagram indicates transitions observed in experiments where Re_i was increased or decreased quasi-statically while keeping Re_o fixed. The black solid and dashed lines, drawn to guide the eye, indicate the transition boundaries from laminar flow to turbulence and from turbulence to laminar flow, respectively. The gray dash-dotted line represents the marginal stability curve for TCF at $\eta = 0.9$ for $\Gamma = \infty$ [184].

Table 4.1: The inner cylinder Reynolds numbers for flow transitions are shown for both laboratory experiments and numerical simulations at $Re_\mathrm{o} = -1000$. Uncertainty values from the experiment reflect the systematic uncertainties associated with the measurement of Re as well as repeatability of the transition, while the uncertainty values from the noiseless DNS reflect the resolution with which the dependence on Re_i was investigated. The uncertainties in experimental values were calculated using an uncorrelated linear propagation of uncertainties associated with all measured quantities and measurement repeatability represented by the standard deviation.

Transition	**Experiment**	**Noiseless DNS**
Laminar → Turbulence	643 ± 2	675 ± 5
Turbulence → IPS	625 ± 3.6	623.5 ± 0.5
IPS → Turbulence	631 ± 3.7	630.5 ± 0.5
IPS → Laminar	617 ± 1	617.5 ± 0.5

lent. Subsequently, beginning from the turbulent state, Re_i was decreased at the same rate as before until the flow returned to the laminar state. No observable shifts in the transition boundaries were found when incrementing or decrementing Re_i in steps of $\Delta Re_\mathrm{i} = 0.25$ separated in time by $10.7\,\tau$.

With the flow starting in a laminar state, laboratory experiments exhibit a laminar-turbulent transition at $Re_\mathrm{i} = 643$ with a total uncertainty in Re_i of ± 2. Repeated measurements demonstrate the transition can be observed with a resolution of ± 0.13 (i.e. 0.02 %), as constrained by the mechanical limits of the motor and transmission driving the inner cylinder; in other words, from laminar flow just below threshold (cf. Figure 4.2(a)), a single increment of $\Delta Re_\mathrm{i} = 0.13$ results in turbulence. At onset (with Re_i fixed), the structure of the flow changes slowly at first; very weak interpenetrating spirals gradually become discernible and grow slowly in amplitude with time (cf. Figure 4.2(b)). Then, abruptly, the spirals break up and spatiotemporally intermittent turbulence develops on top of an IPS-like background flow and persists (cf. Figure 4.2(c)). The interval of time over which the flow resembles IPS before transitioning to turbulence was different each time the experiment was performed and this interval decreased with an increase in the increment size of ΔRe_i. If Re_i is increased stepwise (with a fixed time interval of $3.2\,\tau$ between each step), the transition Re_i is unchanged for increments of $\Delta Re_\mathrm{i} < 1$; the transition Re_i is observed to decrease for increments of $\Delta Re_\mathrm{i} > 1$.

Starting from turbulent flow, decreasing Re_i reveals a transition to stable IPS at $Re_\mathrm{i} = 625 \pm 3.6$. IPS were observed to be weakly chaotic (i.e., having a broad-band temporal spectrum) over a range of Re_i and persist for as long as $3.8 \times 10^3\,\tau$ (two and a half days, after which time the experiments were ended). From stable IPS, increasing Re_i leads to a transition back to intermittent turbulence at $Re_\mathrm{i} = 631 \pm 3.7$; decreasing Re_i leads instead to a transition to the axisymmetric laminar state at $Re_\mathrm{i} = 617 \pm 1$. It should be noted that the values of Re_i at which various transitions are observed (see Table 4.1) depend on disturbances of two qualitatively different types: (a) disturbances associated with a discrete

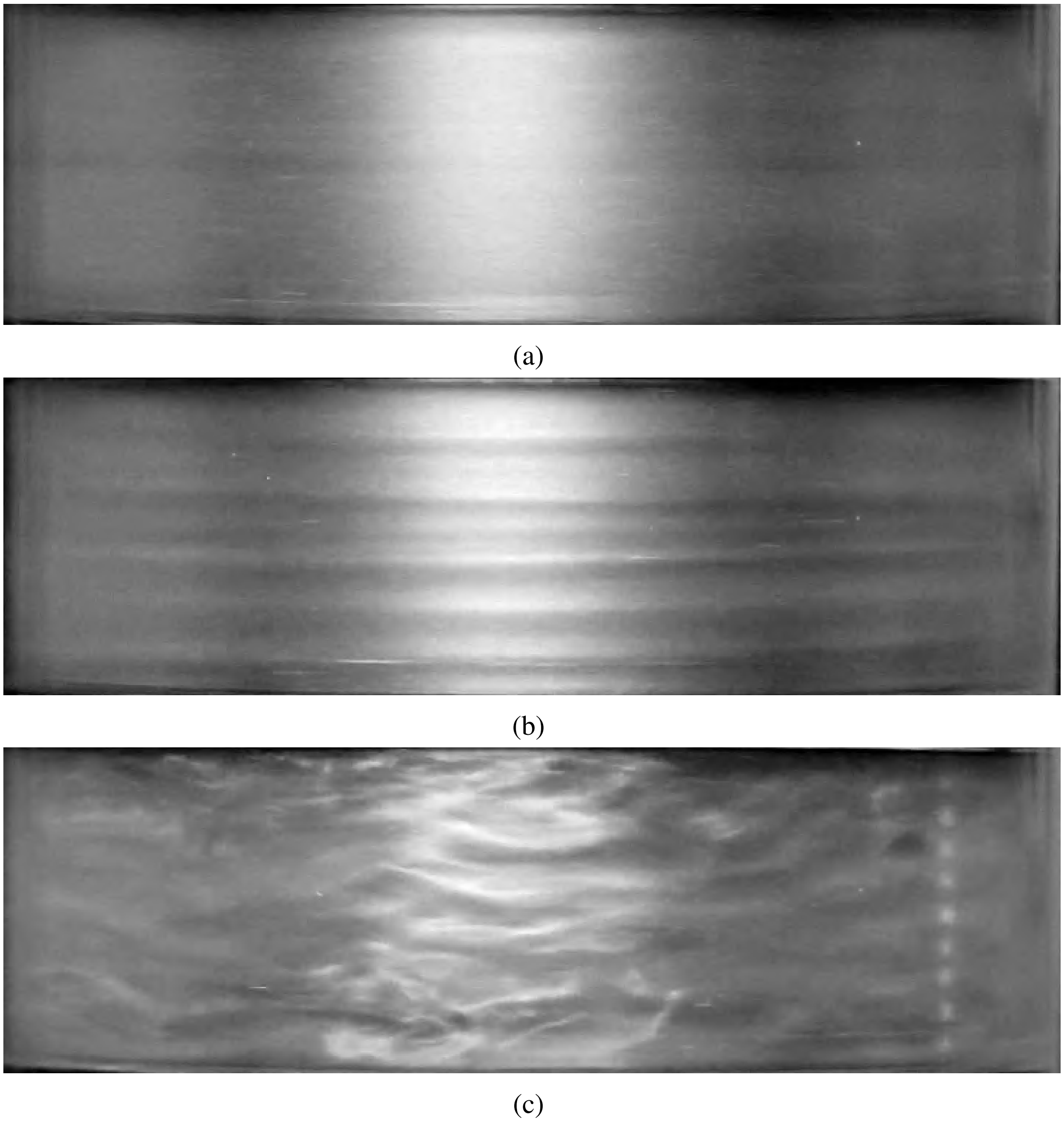

Figure 4.2: Evolution of the flow during laminar to turbulent transition in experiments at $Re_\mathrm{o} = -1000$ and $Re_\mathrm{i} = 643$. The sequence of snapshots shows (a) the initial laminar flow, (b) transient interpenetrating spirals, and (c) persistent intermittent turbulence.

change of Re_i and (b) other types of disturbances (e.g., the cylinders not being perfectly round or coaxial, the deviation in their angular velocity from a constant, etc.). All of these are disturbances of a finite, though likely small, amplitude.

Quenching experiments can provide information on the transition from chaotic/turbulent states that is complementary to results obtained via quasi-static changes in Reynolds number [185, 59, 186, 60]. A typical quenching experiment begins with the flow in a chaotic/turbulent state at fixed Reynolds numbers. At an instant in time, Re_i is abruptly increased or decreased to a new value and held constant; the subsequent "lifetime" of the flow (the time required for the initial flow to change to a qualitatively different state) is determined. Repeating the same experiment often yields a distribution of measured lifetimes, which provides insight into the nature of the transition. To probe the transition from turbulence to IPS, a turbulent state at $Re_\mathrm{i} = 640$ was first established and monitored for $5.3\,\tau$; the inner cylinder rotation was then rapidly (in approximately $4.2 \times 10^{-3}\,\tau$) reduced to $Re_\mathrm{i} = 623$. The time interval between the reduction in Re_i and the disappearance of turbulence was recorded. Similarly, to probe the transition from IPS to turbulence, we initially set $Re_\mathrm{i} = 623$. The IPS was monitored for $5.3\,\tau$; then, the inner cylinder rotation was rapidly (in approximately $4.2 \times 10^{-3}\,\tau$) increased to $Re_\mathrm{i} = 640$ and the time interval between the increase in Re_i and the first appearance of turbulence was recorded.

Figure 4.3 summarizes the results from 250 experiments performing the same cycle of transitions between turbulence and IPS; the data indicate a clear exponential distribution of intervals between the time when the inner cylinder rotation rate is changed and the time for turbulence either completely disappears (cf. Figure 4.3 (a)) or first appears (cf. Figure 4.3 (b)). The exponential distribution suggests that both transitions describe a memoryless Poisson process, with a chaotic attractor at the initial Re_i becoming a chaotic repeller at the final Re_o. There are, however, different scenarios that could gives rise to exponential distribution of transition times such as a boundary crisis bifurcation [188, 189] and a noise-induced transition [190]; to determine the specific mechanism at play here, further

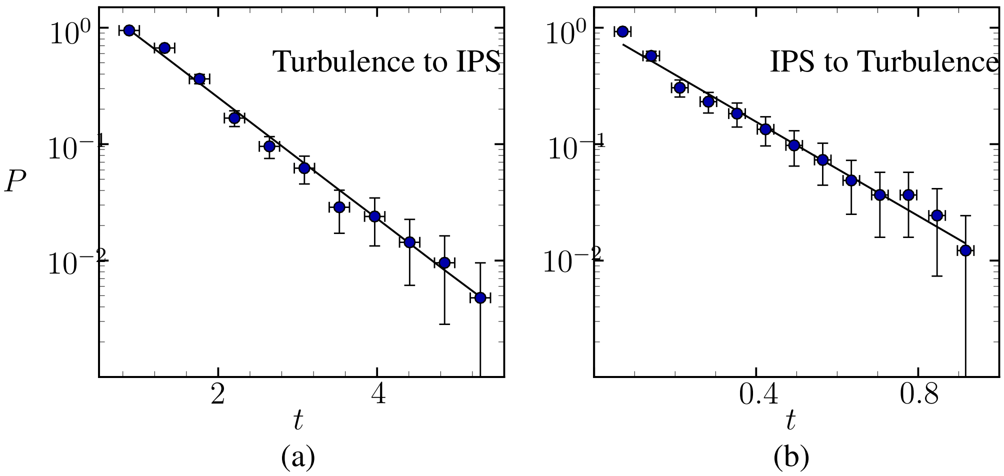

Figure 4.3: Transition probability $P(t)$. After an abrupt change in Re_i, the transition time for turbulence to either (a) disappear or (b) first appear is exponentially distributed. $P(t)$ indicates the fraction of experimental trials where either (a) turbulence still persists after changing Re_i from 640 to 623 or (b) turbulence has not yet appeared after changing Re_i from 623 to 640. The uncertainty bars in the vertical direction describe the uncertainty $U_P = \sqrt{f(1-f)/N}$, where $f(t)$ is the fraction of the number of events where turbulence survived for longer than time t and N is the total number of events observed [187].

investigation would be needed. Similar distributions of transition lifetimes were found in relaminarization studies of high-aspect-ratio TCF [60].

Quenching experiments were also performed for the transition from stable IPS to laminar flow; however, due to the discreteness with which Re_i could be varied in experiment, we could not find a final Re_i for which a meaningful distribution of lifetimes could be observed.

Transitions in Numerical Simulations

Numerical simulations were used to determine linear stability of the steady axisymmetric laminar flow $\mathbf{v}^\mathrm{lam}$. This flow was generated at $Re_\mathrm{o} = -1000$ and different fixed Re_i by keeping only the azimuthally symmetric mode and evolving the state until it stopped changing. The azimuthal symmetry of this flow was then broken by perturbing the first Fourier mode (with the nonlinear term generating disturbances for all other modes). Evolving the perturbed flow, we found that the perturbation decays (the laminar state is linearly stable) for $Re_\mathrm{i} < Re_\mathrm{i}^c = 675 \pm 5$ and grows, resulting in a transition to turbulence, for $Re_\mathrm{i} > Re_\mathrm{i}^c$.

Since the laminar flow undergoes transition to turbulence in experiment at a notably lower Re_i than the linear stability threshold Re_ic, an investigation of its stability to finite amplitude disturbances was performed. Qualitatively, we find that, for $Re_\mathrm{i} \geq 634$, finite amplitude perturbations lead to destabilization of the laminar state, giving rise to IPS with an amplitude that grows and saturates temporarily. Ultimately the IPS gives way to spatiotemporally intermittent turbulence, just as in the experiment. Qualitatively the same transition sequence was found to occur for initial disturbances with different magnitudes and spatial profiles.

To quantify qualitatively how the critical disturbance amplitude depends on Re_i, we fixed the spatial profile of the disturbance by choosing the initial condition in the form of a homotopy

$$\mathbf{v} = (1-\alpha)\mathbf{v}^{\mathrm{lam}} + \alpha\mathbf{v}^{\mathrm{IPS}}, \tag{4.2}$$

where $\mathbf{v}^{\mathrm{lam}}$ is the laminar flow at the given Re_i and $\mathbf{v}^{\mathrm{IPS}}$ is a snapshot of the (nonaxisymmetric) IPS at $Re_\mathrm{i} = 630$. The structure of the IPS is fairly similar at different Re_i; thus, for the purpose of determining critical disturbance amplitudes, we considered it to be sufficient to compute $\mathbf{v}^{\mathrm{IPS}}$ at a fixed Re_i. The homotopy parameter $0 \leq \alpha \leq 1$ characterizes the magnitude of the disturbance; increasing α increases the disturbance amplitude. This particular choice of homotopy guarantees that initial conditions are divergence-free for any value of α.

Numerical simulations find the same sequence of transitions as laboratory experiments when the flow is initially turbulent. Decreasing Re_i first leads to a transition to stable IPS at $Re_\mathrm{i} = 623.5 \pm 0.5$. From stable IPS, increasing Re_i leads to a transition back to turbulence at $Re_\mathrm{i} = 630.5 \pm 0.5$, while decreasing Re_i leads to a transition to the time-independent laminar state at $Re_\mathrm{i} = 617.5 \pm 0.5$. These numerically determined transition Reynolds numbers between IPS and turbulence and from IPS to laminar are quantitatively in agreement with those found in laboratory experiments, as illustrated in Table 4.1. Due to the subcritical nature of the transition between laminar and turbulence, however, the appropriate choice of the finite amplitude perturbation, α, is required.

The protocol for determining $Re_{\rm i}$ for transition from turbulence to IPS is as follows: We started with verifying that turbulence persists at $Re_{\rm i} = 640$ by evolving the flow for a time interval $5.264\,\tau$. Then we ramped down $Re_{\rm i}$ in increments of $\Delta Re_i = 5$ and evolved the flow for the same interval to determine whether a transition occurred. Once a transition was detected (at $Re_i = 620$), we re-initialized the flow using the final state of the simulation at $Re_i = 625$, decreased the Reynolds number by $\Delta Re_{\rm i} = 1$, and evolved the flow for a further $5.264\,\tau$. The procedure was repeated with $\Delta Re_{\rm i} = 2, 3, \cdots$ until a transition was found.

A similar protocol was used for the two transitions from stable IPS. In these cases, we verified that stable IPS persists at $Re_{\rm i} = 620$ and 630. The final states of the simulation at $Re_{\rm i} = 630$ (or $Re_{\rm i} = 620$) were evolved for $5.264\,\tau$ at a fixed Re_i that was increased (or decreased) by $\Delta Re_{\rm i} = 1, 2, 3, \cdots$ until transition to turbulence (or laminar flow) was found. Note that, in all of these cases, only one simulation was performed and the finest resolution was $\Delta Re_{\rm i} = 1$, which determines the accuracy of the values reported in Table 4.1.

Given ample experimental evidence that the transitions between turbulence and IPS are probabilistic [25], we did not investigate these transitions numerically in more detail. For the transition from IPS to laminar flow, however, experiments did not conclusively determine the nature of the transition. We therefore performed an additional numerical investigation of this transition by evolving IPS at a number of fixed $Re_{\rm i}$ in the range $(617, 618)$. While most of the results were consistent with a transition threshold found previously, there were a few outliers. In particular, we found that evolving IPS for $5.264\,\tau$ at $Re_{\rm i} = 617.8125$ does not result in a transition to a laminar flow, although eventually the flow does relaminarize. This result shows that the transition from IPS to laminar flow also appears to have a probabilistic nature and does not correspond to a bifurcation which would have resulted

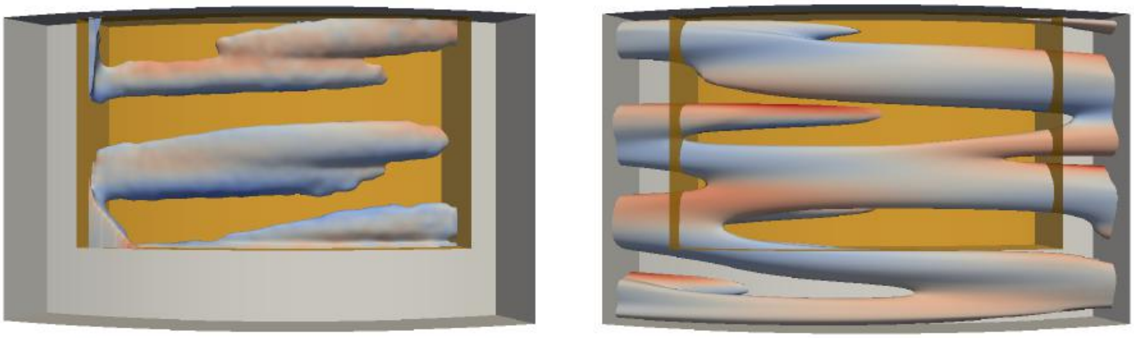
(a) (b)

Figure 4.4: A snapshot of interpenetrating spirals in (a) a tomo PIV experiment and (b) DNS. Each image shows a single isosurface of the perturbation field, $\widetilde{\mathbf{v}}_\theta$, for $Re_\mathrm{i} = 625$ and $Re_\mathrm{o} = -1000$ inside a cylindrical subvolume. The color indicates the corresponding azimuthal velocity component. Red (blue) indicates flow in the same direction as the inner (outer) cylinder rotation. The shaded orange rectangular box represents the region probed by tomo PIV, which spans approximately 10 % of the flow domain volume.

in a sharp transition boundary.

Flow Field Characterization

Flow fields computed numerically also compare well with measurements from laboratory experiments. The stable IPS found in simulations and experiments exhibit a similar spatial structure (Figure 4.4). Moreover, both experiments and simulations show that just above the onset of turbulence, the flow features localized patches of turbulence that co-exist with disordered spiral structures [25] (see Figure 4.4 for an example of the localized turbulent patch in both experiment and numerics). To quantitatively compare the flows in experiment and numerics, we computed the average energy E corresponding to the θ component of the velocity perturbation $\widetilde{\mathbf{v}} = \mathbf{v} - \mathbf{v}^\mathrm{lam}$ over a time interval $T = O(\tau)$ and region Ω in the r, z plane at a fixed azimuthal location where experimental velocity measurements were available. Only the θ-component of velocity was analyzed because v_r and v_z had increased noise due to the frame rates used in the PIV. The region Ω is bounded by the coordinates $r \in [\eta/(1-\eta), 1/(1-\eta)]$ and $z/\Gamma \in [0.254, 0.973]$, where z is measured from the bottom

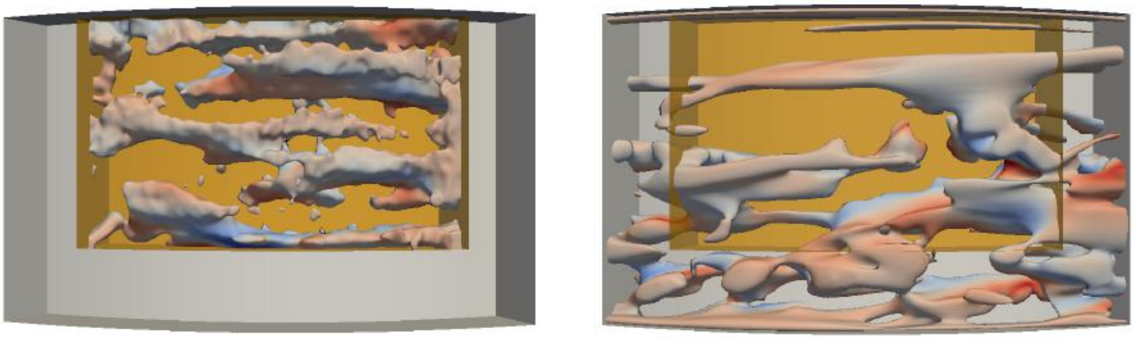
(a) (b)

Figure 4.5: A snapshot of a turbulent flow in experiment (a) and DNS (b). Each image shows a single isosurface of the perturbation field, $\widetilde{\mathbf{v}}_\theta$, for $Re_{\rm i} = 650$ and $Re_{\rm o} = -1000$ inside a cylindrical subvolume. The color indicates the corresponding azimuthal velocity component. Red (blue) indicates flow in the same direction as the inner (outer) cylinder rotation. The shaded orange rectangular box represents the region probed by tomo PIV, which spans approximately 10 % of the flow domain volume.

of the flow domain. For the stable states (IPS and turbulence), the average energy was defined according to

$$E = \frac{1}{TA}\int_0^T dt \int_\Omega \widetilde{v}_\theta^2(t)\, dr dz, \tag{4.3}$$

where A is the area of the cross section of Ω.

The information presented above is summarized in Figure 4.6 in the form of a bifurcation diagram. In particular, we find that the energy E serves as a good order parameter that allows one to easily distinguish the qualitatively different flows (laminar flow, IPS, and turbulence) and to determine where transitions between different flows take place. In particular, we find that the average values of E in experiment and numerics are in good quantitative agreement and that E changes smoothly with Re_i for both IPS and turbulent flow over the regions where these flows are stable (indicated by solid black lines). The dashed lines indicate the trends when these flow states become unstable and are merely extrapolations of the solid curves.

The figure also shows how the energy of the critical disturbance that lies on the boundary of the basin of attraction of the stable laminar flow varies with $Re_{\rm i}$. The dotted

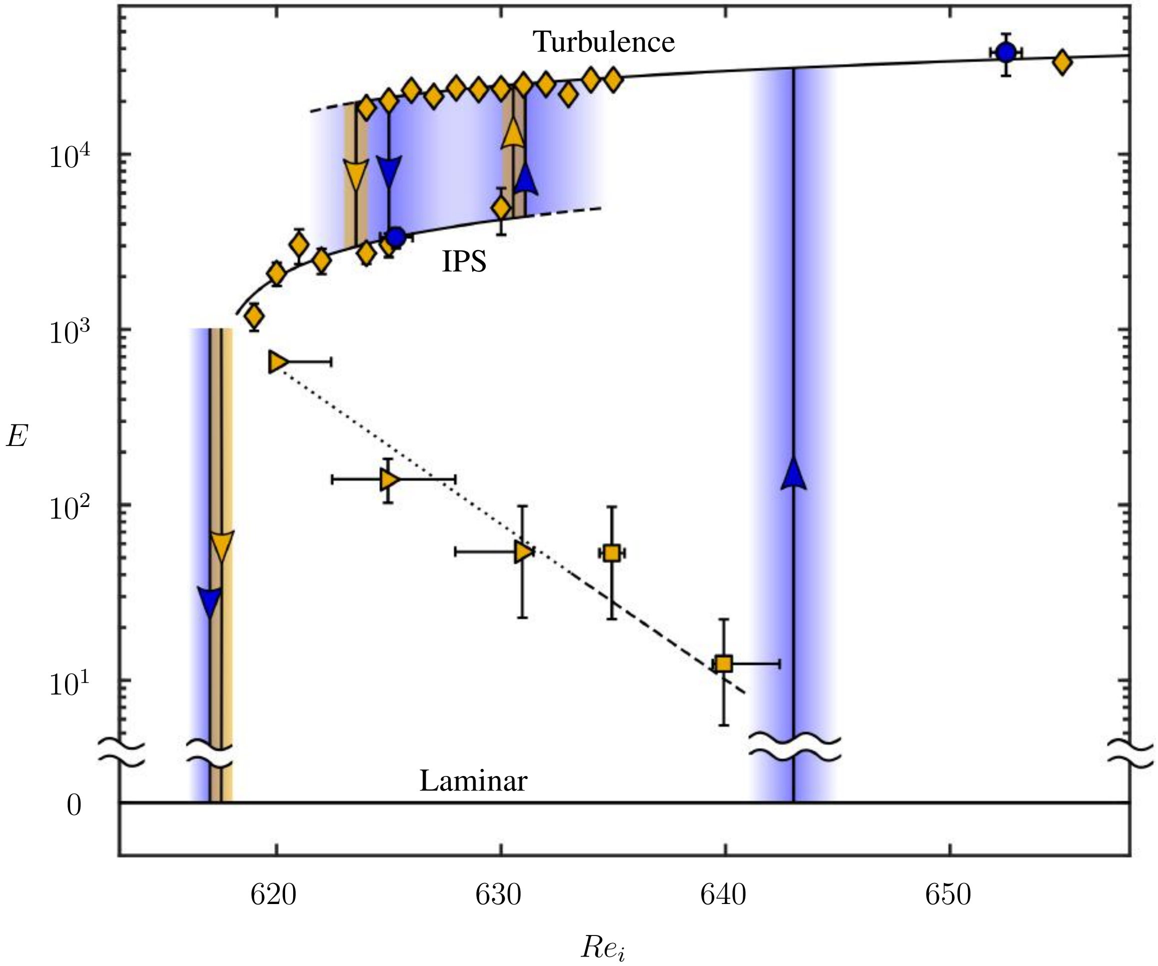

Figure 4.6: Transition map for the three flow states: laminar, IPS, and turbulence. Numerically computed values of E for stable IPS and turbulence at various Re_i are plotted as ◆ while the values calculated from experimental measurements are plotted as ●. The gold and blue arrows indicate the values of Re_i at which transitions occur in simulation and experiment respectively. The shading around the arrows corresponds to the uncertainty in the transitional Re_i value. The ▶ and ■ represent the E value associated with the critical magnitude of the finite amplitude perturbation considered here, which corresponds to $\alpha = \alpha_c$, necessary to initiate transition from laminar flow to IPS and turbulence, respectively. All curves are to guide the eye only.

(dashed) line denotes the transition to IPS (turbulence). To compute this boundary, we performed an average over the azimuthal variable rather than time in (Equation 4.3), where $\widetilde{\mathbf{v}} = \alpha(\mathbf{v}^{\mathrm{IPS}} - \mathbf{v}^{\mathrm{lam}})$ according to (Equation 4.2) and $\alpha = \alpha_c$. Although the specific values of E which define this boundary, just like α_c, depend on the spatial structure of the perturbation $\widetilde{\mathbf{v}}$, the shape of the boundary suggests that it is related to an unstable edge state (or states) connecting the laminar state and IPS, as discussed previously.

In the course of this work we learned that the transition to turbulence in a TCF with $\Gamma = 5.26$ is direct from laminar to turbulent, unlike the transition observed in large aspect ratio systems. This transition is mediated by an intermediate flow state that believed to live on the boundary between turbulence and laminar. The direct nature of this transition resembles the transitions to turbulence observed in wall bounded, shear flows which makes the small Γ TCF an interesting system to study the dynamical systems description of turbulence.

4.3 Discussion

Two distinct instabilities at play in counter-rotating TCF form the basis for a qualitative physical picture of turbulent transition. In the limiting case where Re_{o} approaches zero (the outer cylinder is at rest), the laminar flow is subject to centrifugal instability when Re_{i} is sufficiently large. By contrast, in the limiting case where Re_{i} approaches zero (the inner cylinder is at rest), the flow is centrifugally stable for all values of Re_{o}, but is subject to shear instability for Re_{o} sufficiently large. Under counter-rotation, both instability mechanisms can, roughly speaking, be thought of as operative in distinct spatial regions, separated by a “nodal surface” where the azimuthal velocity component is zero. On the side of the nodal surface nearer the inner cylinder, the azimuthal velocity component is decreasing with increasing radial distance from the inner cylinder, thereby, providing a necessary condition for centrifugal instability in this (inner) flow region. On the side of the nodal surface nearer the outer cylinder, centrifugal instability is ruled out since the azimuthal velocity component is increasing with increasing radial distance from the inner cylinder; however, shear flow instabilities remain as a possibility in this (outer) flow region.

Prior work in large-aspect-ratio counter-rotating TCF has described a scenario in which the interplay between the inner and outer flow regions leads to turbulent transition. When Re_o is fixed and sufficiently large in magnitude and Re_i is increased quasi-statically, the primary instability of the laminar flow leads to the formation of stable spiral flows [191, 50, 192, 193], which are mainly confined to the centrifugally-unstable inner region and qualitatively similar to IPS described in the present paper. Simulations with periodic axial boundary conditions [194] showed that, as Re_i is increased beyond the primary instability, the spiral flow in the inner region increasingly disturbs the centrifugally-stable outer region. Coughlin & Marcus found that, beyond a certain Re_i, the disturbance amplitude becomes strong enough to trigger a shear instability in the outer layer leading to turbulence. This transition scenario is in qualitative agreement with experimental observation in TCF with moderate-to-large aspect ratios ($17 \leq \Gamma \leq 46$) [71].

Our experimental results suggest the interactions between inner and outer flow regions also play a central role in transition in small-aspect-ratio TCF, with the important difference that transition from laminar flow leads directly to turbulence facilitated by the temporary appearance of IPS. The laminar state with Re_o fixed exhibits a subcritical rather than a supercritical instability as Re_i increased quasi-statically. Consequently, as Re_i increases, the laminar flow undergoes a finite amplitude instability leading to growth of a spiral flow mostly confined to the inner region (cf. Figure 4.7(a)). However, unlike the large-aspect-ratio case, the emerging spiral states are transient, with the flow in the inner region generating disturbances of sufficient amplitude to trigger shear instability in the outer region leading to turbulence (cf. Figure 4.7(b)). Stable IPS do exist in our system at lower Re_i, but are disconnected from the axisymmetric laminar solution. The transition from stable IPS to turbulence appears similar to the large-aspect-ratio case.

This transition, as well as the reverse transition from turbulence to stable IPS are similar from a dynamical systems standpoint. The results shown in Figure 4.3(a) for the decay from

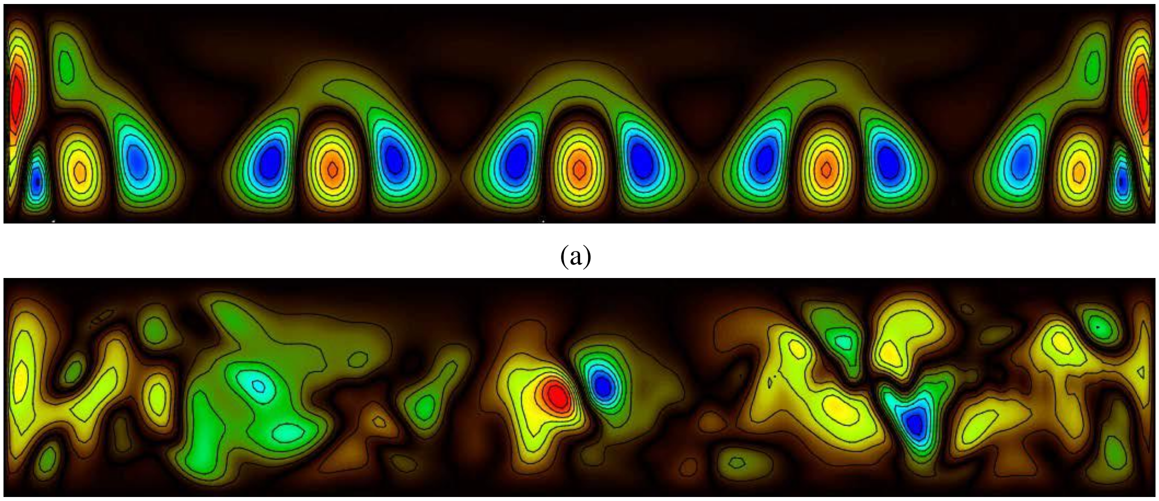

(a)

(b)

Figure 4.7: Typical snapshots of the radial velocity in the constant θ plane for (a) IPS and (b) turbulence in the numerical simulation at $Re_i = 637$ and $Re_o = -1000$. The r direction is vertical and z is horizontal, with the inner cylinder at the bottom. Red (blue) indicates positive (negative) values of v_r.

turbulence is reminiscent of earlier observations of transitions from turbulence in pipe flows [195, 186, 196] and in large-aspect-ratio TCF driven solely by outer cylinder rotation [60]. In all these cases, the exponential decay from turbulence is suggestive of a memoryless process in which, from a state space viewpoint, the transient character of turbulence is captured by a finite-time escape from a chaotic repeller to a qualitatively different solution. Interestingly, in all previous work, once the turbulent transients had disappeared, the flow relaminarized; by contrast, our results demonstrate, for the first time, that turbulence gives way to another chaotic state (IPS). Moreover, Figure 4.3(b) suggests the transition from IPS to turbulence exhibits a similar character, so that for sufficiently large Re_i, IPS are described by a chaotic repeller and the flow transitions to a different chaotic state (turbulence). In this regard, the origin of the IPS-to-turbulent transition observed here is quite different from the linear secondary instability mechanism proposed earlier [194]. The change of the nature of the chaotic set underlying IPS from an attractor at lower Re_i to a repeller at higher Re_i also explains the transient appearance of IPS during the transition from laminar to turbulent flow.

Prior work has demonstrated the chaotic behavior of IPS arises from competition between spiral modes of different wavenumbers and helicities [50, 71, 194]. Our observations of IPS were made in a TCF apparatus with an aspect ratio substantially smaller than that employed in earlier studies of IPS; thus, axial confinement effects in our work hinders clear identification of distinct spiral modes at play in IPS. Nevertheless, we speculate that chaos in IPS observed here originates from qualitatively similar mode interactions as that found in larger aspect ratio studies.

Our experimental and numerical results indicate that, for suitable parameter values, Taylor-Couette flow can exhibit some key characteristics commonly observed in the transition to turbulence in other shear flows. The transition from laminar flow to turbulence is subcritical, like that observed for flows in channels and boundary layers. In particular, when transition is probed by increasing Re_{i} sufficiently slowly (see subsubsection 4.2.2), structured, non-turbulent flows (transient interpenetrating sprials) mediate the transition to turbulence in Taylor-Couette flow in a manner that is analogous to the role of Tollmein-Schlicting (TS) waves in the transition to turbulence in channels and boundary layers in low-noise environments. However, there are also significant differences between Taylor-Couette flow and other canonical shear flows: the physical instability mechanism of IPS (centrifugal instability) differs from the mechanisms for TS waves; TCF transition does not feature a linear growth regime like that found for TS waves in channel and boundary layer transition; stable, nonlinearly-saturated TS waves are never observed in channels/boundary layers, unlike the stable IPS observed in TCF.

Subcritical laminar-turbulent transition is most commonly studied in open flows. However, closed flows such as TCF, which display highly reproducible transitions and close correspondence between numerics and experiments, offer opportunities to explore in much greater detail behaviors that may show up in a variety of shear flows, open or closed. One such opportunity for future study emerging from recent theoretical and experimental work suggests that the dynamics of turbulent flows are guided by particular unstable solutions to the Navier-Stokes equation [197, 198]. This work suggests that selected solutions with simple temporal behavior (e.g., equilibria, limit cycle oscillations) exhibit spatial structures that are strikingly similar to well-known patterns (coherent structures) that have long been known to play a central role in turbulence; moreover, a suitable selection of such solutions (known as *exact coherent structures*) can be harnessed to capture turbulent flow dynamics and statistics (e.g., average turbulent flow properties). Our results suggest that exact coherent structures with spiral spatial structures could play a role in mediating laminar-turbulent transition in counter-rotating Taylor-Couette flow.

CHAPTER 5

DYNAMICAL SHADOWING OF RELATIVE PERIODIC ORBITS BY TURBULENCE

Both engineered and naturally occurring fluid flows are often turbulent and exhibit rich and complicated dynamics. Yet despite centuries of systematic studies going back to Leonardo da Vinci, numerous open questions remain. Statistical theories brought some success in understanding energy and momentum transport in turbulent flows [3, 4], yet quantitative predictions, even for simple properties such as the pressure drop for turbulent pipe flow, remain elusive and require the use of empirical relations [5]. Statistical approaches tend to assume isotropic and/or highly symmetric flows, neglecting the spatial and temporal structure of turbulence. In particular, one of the key unexplained mysteries is the role of recurring, recognizable patterns, known as coherent structures [9]. Coherent structures can provide a better understanding of turbulence [22], even describing physical mechanisms [16] not captured by statistical distributions. While previous studies have primarily focused on the spatial aspects of coherent structures, coherent structures can be used as building blocks of the temporal behavior of turbulence as well. The attempts to build deterministic models describing the evolution of coherent structures based on various modal decompositions go back many decades [199].

A description of turbulence that incorporates coherent structures requires them to be connected to the governing equations. Development of advanced numerical methods such as Newton-Krylov solvers [200] have enabled the computation of unstable, recurrent solutions of the Navier-Stokes equation. Some of these solutions were found to have spatiotemporal properties similar to the observed coherent structures leading to the conjecture that coherent structures appear when turbulent flow transiently approaches these solutions. Consequently, such unstable solutions became known as exact coherent structures (ECSs).

ECSs provide a direct link between the governing equations and the short-lived patterns frequently observed in turbulent flows. They also concrete the qualitative picture of turbulence proposed in the 1940s by Eberhard Hopf [23]. Inspired by the work of Poincaré on celestial mechanics and chaos [24], Hopf's picture represents turbulence as co-evolving with (shadowing), one after another, a repertoire of unstable solutions. Shadowing implies that turbulent flow has spatial *and* temporal structure mimicking that of (possibly more than one) unstable recurrent solutions to the governing equations.

Most of the prior work exploring the role of exact coherent structures in turbulence focused on traveling waves (TW) in transitional flows [18], although TWs have been found in flows as high as $Re = O(10^6)$ [201]. Traveling waves are equilibria in a co-moving reference frame and represent the simplest type of dynamics in systems with continuous spatial symmetries. There is experimental evidence of the role of TWs in the transition from laminar flow to turbulence [197, 202, 203]. TWs were even found to be visited by turbulent flow in numerical simulations of channel flow [204] and pipe flow [205, 206]. However, TWs are too simple to describe the rich temporal dynamics of fluid turbulence. Instead, ECSs that exhibit nontrivial temporal behavior [207, 208] are better suited for this purpose. In particular, RPOs, which are periodic orbits in a co-moving reference frame, are thought to play a key role [45]. Although previous studies found the flow to instantaneously resemble RPOs in numerical simulation of transitional turbulence [45], it was only recently shown that ECSs describe the temporal evolution as well [209]. To date, these findings have not been validated experimentally. In this chapter, the first experimental evidence that unstable, recurrent solutions (i.e. ECSs) play a substantial and persistent role in characterizing the time-evolution of experimentally observable turbulence in three spatial dimensions is presented.

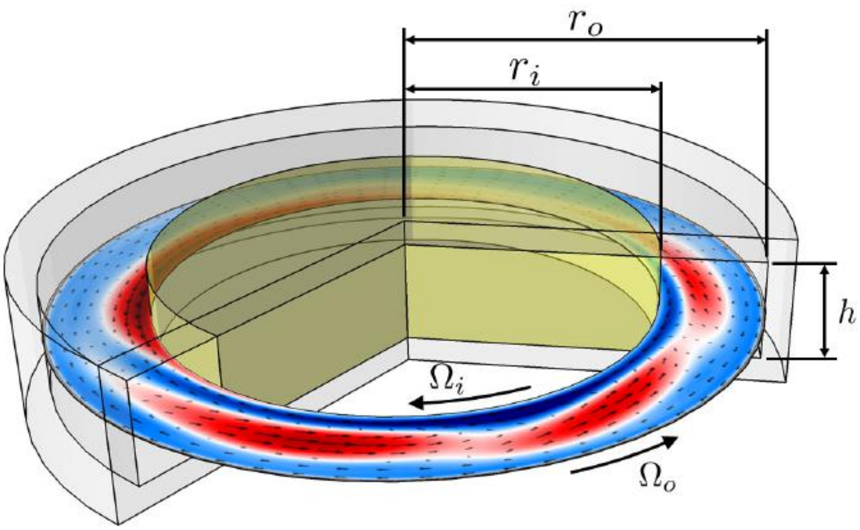

Figure 5.1: Turbulence is visualized in a laboratory flow between concentric, independently-rotating cylinders with radii r_i, r_o and corresponding angular velocities Ω_i, Ω_o. Fluid is confined between the cylinders and bounded axially by end caps co-rotating with the outer cylinder. The red-white-blue colors indicate the fluid's deviation from the mean azimuthal velocity component at a fixed axial location equidistant ($h/2$) from the axial end caps.

5.1 Turbulence in small Γ TCF

To convincingly verify Hopf's picture of turbulence, it is necessary to compute a collection of ECSs under conditions that fully match those encountered experimentally. This is most conveniently done for a closed flow, where the boundary conditions in the flow direction are naturally periodic. For this reason, the present study focuses on TCF between two concentric, independently rotating cylinders. The present study was carried out in a system with $\Gamma = 1$, as shown in Figure 5.1.

TCF is a canonical flow that has been used to study a wide variety of flow behaviors, including pattern formation [58, 50], transition to turbulence [52, 53, 54, 60, 25], and turbulence itself [55, 56, 57]. The bulk of the previous work was performed in systems with large Γ. In the work presented here, we restrict Γ to be small to allow for direct comparisons between numerics and experiment across the full flow domain. Specifically, we focus on flows driven by counter-rotating cylinders ($Re_i = 500$, $Re_o = -200$) in a wide-gap ($\eta = 0.71$), small-aspect-ratio ($\Gamma = 1$) geometry. In the small-aspect-ratio regime ($\Gamma \approx 1$) of TCF, there have been several studies with stationary outer cylinder and rotating inner cylinder [61, 62, 63, 64, 65, 66, 67, 68, 69]; however, only one study examines the co- and counter-rotating scenarios [70], and none investigate turbulence.

As Γ decreases, the end cap effects play a more substantial role than they do at large Γ. In particular, the top and bottom end caps result in a redistribution of angular momentum, which causes the transition away from the laminar base flow to occur at larger values of Re_i [71]. However, the decrease in Γ does not undermine the three-dimensional nature of the spatio-temporally chaotic flow observed at Reynolds numbers considered in this study, which still exhibits structure over a range of scales in each spatial dimension.

An experimental realization of TCF was constructed with transparent walls, giving optical access to the entire domain of the flow. For visualization, the flow was seeded with neutrally buoyant, fluorescent tracer particles and the plane at $z = h/2$ was illuminated. For details regarding the experimental design, construction, and procedure, see Chapter 3. Despite having nontrivial structure in the axial direction, shadowing can be characterized sufficiently well by considering the motion in a radial-azimuthal plane at a fixed height along the axis (see subsection 5.2.1 for details). The flow was imaged with a camera whose line of sight lies along the cylinders' axes, and in-plane components of velocity were determined using particle image velocimetry. Direct Numerical Simulations (DNS) in the entire flow domain were performed using a pseudospectral solver [181] with boundary conditions exactly matching experiment [210]. This correspondence enables a quantitative comparison of numerically computed ECS with experiment.

5.2 A demonstration of shadowing

5.2.1 A quantitative signature of shadowing

Often, state space distance is used as a measure of similarity of two flows [211, 45, 44]. If two flows resemble each other, their l^2-norm based distance, $D_1(t)$, should be small. However, just having a small distance between the two flows does not imply they are evolving similarly. Consider two examples from Kuramoto-Sivashinsky (KS), which is a nonlinear model of how a laminar flame front evolves [212, 213]. In general, KS is a vector equation, but let's consider the one-dimensional version of it,

$$u_t + u_{xx} + u_{xxxx} + \frac{1}{2}u_x^2 = 0, \tag{5.1}$$

where the subscripts imply partial derivatives with respect to that variable. To analyze the KS system in one-dimension, allow the spatial domain to be periodic. In this scenario, there is a continuous symmetry in the spatial dimension, which implies that the relevant class of ECSs will be RPOs.

Figure 5.2 presents two examples of when a chaotic trajectory in KS has a small distance with an RPO. Both examples have comparably small distance values between turbulence and the RPO, but as can be seen in panel (b), only one of the examples has dynamical similarity. Therefore, if an RPO is to be considered dynamically relevant to turbulence, a more sophisticated metric than the simple closest distance is needed.

In order to establish the dynamical relevance of an RPO in turbulence, the flows representing both must have similar temporal evolution and spatial orientation. To quantify how closely the RPO is being shadowed, we define two distance metrics

$$D_\phi(t,\tau) = \min_{\phi} \|\mathbf{u}(t) - \mathbf{u}_i(\phi,\tau)\|_2 \tag{5.2}$$

and

$$D_\tau(t,\phi) = \min_{\tau} \|\mathbf{u}(t) - \mathbf{u}_i(\phi,\tau)\|_2, \tag{5.3}$$

whose minima determine the evolution of the coordinates τ and ϕ parameterizing the RPO. An example of a turbulent flow in direct numerical simulations (DNS) shadowing an RPO is shown in Figure 5.3. In this example, for the range of t where turbulence is shadowing

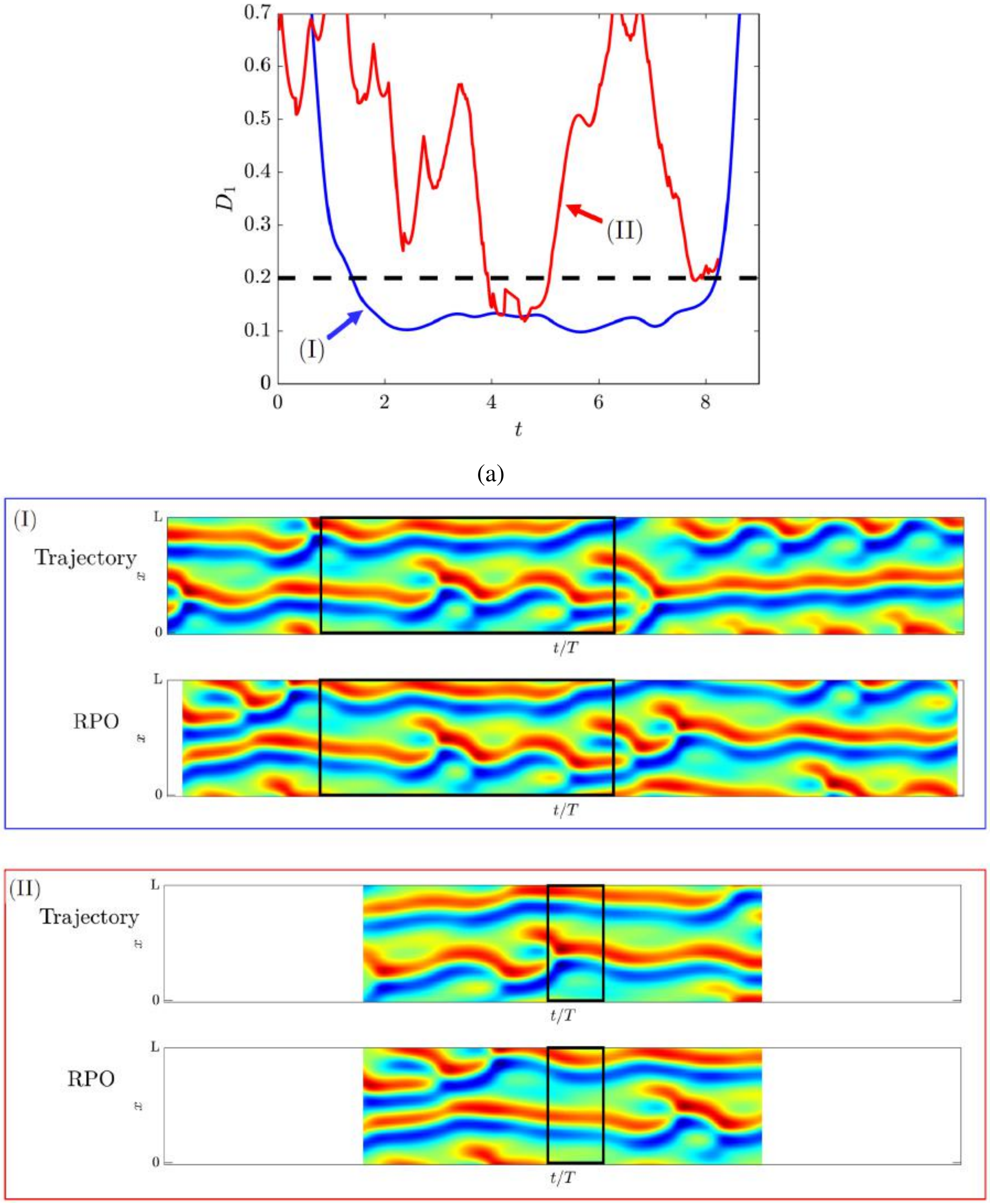

(a)

(b)

Figure 5.2: Two examples from Kuramoto-Sivashinsky demonstrating that state space distance alone is not sufficient for identifying shadowing. Panel (a) shows two events of comparably small state space distance: (I) and (II). In panel (b), both examples are plotted with the chaotic trajectory on top and the RPO being shadowed below. The interval of time when the distance is below the threshold indicated in panel (a) is outlined by a black box. Note that for example (I), the interval below the distance threshold is a good example of shadowing while the comparably low distance of example (II) is not an example of shadowing.

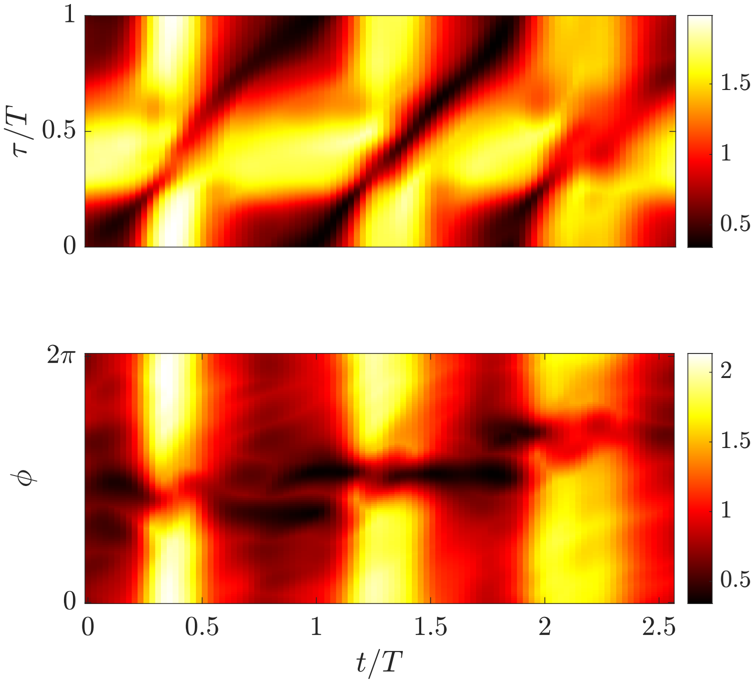

Figure 5.3: A shadowing event for RPO$_1$ in DNS. The distance metrics D_ϕ (above) and D_τ (below) are shown over a time interval including the shadowing event which corresponds to $t/T \in (0.8, 1.8)$.

the RPO, there is a clear minimum in D_ϕ that falls along the diagonal $\tau = t - t_0$ and a staircase pattern of minima in D_τ, implying the flows are not only similar at one time instant, but both flows have the expected similar orientation and temporal evolution for more than one period. The discrete shifts in the minima of D_τ are associated with the rotation of the reference frame by angle Φ_i once per period of the RPO, so that $\mathbf{u}(t)$ is expected to be similar to $\mathbf{u}_i(\phi \pm \Phi_i, \tau)$ for $\tau < 0$ and $\tau > T_i$.

5.2.2 2D-2C PIV is sufficient

Unlike TW detection in previous experimental studies, RPO detection requires a measurement that provides spatial structure along the streamwise direction. TWs have spatial and temporal translations that are equivalent, making it possible to detect them by imaging the flow in a fixed plane transverse to the flow and using Taylor's frozen turbulence hypothesis to reconstruct the spatial variation from the temporal variation. However, RPOs vary

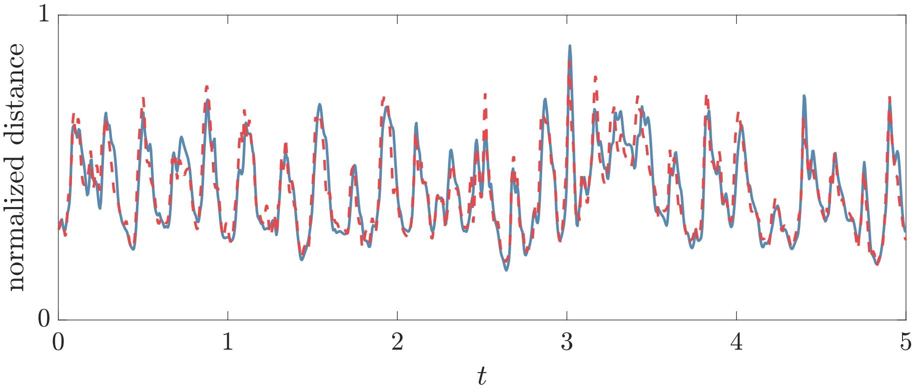

Figure 5.4: The distance $D(t)$ between a turbulent flow in DNS and RPO$_7$, during an arbitrary interval, computed using the full, 3D-3C flow field (solid blue) and the 2D-2C flow field restricted to the midplane $z = 0$ (dashed red). Both signals were normalized to allow direct comparison. These normalized signals differ by less than 1% relative error over the interval $t \in (0, 60)$, indicating that the 2D-2C distance is a good proxy for 3D-3C distances. Here and below, time has been non-dimensionalized using the timescale d^2/ν, for cylinder gap width d and viscosity ν.

independently in space and time, explicitly breaking the Taylor hypothesis. In our system, we find measuring the streamwise (θ) and radial (r) velocity components in a plane at a fixed height along the axis of rotation provides sufficient spatial and temporal information to detect reliable shadowing events involving RPOs. To illustrate this point, the distance $D(t) = \min_\phi D_\tau(t,\phi) = \min_\tau D_\phi(t,\tau)$ between a turbulent flow in DNS and RPO$_7$ is shown in Figure 5.4. In this figure, a clear correlation exists between distances computed over the entire volume and distances computed with only in-plane velocities obtained from the mid-plane.

The ability to robustly identify shadowing events with two-dimensional data sets should not be taken to imply that the flow is nearly two-dimensional. Indeed, the small aspect-ratio Γ implies that end-cap-induced Ekman pumping strongly affects the flow over its entire axial extent. More importantly, as Figure 5.5 illustrates, the fluctuations about the mean flow in all three directions have comparable magnitude over a large range of scales which is typical for three-dimensional turbulent flows. Also, as is typical for turbulent flows, we find the power spectrum to be broadband without any discernible peaks for any of the three velocity components.

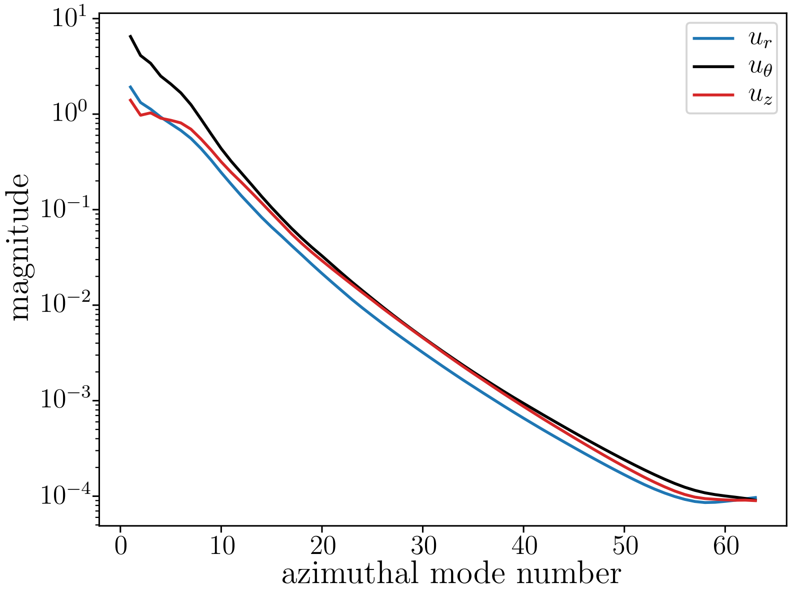

Figure 5.5: Turbulent behavior in all three velocity components is indicated by significant energy in a broad range of azimuthal mode numbers, as illustrated by the time-averaged magnitude of the azimuthal spectral coefficients from numerical simulations at Re_i = 500, Re_o= -200.

5.2.3 Library of Solutions

Taylor-Couette flow has inherent symmetry with respect to continuous rotations about the z-axis, R_ϕ,

$$R_\phi \mathbf{u}(r, \theta, z) = \mathbf{u}(r, \theta - \phi, z), \tag{5.4}$$

and discrete reflections, K_z,

$$K_z[u_r, u_\theta, u_z](r, \theta, z) = [u_r, u_\theta, -u_z](r, \theta, -z), \tag{5.5}$$

about the z-axis. This implies that the solutions relevant to turbulence are relative solutions, such as RPOs or traveling waves, and pre-periodic orbits. A turbulent trajectory $\mathbf{u}(t)$ was computed for 60 non-dimensional time units (equivalent to $300\overline{T_i}$) where time is non-dimensionalized using the radial momentum diffusion timescale, $d^2/\nu \approx 267$ sec-

Table 5.1: Properties of RPOs found in TCF for $\Gamma = 1$, $\eta = 0.71$, $\text{Re}_i = 500$ and $\text{Re}_o = -200$: the temporal period T and shift ϕ. The dimension of the unstable manifold of each solution, N^u is also shown, as well as the escape time, γ^{-1}. Both the period and escape rate have been non-dimensionalized using the timescale $d^2/\nu \approx 267$ seconds, for cylinder gap width d and viscosity ν.

	T	Φ	N^u	γ^{-1}
RPO_1	0.195	1.040	7	0.0246
RPO_2	0.177	0.855	5	0.0166
RPO_3	0.234	0.447	7	0.0260
RPO_4	0.199	0.198	6	0.0227
RPO_5	0.421	0.442	5	0.0295
RPO_6	0.419	0.424	6	0.0291
RPO_7	0.164	0.481	6	0.0249
RPO_8	0.215	5.799	6	0.0464

onds. We find that the chaotic set breaks the z-reflection symmetry. That is, there are two z-asymmetric chaotic sets, one the reflected copy of the other, which are observed to be dynamically disconnected. Pre-periodic orbits, which would represent orbits lying in both sets, are therefore unlikely to be relevant to turbulent motion. Because of this, we focus on relative solutions exclusively.

Relative solutions were found using an in-house Newton-GMRES solver [210] that leverages a hookstep algorithm [200]. Since Newton's method is not globally convergent, sufficiently good initial guesses had to be supplied to this solver. To accomplish this we computed a turbulent trajectory, $\mathbf{u}(t)$, and analyzed the recurrence function,

$$G(t) = \min_{\tau,\phi} D_{\text{self}}(\phi, \tau, t). \tag{5.6}$$

Deep minima of Equation 5.6 correspond to moments in which the turbulent trajectory is almost periodic or stationary in the co-moving frame. The flow field during these deep minima, as well as their corresponding τ and ϕ values, are good initial conditions for the solver. These initial conditions are fed into the solver and added to our library of solutions if the relative residual

$$\varepsilon = \frac{\|\mathbf{u}(T) - R_\Phi \mathbf{u}(0)\|_2}{\|\mathbf{u}(0)\|_2}, \tag{5.7}$$

becomes sufficiently small ($\varepsilon < 10^{-11}$). T and Φ represent the period and azimuthal shift of converged solutions. Eight distinct solutions were converged for this parameter regime; their properties are listed in Table 5.1.

The symmetry-reduced Euclidean distance

$$D_i(\mathbf{u}(t)) = \min_{\phi,\tau} \|\mathbf{u}(t) - R_\phi \mathbf{u}_i(\tau)\|_2 \tag{5.8}$$

between each of these solutions and the turbulent flow $\mathbf{u}(t)$ is shown in Figure 5.6. The distance was normalized by the radius of the chaotic set

$$\Sigma = \langle\, \|\mathbf{u}(t) - \langle \mathbf{u}(t)\rangle_t\|_2 \,\rangle_t, \tag{5.9}$$

where $\langle \,\cdot\, \rangle_t$ denotes a temporal mean. Low (compared with unity) values of D_i/Σ indicate instances where turbulence approaches RPO $\mathbf{u}_i$.

5.2.4 Examples of shadowing

Rotational symmetry of the TCF implies that, just like for a pipe or channel flow, most ECSs are expected to take the form of either RPOs or TWs [45]. Both types of ECSs satisfy the condition

$$\mathbf{u}(r, \theta - \Phi, z, t + T) = \mathbf{u}(r, \theta, z, t). \tag{5.10}$$

For RPOs, T is the period of the solution and Φ is the angle by which the solution drifts in the azimuthal direction over one period. The constant angular speed of the co-moving frame is then $\Omega = \Phi/T$. For TW's, Equation 5.10 is satisfied for any Φ and T whose ratio

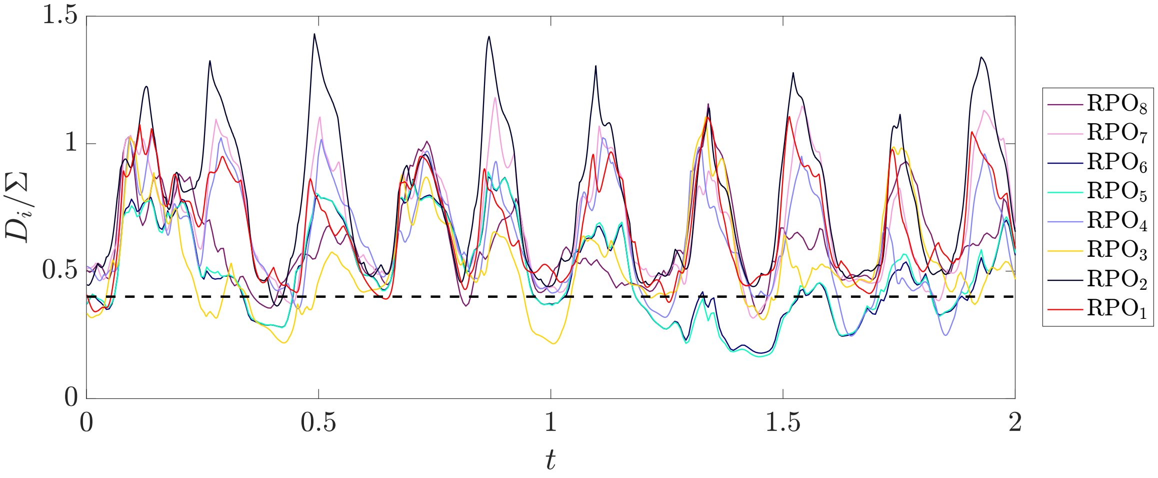

Figure 5.6: The distance between turbulent trajectory and the eight RPOs in DNS, computed using the 3D-3C Euclidean norm. Here, D_i is the distance to solution $\mathbf{u}_i$ and Σ is the radius of the chaotic set. The threshold $D_i/\Sigma = 0.4$ below which two flow states are considered close is designated with a dashed black line. While the full data set spans $t \in [0, 60]$, only a portion of that interval is shown here, to better illustrate the behavior of the distances, D_i.

Ω is the drift speed of the solution.

We focused on computing RPOs by analyzing a long, unconstrained turbulent flow obtained through DNS. Nearly recurrent segments of the simulated turbulent trajectory were found by examining minima of the residual,

$$D_{\text{self}}(\theta', t', t) = \|\mathbf{u}(r, \theta - \theta', z, t + t') - \mathbf{u}(r, \theta, z, t)\|_2, \tag{5.11}$$

where $\|\mathbf{u}\|_2^2 = \int_V \mathbf{u} \cdot \mathbf{u}\, dV$. These segments were then used as initial conditions for a Newton-Krylov solver which converged them to be exactly recurring, i.e., solutions to Equation 5.10. This search identified eight distinct RPOs, each labeled with index $i = 1, \ldots, 8$.

In general, the set of flow states corresponding to an RPO is a two-torus, S_i, in the infinite-dimensional space of flow states (see Figure 5.7(a)). In the fixed laboratory frame, trajectories lying on S_i are quasi-periodic. Any point on the i-th RPO (light blue two-torus in Figure 5.7(b)) may be written as $\mathbf{u}_i(\phi, \tau)$, for some ϕ and τ. Both coordinates are cyclic, with ϕ running from 0 to 2π and τ ranging from 0 to T_i (the solution's period). To

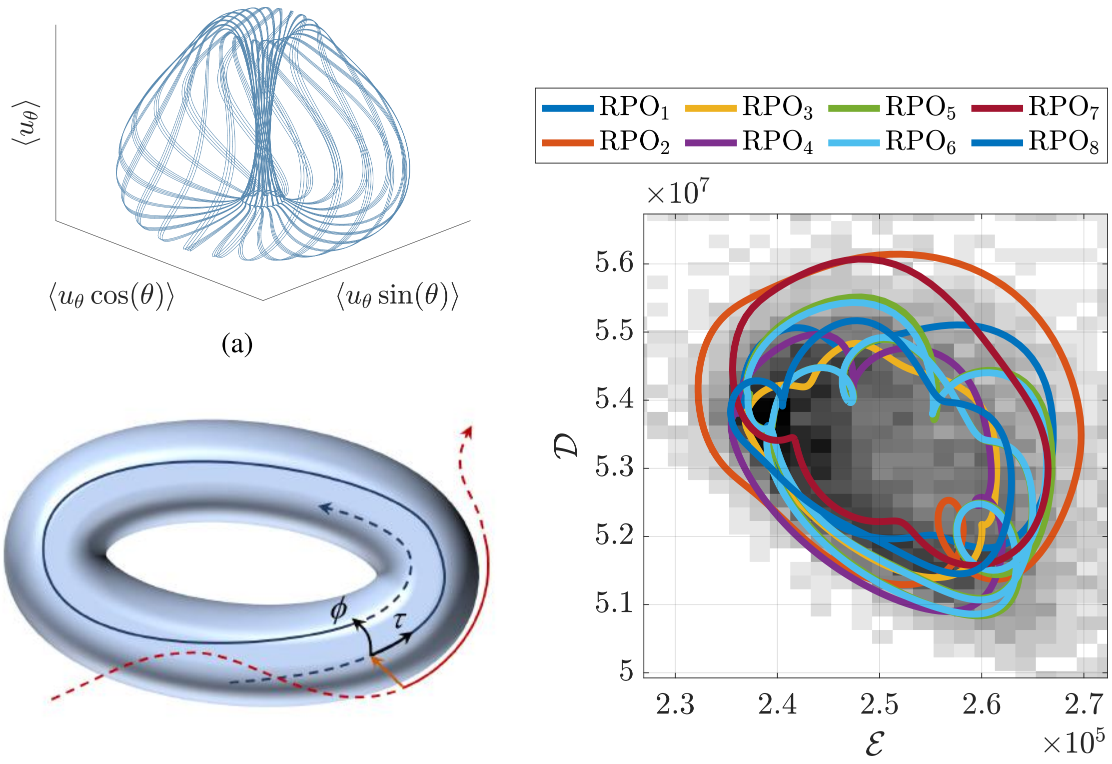

(a)

(b)

(c)

Figure 5.7: Low-dimensional projections suggest that RPOs, i.e. solutions to the governing equations that recur indefinitely in time, are relevant to turbulence. (a) To demonstrate that RPOs are truly two-tori when rotational symmetry is not reduced, RPO_2 is plotted over 80 periods using the coordinates shown, where u_θ represents the azimuthal component of the flow velocity and $\langle \cdot \rangle$ indicates a spatial average. Thus, $\langle u_\theta \rangle$ is the mean azimuthal speed, and $\langle u_\theta \sin(\theta)\rangle$ ($\langle u_\theta \cos(\theta)\rangle$) is the imaginary (real) component of the leading spectral mode. (b) Cartoon depicting how a portion of a turbulent trajectory (solid red curve) shadows, i.e., follows, an RPO (light blue surface) for a period of time. Shown in dark blue is the trajectory belonging to the RPO, which is most similar to the turbulent trajectory. The orange arrow relates a point on the turbulent trajectory to the point closest to it on the torus. (c) Using energy $\mathcal{E}$ and energy dissipation rate $\mathcal{D}$ of the flow as projection coordinates, eight RPOs are represented by closed trajectories (shown in color). RPOs appear as closed curves in this projection because both coordinates are rotationally invariant. The chaotic behavior of turbulence is indicated by the distribution (shown in grey) of visits to particular regions of the projection (darker regions have higher likelihood of visitation).

visualize the relationship between the computed ECSs and turbulent flow, we plotted in Figure 5.7(c) each RPO, $\mathbf{u}_i$, using a low-dimensional projection of the state space spanned by the energy $\mathcal{E} = \|\mathbf{u}\|_2^2$ and the rate of energy dissipation $\mathcal{D} = \|\nabla \times \mathbf{u}\|_2^2$. Since both $\mathcal{E}$ and $\mathcal{D}$ are invariant with respect to rotation, every RPO is represented by a closed curve in this particular projection. Indeed, as we mentioned previously, each RPO becomes a temporally-periodic solution in the co-rotating reference frame.

A long turbulent trajectory computed using DNS is shown in Figure 5.7(c) as a histogram, with the gray scale intensity representing the likelihood of visiting different regions of state space. In this low-dimensional projection, we find that the computed RPOs lie in the regions of state space frequently visited by turbulence. Although this fact is consistent with Hopf's picture of turbulence, it does not by itself demonstrate that turbulent flows evolve similarly to RPOs. If RPOs play an important dynamical role, turbulence will not only approach each RPO, but shadow it, i.e., the corresponding flows will co-evolve in a similar manner for an interval of time before diverging.

The expected duration of shadowing intervals depends on the stability properties of individual RPOs. The more unstable an RPO is compared to its peers, the less frequently its neighborhood is visited by turbulent flow. Moreover, the more unstable a solution is, the shorter the shadowing intervals are. Stability is characterized by the escape rate $\gamma_i = \sum_k \mathrm{Re}(\lambda_{i,k})$, where $\lambda_{i,k}$ are the unstable Floquet exponents of RPO$_i$. The inverse of the escape rate then gives the characteristic duration of shadowing intervals. The typical value in our system, $\gamma^{-1} \sim 0.027$, is much shorter than the typical period of an RPO (see Table 5.1), so turbulence is expected to shadow short segments of an RPO before leaving its neighborhood, as illustrated in Figure 5.7(c).

We quantify shadowing of RPO$_i$ by projecting turbulent flow $\mathbf{u}$ onto the coordinate system associated with the corresponding torus S_i. We define $\mathbf{u}_i(\phi(t), \tau(t))$ to be the point on S_i closest to a snapshot $\mathbf{u}(t)$ of turbulent flow at time t, such that

$$\{\phi(t), \tau(t)\} = \arg\min_{\tau', \phi'} \|\mathbf{u}(t) - \mathbf{u}_i(\phi', \tau')\|_2. \tag{5.12}$$

For any initial condition on S_i (e.g., any flow field described by the RPO), we will have $\phi(t) = \phi_0$ and $\tau(t) = t + \tau_0$ with some constant ϕ_0 and τ_0. For any trajectory passing close to S_i, we expect the same relations to be satisfied approximately. Hence, we detect shadowing by searching for intervals where deviations from these two relations are small (specifics can be found in the Materials and Methods "Shadowing Criteria" section below).

Shadowing events identified using these criteria are summarized in Figure 5.8 for a numerically computed turbulent trajectory over an interval equal to about 300 times the mean RPO period; this interval corresponds to about 270 minutes in experiment. We find, in validation of Hopf's picture, that turbulence visits the neighborhoods of all eight RPOs, with each neighborhood visited multiple times. In fact, we observe that turbulence occasionally shadows multiple solutions simultaneously, as indicated by vertical lines that share some time intervals in Figure 5.8. This behavior can be understood from dynamical systems theory, which indicates the state space occupied by a chaotic attractor is tiled with an infinite hierarchy of periodic solutions of varying periods. If two (or more) periodic solutions are nearly identical, then, when turbulence shadows any portion of one such solution's orbit, shadowing of the other close-by solution(s) will typically occur. This is the situation for RPO_5 and RPO_6 in our system. We speculate that RPO_5 and RPO_6 are born from a nearby (in parameter space) bifurcation, thereby explaining their closeness. When solutions are not particularly close (on average) in state space, simultaneous shadowing can still arise if a portion of their orbits are close and the turbulent flow happens to pass into the state space neighborhood of this close portion of the orbits. We believe this to be the case for the simultaneous shadowing of the known RPOs other than RPO_5 and RPO_6.

Figure 5.9 illustrates experimentally observed shadowing of RPO_1 and RPO_7. For each RPO, this figure compares four equally spaced snapshots of the flow field in the symmetry midplane $z = h/2$ that correspond to the RPO and turbulent flow in the experiment. Turbulent flow in this system is characterized by fluctuations that are relatively weak compared to the axisymmetric mean flow $\langle \mathbf{u} \rangle_{t,\theta}$. Hence, to visualize the fluctuation, we subtracted the mean from all the flow states. Figure 5.9 shows the deviation of the azimuthal flow velocity from its mean. In each observed shadowing event, the turbulent flow's complex spatial and

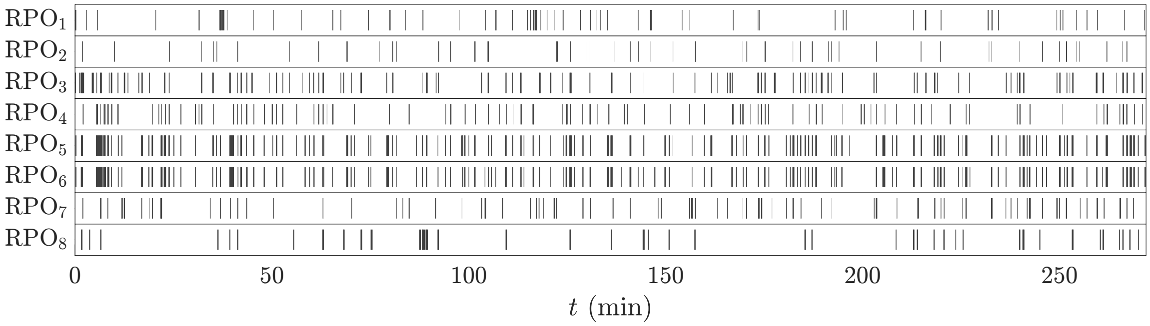

Figure 5.8: Turbulence frequently shadows ECSs. In the graphic, black vertical lines indicate shadowing events – time intervals during which ECSs (RPO$_1$-RPO$_8$) are being tracked by turbulence obtained from a numerical simulation (See Materials and Methods “Shadowing Criteria” section). The duration of each shadowing event shown is at least one escape time γ_i^{-1}, computed from the unstable Floquet exponents of the corresponding ECS.

temporal structure is well characterized by the corresponding RPO.

5.3 Automated shadowing detection

5.3.1 Dynamics in state space

A fluid flow is typically thought of and described as a time-dependant, velocity field; however, this same flow can also be understood as a trajectory in a high-dimensional space, called “state space.” State space can be constructed from the 3D velocity field with any invertable, one-to-one mapping. Regardless of the choice of mapping, at an instant in time, the entire flow field is represented as a single vector. At any instant in time, this vector points to a single location in the state space and, as time evolves, this point traces out a curve. For a turbulent flow, the trajectory of this state vector traces out is a chaotic, complicated curve.

Embedded within the complicated tangle of the turbulent trajectory, there exists special closed trajectories. These closed trajectories are solutions to the governing equations that, unlike turbulence, reccur indefinitely in time (e.g. a fluid flow that exhibits periodic motion in time as it advects down the length of a pipe). Recurrent solutions are thought to be related to coherent structures in the 3D flow field, and, for this reason, are often called

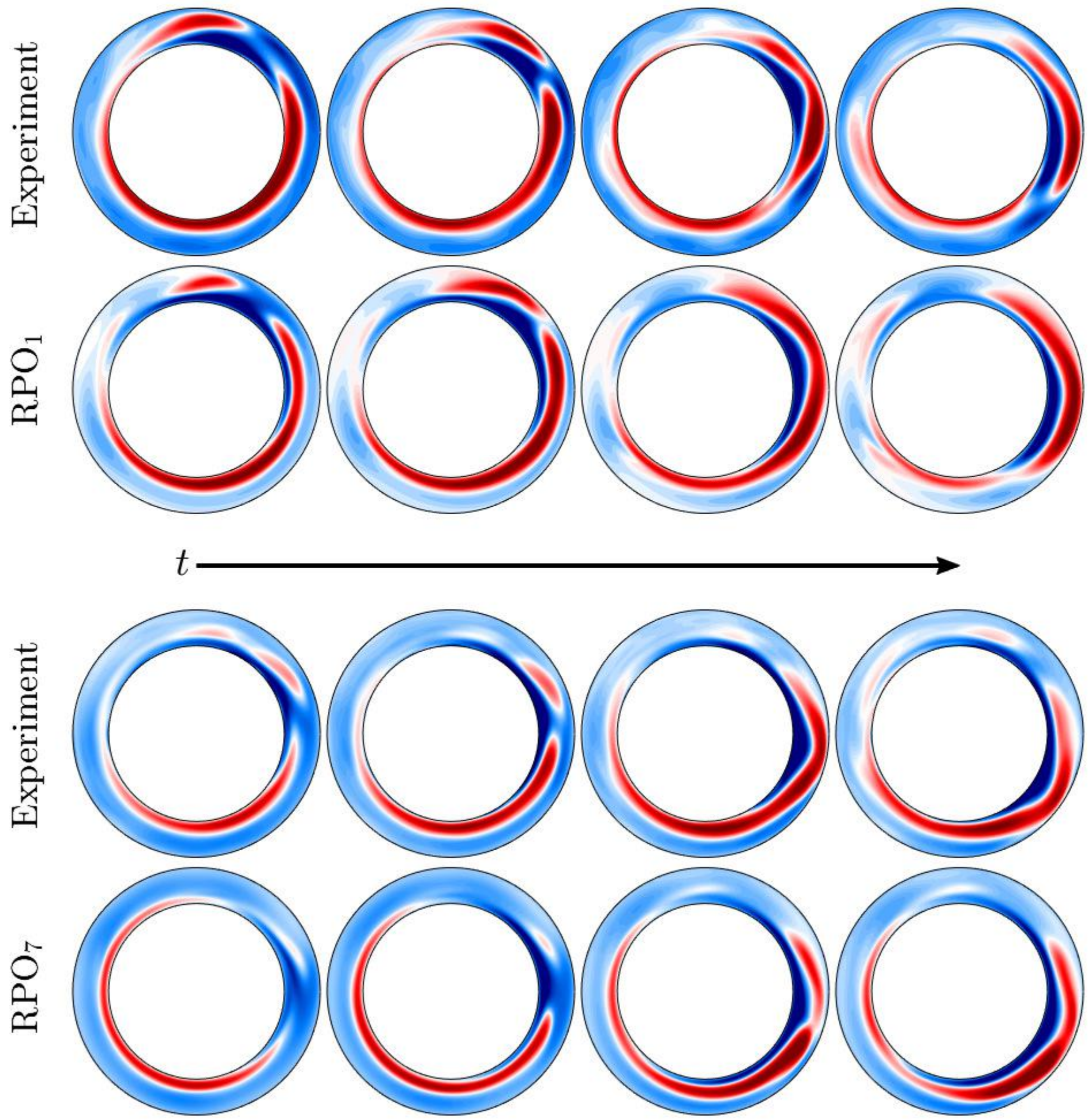

Figure 5.9: Experimental evidence that turbulence and RPOs, i.e., solutions to the governing equations that reccur indefinitely in time, co-evolve when the 'shadowing' criteria are met. Turbulence closely follows RPO$_1$ (top) and, during a different time interval, tracks RPO$_7$ (bottom). In both cases, the color map shows the deviation in the azimuthal component of the velocity u_θ from the mean; moreover, the time interval between successive turbulent snapshots is approximately 3.5 seconds, which may be compared to the period, 52 (44) seconds, and escape time, 6.6 (6.6) seconds, of RPO$_1$ (RPO$_7$). The flow fields for the RPOs were chosen by first finding the optimal azimuthal orientation ϕ_0 and temporal phase τ_0 for the entire shadowing event; subsequently, the RPO was evolved in time while holding the azimuthal orientation fixed (i.e., $\phi(t) = \phi_0$ and $\tau(t) = \tau_0 + t$).

Exact Coherent Structures.

Recurrent solutions are believed to be useful for recovering statistical aspects of the flow [43, 208] and have been proposed the building blocks of state space [45]. These special solutions are located in the same region of state space as the turbulent trajectory and, therefore, capture the intrinsic geometric structure of the chaotic trajectory in state space. With a properly chosen collection of recurrent solutions, the geometry of the full turbulent trajectory can be approximated. Recent work has even suggested that recurrent flows can be used to capture the dynamics of turbulent evolution as well [209, 214].

Representing a turbulent flow as a chaotic trajectory in state space is advantageous for understanding how similar turbulence and recurrent solutions *evolve*. In state space, dynamical similarity is given by the relative shape and proximity of two trajectories. That is, two very close points in state space correspond to two flows that have only a slight difference in the velocity field. Similarly, two trajectories that explore state space along similar shaped paths have two flow fields with similar time evolution. Therefore, if two trajectories are both close and have the same shape, they can be considered dynamically similar.

Identifying intervals of time when a given recurrent solution is dynamically relevant is a first step towards developing a useful framework for understanding the dynamics of turbulence using recurrent solutions as building blocks to coarse grain turbulent state space. Early work focusing on finding recurrent solutions in turbulence either used qualitative comparisons [197] or searching for minima in Euclidean distance in state space [198]. However, just as two flows starting from rest can evolve quite differently, an instantaneously small Euclidean state space distance does not indicate dynamical similarity. To infer dynamical similarity, more must be known about the shape of the trajectories over time.

5.3.2 Signature of shadowing

State space for a turbulent flow is very high-dimensional, and computing the geometric similarity of trajectories in this space is computationally intractable (although possible through methods like persistent topology). To overcome this, a projection is needed [43]. Often, the choice of projections are either along dimensions corresponding to observables calculated from the flow (e.g. energy input and dissipation) or simply ad hoc. If the observables are chosen intelligently, a lot can be understood from a small amount of information. On the other hand, if the observables are chosen poorly, the data can be difficult to interpret, have crucial information obscured, or even be presented in a misleading way.

For instance, consider the use of distance in state space. Often, state space distance is used as a measure of similarity of two flows [211, 45, 44]. If two trajectories in state space are co-evolving, then their Euclidean distance (i.e. l^2-norm based distance), $d(t)$, in state space should be small and remain small as they co-evolve. However, the two trajectories can be the same distance apart from each other, but along many different directions. This means that two flows that have small state space distance, could evolve in different ways. Two fluid flows that are evolving similarly will manifest as two trajectories move along similar shaped paths. Therefore, a better indicator of dynamical similarity is that the distance remain small for some time *and* that the shape of the state space trajectories are similar.

Here, we introduce a projection of state space that makes dynamical similarity of turbulence and a recurrent solution easy to identify. This projection reveals simple, straight features when the two complicated trajectories are evolving similarly. For a fixed point, shadowing is simply indicated by an interval of time where $d(t)$ is small. However, recurrent flows are time-dependant and a small value of $d(t)$ does not necessarily imply that the two flows are evolving similarly. For instance, the turbulent trajectory may simply slow down when in the vicinity of the recurrent solution before racing away, resulting in an extended duration of time with small $d(t)$. If, on the other hand, the turbulent trajectory is tracking along with the recurrent solution, as time, t, along the turbulent trajectory evolves, the distance to the recurrent solution parameterized in time by τ will remain small as both t and τ evolve. Therefore, not only evaluating the state space distance as a function of t, but also parameterizing the distance with time along the recurrent flow (i.e. $d(t,\tau)$) allows for time-dynamics to be elucidated. When turbulence is shadowing a recurrent solution, the minima of $d(t,\tau)$ to fall along $d(t,t)$.

In addition to paramaterizing distance along both time coordinates, in systems with continuous symetry, the dynamics in the symmetry directions also need to be concidered. Since TCF has a continuous symmetry in θ, time-periodic solutions that advect in the azimuthal direction as time evolves are also possible. This class of solutions is known as relative periodic orbits (RPOs). While the azimuthal drift speed, Ω, will depend on the specific recurrent solution, it is always easily computable from the recurrent solution itself. Thus, for a given specific solution's drift speed, the distance metric will have a minimum of $d(t,\tau,\theta)$ along $d(t,t,\Omega t)$, when turbulence shadows a relative periodic orbit. This calculation can be extended to every symmetry of the recurrent solution. In every situation, regardless of the number of symmetries present, shadowing implies a minimum along a line of constant slope in $d(t,\tau,\theta,\dots)$.

To illustrate the use of this analysis, consider the example projections in Figure 5.10. In panel (a), a projection along two Fourier modes of a turbulent trajectory (in red) evolving similarly to a recurrent solution (in blue) is shown. In this projection the dynamical similarity between these two trajectories is difficult to identify. If, instead, the same co-evolution event is plotted as a heat-map of $d(t,\tau)$, there is a clear minimum distance along a diagonal, straight line (see panel (b) of Figure 5.10). When turbulence and a reccurent solution co-evolve in this way it is called "shadowing." When turbulence is shadowing a reccurent solution (i.e. the minimum of $d(t,\tau)$ falls along a straight, diagonal line), the flow fields in 3D space evolve similarly in time (see Figure 5.9).

5.3.3 Shadowing Detection

The utility of finding linear minima of $d(t,\tau,\theta)$ is clear; when linear minima exist, the flow fields evolve similarly. However, finding many examples of linear minima by inspection is

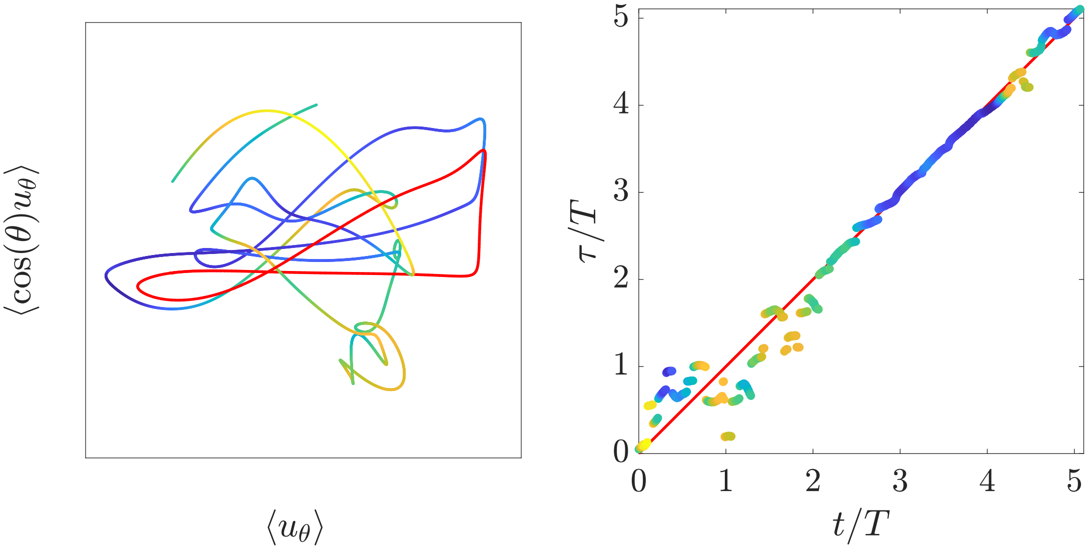

(a)

(b)

Figure 5.10: Illustration of the proposed shadowing projection (b) versus traditional projections (a). In both panels, the recurrent solution is depicted in red. The other curve represent turbulence, color coded by the distance between turbulence and the solution in the full state space. In panel (a), $\langle cos(k\theta)u_\theta\rangle$ represents Fourier modes of the azimuthal velocity field. Fourier modes are computed in the co-moving frame with the recurrent solution, such that it is exactly periodic over one period. In panel (b), the time coordinates of turbulence t, and the recurrent solution τ are used, in units of the solutions period T. In this projection, motion is simple during shadowing (e.g. around $t \in (3, 4)$. Around $t \in (0, 1)$, there is a close pass to the recurrent solution. However, this would not be considered shadowing, since the evolution is not similar, i.e., the line is not sufficiently linear.

laborious. Thus, an automated detection scheme is needed.

For systems with continuous symmetries in their boundaries, a continuum of recurrent flows exist. For each RPO, $\mathbf{u}(\tau, \theta)$, there are symmetry related 'copies', $\mathbf{u}(\tau - \tau_0, \theta - \theta_0)$, that also satisfy the governing equations for $\tau_0 \in [0, T)$ and $\theta_0 \in [0, 2\pi)$. Identifying linear minima in $d(t, \tau)$ for any one of these symmetry related copies would imply turbulence is shadowing the prototypical solution in the family of RPOs, just shifted along the symmetry direction.

In order to identify intervals of time when turbulence is dynamically similar to a given recurrent solution, the average state space distance along a line of $t = \tau + \tau_0$ can be evaluated. Minima of d lying along lines of slope 1 implies that the distance between the two trajectories is only changing along a single direction and therefore the shapes of the two trajectories are similar. Additionally, when the minima are deep, not only are the dynamics similar, but the flow fields themselves are also similar. The average distance during a shadowing event lasting T seconds may be computed as

$$\bar{d}(t_0, \tau_0, \theta_0) = \frac{1}{T}\int_0^T d(t - t_0, t - \tau_0, \Omega t - \theta_0)\; dt, \tag{5.13}$$

where the shadowing event starts at t_0 along turbulence and τ_0 along the recurrent flow, for an RPO oriented at θ_0 along the azimuth. If $\bar{d}$ is small, the turbulent and RPO flow fields are co-evolve *in physical space* for at least T seconds, as seen in Figure 5.9.

The average distance along a line can be evaluated for any (t_0, τ_0, θ_0), and inspected for when $\bar{d}$ is small. Equation 5.13 may be written as a convolution

$$\begin{aligned}\bar{d}(t_0, \tau_0, \theta_0) &= \int d(t, \tau, \theta) L(t_0 - t, \tau_0 - \tau, \theta_0 - \theta)\; dt\; d\tau\; d\theta \\ &= [L * d](t_0, \tau_0, \theta_0),\end{aligned} \tag{5.14}$$

where $L(t, \tau, \theta) = \delta(\tau - t)\delta(\theta - \Omega t)/T$ is a ‘stencil’ that averages distances only along a line of the proper slopes. Just as in Equation 5.13, $\bar{d}$ is a measure of the quality of shadowing, starting at time t_0 and τ_0, where θ_0 describe which symmetry related trajectory of the RPO is being considered. For most choices of (t_0, τ_0, θ_0), turbulence and the given reccurent solution will not resemble each other whatsoever; this is indicated by $\bar{d}$ being large.

To characterize $\bar{d}$ as “small” or “large,” a distance scale is needed. Generically, a characteristic distance scale, D, can vary substantially throughout state space, as the density of trajectories in state space itself varies. This characteristic distance can even vary along a single recurrent solution (see Figure 5.11). As a result, intervals of shadowing that occur in regions where D is large will result in a larger value of $\bar{d}$ compared with shadowing

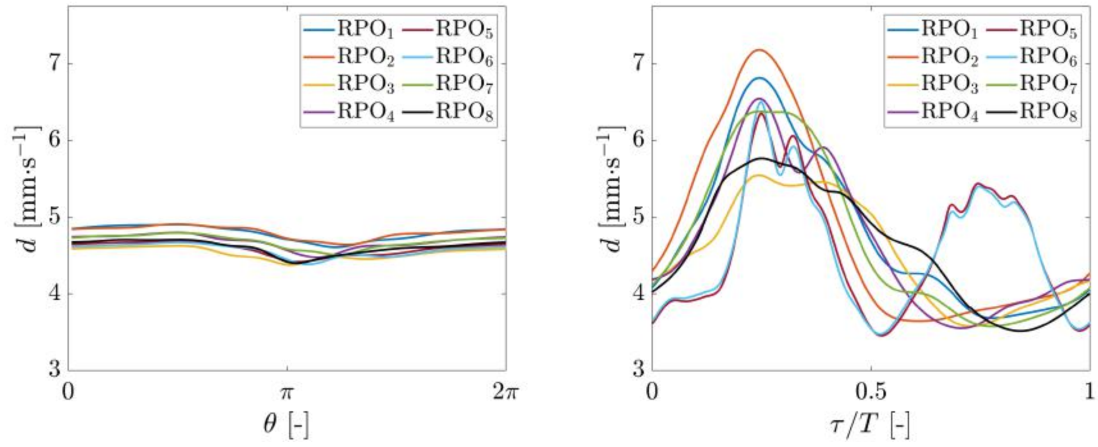

(a) (b)

Figure 5.11: The average distance from each recurrent solution to experimentally obtained turbulence. The average distance, d, is independant of orientation along the azimuthal direction, but depends on τ. (a) Distance from each recurrent solution to turbulence averaged over t and τ. (b) Distance from each recurrent solution to turbulence averaged over t and θ.

events of similar quality in regions where D is small. Thus, to compensate for this intrinsic variation in distance within state space, we define a normalized average distance

$$\tilde{d}(t_0, \tau_0, \theta_0) = \int \frac{d(t, \tau, \theta)}{D(\tau, \theta)} L(t_0 - t, \tau_0 - \tau, \theta_0 - \theta)\, dt\, d\tau\, d\theta, \qquad (5.15)$$

where $D(\tau, \theta)$ is the charicturistic distance scale of state space in the vicinity of $\mathbf{u}(\tau, \theta)$. In general, D may depend on θ. However, TCF is equivariant under rotations along θ, so no θ dependence is expected. The same cannot be said for τ, see Figure 5.11, and as a result D varies only along the RPOs time coordinate. Thus, we define the characteristic length scale

$$D(\tau) = \left[\frac{1}{2\pi T} \int_0^{2\pi} \int_0^T \frac{1}{d(t, \tau, \theta)}\, dt\, d\theta\right]^{-1},$$

as the harmonic mean distance between turbulence and the given RPO. The harmonic mean weights distances closer to the PRO more, which gives a more localized measure of the characteristic inter-trajectory distance to the RPO.

For a shadowing event to be considered significant, it should persist for at least as long as the characteristic escape time of the given RPO. Two trajectories that do not follow eachother for atleast the escape time are most likely not dynamically similar, while events lasting longer than the escape time are dynamically similar for longer than a naive expectation based on the solutions stability would suggest. Therefore, the interval of time which Equation 5.15 is integrated over is chosen to be the characteristic escape time of each RPO, γ_i^{-1}. This choice, though informed by intuition, is somewhat subjective and other choices may also be reasonable.

The quantity, $\tilde{d}$, is a measure of the quality of shadowing. low values correspond to intervals when both the turbulent flow field and its time evolution are well captured by the specific reccurent solution. For larger values of $\tilde{d}$, the apparent similarity of the two flow fields and dynamics is less striking. The degree to which the two flows must resemble one another before it is labeled as “shadowing” is subjective. Figure 5.12 shows an example shadowing event observed in numerically computed turbulence. In this figure, the flow fields at different values of $\tilde{d}$ are plotted to illustrate the subjectiveness of a choise of threshold for labeling an event as “shadowing.”

5.4 Discussion

The results presented here provide the most convincing evidence to date in support of a dynamical description of turbulent flow grounded in the governing equations, as envisioned by Hopf. Turbulent flow does indeed move between neighborhoods of a collection of ECSs, where the evolution of turbulent flow in each neighborhood is well-described by the corresponding ECS. Therefore, this work demonstrates that ECSs in the form of RPOs are important in describing the temporal evolution of turbulence.

An automated method for identifying intervals of time when turbulence is dynamically relevant to a given RPO is essential for any practical implementation of a framework based on RPOs. Here, an automated shadowing detection algorithm based on the shape and prox-

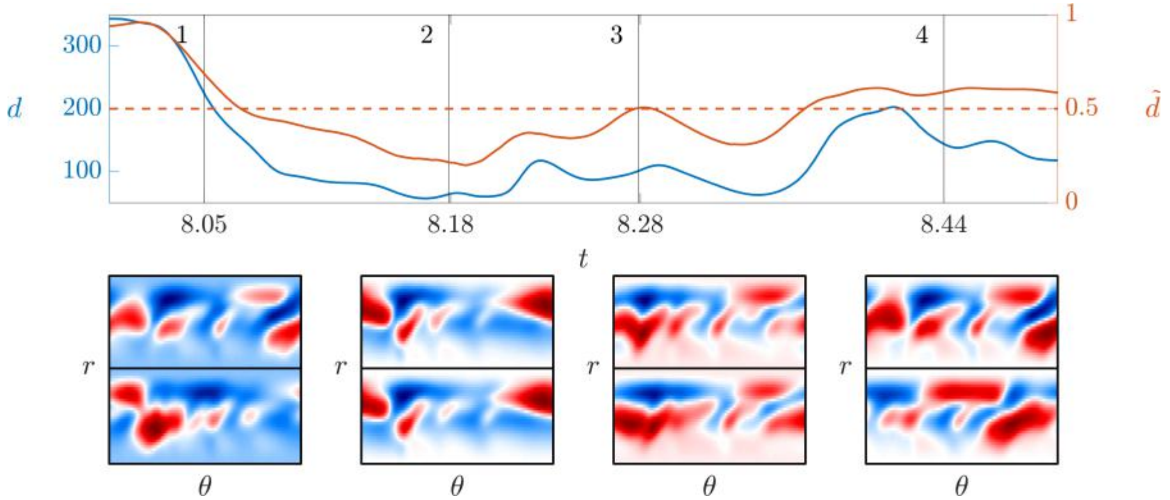

Figure 5.12: PLACEHOLDER of a good quality event to RPO01. The flow fields are at various instances in time, each indicated by a dashed line. For each moment in time, time-ordered from left to right, the mean subtracted azimuthal velocity, $u_\theta - \langle u_\theta \rangle$, is plotted for the (top box) recurrent solution and (bottom box) turbulence. Each rectangular box represents the ring-shaped region spanned by r and θ.

imity of the turbulent trajectory and a given RPO was established. This algorithm produces a parameter, $\tilde{d}$, that was demonstrated that be a measure of quality of shadowing. For a given threshold of quality based on visual inspection of the real-space velocity fields, it was shown that our limited library consisting of only eight RPOs could capture the dynamics of turbulence for about one-third of the time.

While a much larger set of ECSs is required for a complete quantitative description of fluid turbulence, even at the relatively low Reynolds numbers considered here, the results of this study are quite significant. They validate several key assumptions of a deterministic description of turbulence that is grounded firmly in the governing equations of fluid dynamics, and elucidate the relation of the dynamics of coherent structures to the evolution of turbulent flow. Improved understanding of coherent structures promises to shed new light on many long-standing problems, including the role and origin of intermittency and the mechanisms of turbulent cascades. Beyond fluid turbulence, a similar framework should be useful for describing complex dynamics in other high-dimensional systems where strong nonlinearities appear, such as plasmas [215], interacting subatomic particles [216], arrhythmic cardiac tissues [217], neural networks [218], and active matter [219].

CHAPTER 6

CONCLUSIONS

Turbulence is considered by many to be the greatest unsolved problem in classical physics. Although much progress has been made over the years, even basic aspects of a turbulent flow (e.g. pressure drop across a pipe with turbulent flow) have required empirical look-up tables to determine. Many approaches to turbulence employ statistical descriptions which provided little (if any) insight into topics such as prediction or control.

Aside from statistical approaches, fluid mechanicists have been identifying seemingly structured flow patterns in the otherwise disordered turbulence. The role of these flow patterns, called Coherent Structures, has been an outstanding question for many decades. Recent work suggests that these recognizable flow patterns are the turbulence resembling special, non-turbulent flows that are recurrent in time. These special recurrent flows are the basis for a radical new way of thinking about turbulence pioneered by the mathematician Eberhardt Hopf, where turbulence fleetingly but repeatedly resembles these recurrent flows.

Recent advancements in computational techniques have allowed researchers to numerically compute the solutions to the Navier-Stokes equations that exactly recur in time, often called Exact Coherent Structures (ECS). There has been much theoretical and numerical investigation of a description of turbulence based on these ECS, however there has been little experimental work validating this framework. Moreover, the majority of the work in this area has focused around recovering statistical properties of the flows and very little work has addressed questions of dynamics.

In this thesis, I presented the first experimental evidence for the *dynamical* relevance of ECSs in a three dimensional turbulent flow. This work provides convincing evidence in support of a dynamical description of turbulent flow grounded in the governing equations, as envisioned by Hopf.

To validate this dynamical systems description of turbulence, experiments and numerics were carried out in the Taylor-Couette geometry. To be able to perform numerics in a reasonable amount of time, the system was setup with a relatively short axial height to gap width configuration. The Taylor-Couette apparatus had a geometry that differed from the vast majority of what was studied in the literature; therefore, an investigation of the specific Reynolds number at which turbulence occurred was needed. Before settling on which small-aspect ratio the final experiment would be conducted, studies were carried out in a Taylor-Couette system with an intermediate height aspect-ratio (discussed in Chapter 4). While investigating the Reynolds number that turbulence existed, a novel direct, subcritical transition into turbulence was discovered. This transition had the interesting feature of being mediated by a spatially-ordered, temporally chaotic flow. A Reynolds number range for which laminar, turbulence, and this intermediate chaotic flow state were simultaneously stable was discovered. This is, to my knowledge, the first time a system exhibiting bi-stability of two chaotic attractors has ever been observed experimentally.

Although the transition to turbulence exhibited rich and interesting phenomena, the system was still too large to perform tractable tests of the dynamical systems description of turbulence. A new experimental apparatus was designed and constructed with an even smaller height aspect-ratio. This system was designed in a way that provides complete optical access to the flow domain (as described in Chapter 3), which allows for velocimetry measurements throughout the full flow domain. Since the Taylor-Couette geometry is a closed flow, the same turbulent evolution can be studied for an extended duration, making it ideally suited for studying the dynamical systems approach. This system allowed for the first ever direct, quantitative comparisons of experimentally obtained, time-resolved turbulent flow fields in the full flow domain, with direct numerical simulations carried out in the same geometry.

Measurements carried out in this new experimental setup allowed for the first quantitative validation that the time evolution of a turbulent flow is temporarily captured by ECS in the form of Relative Periodic Orbits (RPOs). Even with a rather small set of eight RPOs, the time evolution of the turbulent flow was captured by at least one of the about one-third of the time RPOs (discussed in Chapter 5). To further develop the framework, an algorithm that detects intervals of time where turbulence is dynamically similar to a given RPO was developed. This algorithm produces a quality measure that indicates how similar the dynamics of turbulence is to a segment along the RPO allowing for portions of the RPO to be considered.

Almost all of the previous analysis in the literature has used the entire ECS to preserve the invariance of the solution; however, here we relax that requirement and find that the dynamical similarity of the solutions and turbulence is far more robust to large distances in state space than expected. Even when the turbulent trajectory is not in the linear neighborhood of the RPO, the two flows evolve similarly. This is both surprising and helpful for experimental investigations. The effect of experimental noise is to add a perturbation to the true turbulent trajectory in state space. A small amount of experimental noise would effectively make the turbulent trajectory appear distant to a recurrent solution it may actually by close to.

By taking a step away from the theoretical elegance that using the entire period RPO provides, we are able to effectively capture an impressive fraction of the dynamics with a rather small number of RPOs. However, by taking this step away from the theoretically developed framework, many of the powerful theoretical tools may not be applicable. This means that new tools and intuition need to be developed to further make use of this new tool. For instance, can state space be ‘tiled’ with snippets of RPOs or line-time trajectories? Can symbolic dynamics or a Markov chain be developed using just portions of solutions? Can observable quantities (e.g. instantaneous dissipation) be calculated from an ensemble of shadowing events to portions of RPOs?

Beyond some of these basic questions that need to be answered, there are many exploratory studies that should be conducted. An example of one of these exploratory studies is whether the ECSs are needed at all. The use of ECS brings invariance into the problem and allows for powerful connections to be made to other areas in math and physics, so doing away with their use is a notion that is considered blasphemous by some. However, by looking at shadowing of only portions of the solutions, we are already stepping away from the theoretical solid ground, so how much further can we diverge? Perhaps using snippets or segments of turbulence itself (properly chosen to best tile state space) could be used as the building blocks in the dynamical systems description instead of the invariant solutions. If this is possible, the need for expensive and time-consuming numerical work would be reduced, making this framework much more approachable. Additionally, it may offer a practical way of extending this framework and tool-set to higher Reynolds numbers.

Appendices

APPENDIX A

MATLAB CODES

A.1 px2mmANDeccentricityCalculation

To identify the boundary of the flow domain on the images, a few thousand images of the particles taken from the data set are superimposed to produce well defined region. Canny edge detection is then performed on the stacked image to produce well defined edges of the flow domain. the edge detection image is then cleaned up to remove all edges except the ones corresponding to the inner and outer cylinder. An ellipse is then fit to the two edges using Fit_ellipse from the MATLAB File Exchange [141]. The choice of origin is then taken to be the average of the four focal points of the two ellipsis. The following script determines the domain center, image eccentricity, and nominal px/mm scale factor. The code requires lines 5, 6, 19, and 21 to be edited for best results.

```
1  %% Fit an ellipse to the edge of the cylinders
2  % This code reads in images of the particles and fits an elipse to
3  % the domain edge
4  %% load images in from data
5  FolderName = 'E:\Slice_12_19_2020\2 (Fast)\Camera_1\Data\';
6  N=3000;% How many images to superimpose
7
8  % load them in and sum them together
9  raw = double(ones(1024,1280));%uint16(zeros(1024,1280));
10 for i =1:N
11 raw = sqrt(raw.^2 + (double(imread([FolderName, ...
       sprintf('%07s',num2str(i)), '.tiff']))).^2);
12 end
```

```
DataSet = FolderName;

%% Do the calculations
Center_x = 596; Center_y = 532; % nominal center

% edge detect
BW1 = edge(raw,'canny',0.3);
% mask out troubled regions
BW1(132:251,553:620)=0; BW1(261:489,887:895)=0; ...
    BW1(500:700,500:700)=0; BW1(834:944,570:586)=0; ...
    BW1(923:927,710:717)=0;

%find the locations of the edge
[y_image,x_image]=find(BW1>0.5);

%split into inner and outer
x_inner = x_image(sqrt((x_image-Center_x).^2 + ...
    (y_image-Center_y).^2) < 380);
y_inner = y_image(sqrt((x_image-Center_x).^2 + ...
    (y_image-Center_y).^2) < 380);
x_outer = x_image(sqrt((x_image-Center_x).^2 + ...
    (y_image-Center_y).^2) > 380);
y_outer = y_image(sqrt((x_image-Center_x).^2 + ...
    (y_image-Center_y).^2) > 380);

 % fit to an ellipse
ellipse_out = fit_ellipse_CJC(x_outer,y_outer);
a_out = ellipse_out.a; b_out = ellipse_out.b; x0_out = ...
    ellipse_out.X0_in; y0_out = ellipse_out.Y0_in;
Eccentricity_out = sqrt(1-(min([b_out/a_out,a_out/b_out]))^2);
px2mm_out_x = a_out/70.42; px2mm_out_y = b_out/70.42;

ellipse_in = fit_ellipse_CJC(x_inner,y_inner);
```

```
a_in = ellipse_in.a; b_in = ellipse_in.b; x0_in = ellipse_in.X0_in; ...
    y0_in = ellipse_in.Y0_in;
Eccentricity_in = sqrt(1-(min([b_in/a_in,a_in/b_in]))^2);
px2mm_in_x = a_in/50; px2mm_in_y = b_in/50;

px2mm_i = [px2mm_out_x, px2mm_in_x, px2mm_out_y, px2mm_in_y];
px2mm = mean(px2mm_i); px2mm_std = std(px2mm_i);

disp(['X = ',num2str((x0_out+x0_in)/2),' [px]'])
disp(['Y = ',num2str((y0_out+y0_in)/2),' [px]'])
disp(['X = ',num2str((x0_out+x0_in)/2/px2mm),' [mm]'])
disp(['Y = ',num2str((y0_out+y0_in)/2/px2mm),' [mm]'])
disp(['px/mm = ',num2str(px2mm),' ± ',num2str(px2mm_std)])
disp(['mm/px = ',num2str(1/px2mm)])
disp(['r_i = ',num2str(50*px2mm),' [px]'])
disp(['r_o = ',num2str(70.42*px2mm),' [px]'])
disp(['Eccentricity = ', num2str((Eccentricity_out+Eccentricity_in)/2)])

end
```

A.2 Spectrumizer

A.2.1 Fit data to the spectrum

The following function fits data do a Fourier-Chebychev spectrum. The function requires the file path and file name (pivLaminarName), the number of grid points to perform the fit on (nr and nt), as well as parameters about the geometry (x_shift, y_shift, spaceScale, and TimeScale). The code improves the quality of the fit by enforcing the zero-slip boundary condition on the inner and outer cylinders. To do this, the code also needs to know the rotation frequency of the cylinders determined by the motors (f_in and f_out). For more details, see subsubsection 3.3.3

```
function [coeff_th,coeff_r] = Spectrumizer(pivFileName, nr, nt, ...
    x_shift, y_shift,  spaceScale, TimeScale, f_in, f_out)
%%%%%%%%%%%%%%%%%%%%%%%%%%%%%%%%%%%%%%%%%%%%%%%%%%%%%%%%%%%%%%%%%%%%
%%%%%%%%% Fit 2D DaVis data to spectrum (Cheby-Fourier) %%%%%%%%%%%
%%%%%%%%%%%%%%%%%%%%%%%%%%%%%%%%%%%%%%%%%%%%%%%%%%%%%%%%%%%%%%%%%%%%
% This function reads in 2D Cartesian data from DaVis output .dat
% files and fits it to a spectrum that is Chebychev in r and Fourier
% in \theta. The fit applies a weight function based local on the PIV
% uncertainty.

%% parameters
ro = 70.42; ri = 50.0; d = ro-ri;
%% Load the PIV
[rho_in, theta_in ,Vr_in, Vth_in, StdVr_in, StdVth_in, UVr_in, ...
    UVth_in] = PIV_Slice_TCF_readANDconvert(pivFileName, x_shift, ...
    y_shift, spaceScale, TimeScale);

% Remove the NaNs
rho = rho_in(¬isnan(rho_in)); theta = theta_in(¬isnan(theta_in)); Vr ...
    = Vr_in(¬isnan(Vr_in)); Vth = Vth_in(¬isnan(Vth_in)); StdVr = ...
    StdVr_in(¬isnan(StdVr_in)); StdVth = ...
    StdVth_in(¬isnan(StdVth_in)); UVr = UVr_in(¬isnan(UVr_in)); UVth ...
    = UVth_in(¬isnan(UVth_in));

% establishing the boundary rotation velocity
BoundaryCondition_in = f_in*2*pi*ri;
BoundaryCondition_out = f_out*2*pi*ro;

%% Actually do the fit to the spectrum
% scaling the coordinants to fit into chebyshev
% MAKE SURE THESE GO FROM -1 TO 1
x = (2*rho-ri-ro)/d;

```

```
% Put data on the boundaries to encourage the boundary conditions
temp = linspace(0,2*pi,1000);temp = temp(1:end-1)';
alpha = 100; %weight value for boundary

% creat a weight function for the fit based on uncertianty
weight_v = 1./(UVth.^2+UVr.^2);
weight_v = weight_v(:);

% construct the A matrix (i.e. a 2D array of all the spectral terms
% evaluated at the location of the particles). Where A*coeff = v
k = 0:nr; m = 0:nt-1; [K,M] = meshgrid(k,m); % generate the mexh in ...
    spec space
x = [x(:);-ones(size(temp));ones(size(temp))]';
K = K(:)';
theta = [theta(:);temp;temp]';
M = M(:)';
ChebyPart = cos(K'*acos(x));
spec_odd  =  sin(M'*theta).*ChebyPart;
spec_odd(1,:) = sin(nt*theta).*ChebyPart(1,:);
spec_even =  cos(M'*theta).*ChebyPart;
clear ChebyPart K

% put the A matrix together
A = [spec_odd; spec_even]';

A(end-2*numel(temp):end,:) = alpha*A(end-2*numel(temp):end,:); % ...
    apply the boundary weights
A(1:end-2*numel(temp),:) = weight_v.*A(1:end-2*numel(temp),:); % ...
    apply the uncertianty weight
% establish boundary condition
Vth = [Vth;BoundaryCondition_in.*ones(size(temp));...
    BoundaryCondition_out.*ones(size(temp))];
```

```
Vth(end-2*numel(temp):end) = alpha*Vth(end-2*numel(temp):end); % ...
    apply the boundary weights
Vth(1:end-2*numel(temp)) = weight_v.*Vth(1:end-2*numel(temp)); % ...
    apply the uncertianty weights
Vr = [Vr;0*ones(size(temp));0*ones(size(temp))];
Vr(end-2*numel(temp):end) = alpha*Vr(end-2*numel(temp):end);
Vr(1:end-2*numel(temp)) = weight_v.*Vr(1:end-2*numel(temp));

% solve for the optimal spectrum
warning('off')
coeff_th = A\Vth; coeff_r = A\Vr;
warning('on')

end
```

A.2.2 Plot the velocity fields represented by the spectrum

The spectrum that is produced by PIV_Slice_TCF_Spectrumizer often needs to be plotted. To plot the resulting velocity field, the A matrix is needed to be regenerated or read in from an existing file. The following code can be used to plot the spectrum.

```
nr_plt = 33;
nt_plt = 128;
xOut = linspace(-1, 1, nr_plt+1); thetaOut = linspace(-pi, pi, nt_plt);
[Xout,THout] = meshgrid(xOut,thetaOut);
% construct the A matrix where A*coeff = v
k = 0:nr; m = 0:nt-1; [K,M] = meshgrid(k,m);
Xout = Xout(:)';
K = K(:)';
THout = THout(:)';
M = M(:)';
ChebyPart = cos(K'*acos(Xout));
```

```
spec_odd   =  sin(M'*THout).*ChebyPart;
spec_even =  cos(M'*THout).*ChebyPart;
clear ChebyPart K
% put the A matrix together
Aout = [spec_odd; spec_even]';
xOut = linspace(ri, ro, nr_plt+1); thetaOut = linspace(-pi, pi, nt_plt);
[THout, Xout] = meshgrid(thetaOut, xOut);
Yout = Xout.*sin(THout); Xout = Xout.*cos(THout);
V_th = reshape(Aout*coeff_th, [nt_plt,nr_plt+1]);
V_r = reshape(Aout*coeff_r, [nt_plt,nr_plt+1]);

contourf(Xout',Yout',V_th,50,'EdgeColor','none')
figure
contourf(Xout',Yout',V_r,50,'EdgeColor','none')
```

A.3 HeightFinder

Whenever making 2D-2C measurements of turbulence, the system is also prepared in the $Re_i = 300$ and $Re_o = 0$ laminar flow and a flow field is captured. The PIV velocity field, $\mathbf{V}_{\text{PIV}}$, is then converted into cylindrical coordinates and compared with the laminar flow, $\mathbf{V}_{\text{Sim}}$, computed in numerics. The following code reads in the numarically computed laminar flow (whose path is specified in line 3) and compares it against the 2D-2C measurement data. To run this code, lines 2 through 10 should be adjusted to reflect the data set. For more details, see subsubsection 3.3.1

```
1 %% parameters
2 pivLaminarName = 'D:\Data\ExampleLaminar\8\align0001.dat';
3 simLaminarName = "g1_eta71_300_0.converged";
4 scale = 1;
5 x_shift = 0;
```

```
y_shift = 0;
spaceScale = 1; %mm/pix,fl
timeScale = 1/1;
nu = 1.6279;
ro = 70.42; ri = 50.0; h = ro-ri; zmin = -h/2; zmax = h/2; eta = ri/ro;

%% read in the numerics
[domain,vrc,vtc,vzc,¬,¬,¬] = fortran.readphysicalfile(simLaminarName);
nr = domain.nr; nz = domain.nz; nt = domain.nt;

% put it into dimensional units, still non-uniform in r and z
[vrc,vtc,vzc] = convert2dimensional(vrc,vtc,vzc,ri,ro,nu);
rc = domain.r; zc = domain.z;
[Zc,Rc] = meshgrid(zc,rc);

% the grid we want
Nz = nz*100;
z = linspace(zmin,zmax,Nz); r = linspace(ri,ro,nr); th = ...
    linspace(-pi,pi,nt+1);
th = th(1:(end-1)); % remove the doubled up end point
[Z,R] = meshgrid(z,r);

% interp solution to uniform grid
VthSol = repmat(interp2(Zc, Rc, vtc(:,:,1), Z, R, 'makima'), ...
    [1,1,length(th)]);
VrSol = repmat(interp2(Zc, Rc, vrc(:,:,1), Z, R, 'makima'), ...
    [1,1,length(th)]);

%% Load the PIV
[rho_in, theta_in, Vr_in, Vth_in, StdVr_in, StdVth_in, UVr_in, ...
    UVth_in] = PIV_Slice_TCF_readANDconvert(pivLaminarName, x_shift, ...
    y_shift, spaceScale, timeScale);

```

```
rho = rho_in(¬isnan(rho_in)); theta = theta_in(¬isnan(theta_in)); Vr ...
    = Vr_in(¬isnan(Vr_in)); Vth = Vth_in(¬isnan(Vth_in)); StdVr = ...
    StdVr_in(¬isnan(StdVr_in)); StdVth = ...
    StdVth_in(¬isnan(StdVth_in)); UVr = UVr_in(¬isnan(UVr_in)); UVth ...
    = UVth_in(¬isnan(UVth_in));

[R2,TH2] = meshgrid(r,th);

VrPIV = griddata(theta-pi, rho,Vr*1000*scale, TH2, R2, 'cubic');
VthPIV = griddata(theta-pi, rho,Vth*1000*scale, TH2, R2, 'cubic');
UVrPIV = griddata(theta-pi, rho,sqrt(UVr.^2+StdVr.^2)*1000*scale, ...
    TH2, R2, 'cubic');
UVthPIV = griddata(theta-pi, rho,sqrt(UVth.^2+StdVth.^2)*1000*scale, ...
    TH2, R2, 'cubic');

VrPIV = permute(repmat(VrPIV,[1,1,Nz]),[2,3,1]); % puts it in (r,z,th)
VthPIV = -permute(repmat(VthPIV,[1,1,Nz]),[2,3,1]);
UVrPIV = permute(UVrPIV,[2,1]);
UVthPIV = permute(UVthPIV,[2,1]);

%% find the min
for t = 1:size(VthPIV,3)
rms_zlevels = squeeze(nanmean( (((VrPIV(:,:,t) - ...
    VrSol(:,:,t))./repmat(UVrPIV(:,t),[1,length(z)]) ).^2 + ...
    ((VthPIV(:,:,t) - VthSol(:,:,t))./repmat(UVthPIV(:,t), ...
    [1,length(z)])).^2), 1))  ;
        if isnan(sum(rms_zlevels))
            rmsMin(t) = nan; zHeights(t) = nan;
        else
            rmsMin(t) = find(rms_zlevels == min(rms_zlevels));
            zHeights(t) = z(rmsMin(t));
        end
end
```

```
Zout = (zHeights);

%% fit to a plane
ft = fittype('a*cos(x) + b*sin(x) + ...
    ofset','coefficients',{'a','b','ofset'});
ValidPoints = ¬isnan(Zout);
plane = ...
    fit(th(ValidPoints)',Zout(ValidPoints)',ft,'startpoint',[0.63,0.22,1]);
a = 2*plane.a/(ri+ro);
b = 2*plane.b/(ri+ro);
alpha = a;
beta = b;
z0 = plane.ofset;

disp(['z-height: ',num2str(plane.ofset)])
disp(['slope in x: ',num2str(a),', slope in y: ',num2str(b)])
disp(['theta_x: ',num2str(radtodeg(atan(a))),', theta_y: ...
    ',num2str(radtodeg(atan(b)))])
disp('==============================================')

%% Helper functions
function [VRd,VTd,VZd] = convert2dimensional(VR,VT,VZ,ri,ro,nu)
    d = ro - ri; % unit length = gap width in mm
    td = d^2/nu; % unit time = viscous diffusion time
    VRd = VR*(d/td); % dimensional radial velocity field
    VTd = VT*(d/td); % dimensional azimuthal velocity field
    VZd = VZ*(d/td); % dimensional axial velocity field

end
```

APPENDIX B

CALIBRATION TARGET DESIGN FOR 3D-3C

There are not many constraints on the geometry or appearance of the calibration target used in a multi camera system. Because of this, there are few discussion in the literature on their design (e.g. [220, 162, 89, 221]). For many applications, a target can be purchased from companies such as LaVision or Dantec, but some experimental setups require specialized targets. The design and manufacturing of a three dimensional calibration target is relatively easy and very inexpensive if one has access to the proper tools.

When designing a three dimensional calibration target for use with a multi-camera system, there are a few considerations that help narrow the design. For a calibration target based on a regular dot pattern, here are a few considerations:

- The dots need to be large enough and contrasted against the background enough that they are clearly seen and identified on each camera image
- The calibration marks on all planes must be visible from cameras pointing at the target at an angle
- The dot need to be spaced dense enough that each camera sees at least $\sim$10 dots from each plane

An example calibration target design is shown in Figure B.1. This target has two planes of dots regularly spaced a distance w apart within the plane. The planes are separated by a distance D and the dots of diameter d are centered within the grooves. These three dimensions give a constraint on d, D, w, and camera viewing angle, θ ensuring that the dots are not obstructed by the target geometry. The full dot will be seen as long as

$$d \leq w + 2D \tan\left[\theta\right] \tag{B.1}$$

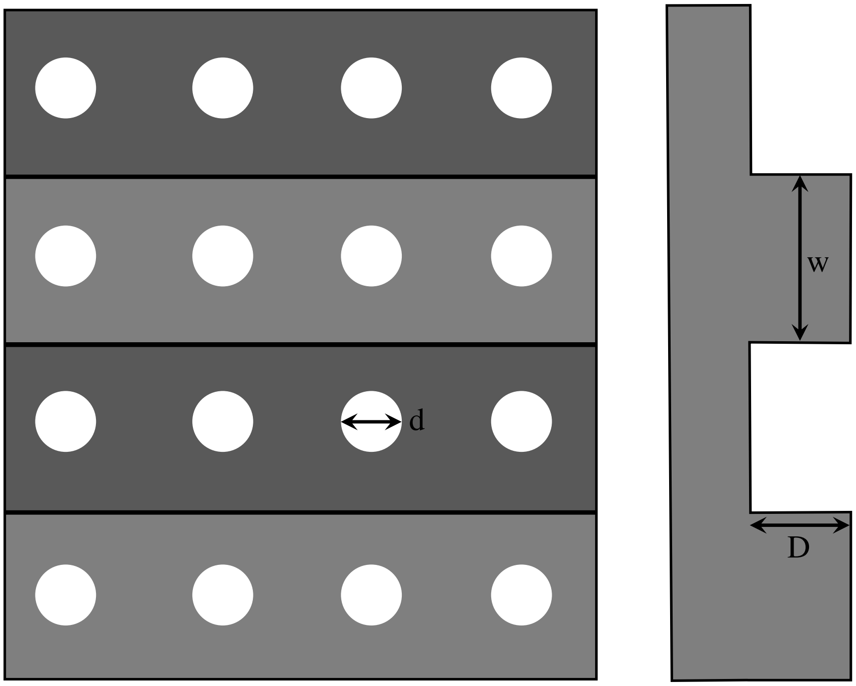

Figure B.1

is satisfied.

Once the dimensions are chosen, the groove pattern can be cut out of aluminum using a mill. After the grooves have been cut, the plate can then be anodized flat black. Then, the dot pattern can be produced by using a laser cutter to ablate away the anodizing. Alternatively, if a laser cutter is not available, a #00 carbide center drill[1] can be used to mechanically remove the anodizing. The hardness of the anodized layer exceeds that of cast iron [222], so new, hardened tools are needed. By first punch through the anodizing, then going over each hole with a new tool, going down 0.001 in with a 1 s dwell time, the anodizing can be removed.

---

[1] Since only the very tip of the tool is going to be used and the tip has a different angle than the tools "cut angle", it doesn't matter which tool is used.

APPENDIX C

TORQUE MEASUREMENT CAPABILITIES

Angular momentum transport plays a key roll in many flows. A time-resolved measurement of angular momentum transport from the inner and outer cylinders along with PIV or PTV measurements could possibly be used as a separate measure of the state of the flow. In the limit as $\Gamma \to \infty$, the angular momentum transport from the inner cylinder to the outer cylinder (and *vice versa*) is the sum of the torque on the outer cylinder. There are modern TCF apparatuses that have been built to measure angular momentum transport this way [87, 101, 223, 224]. In these systems, the middle portion of the inner cylinder is constructed to only be attached to the driving through a torque sensor (see Figure C.1). The torque measurement is only made on the middle portion of the flow to avoid contributions from the top and bottom end caps. As Γ decreases, the contribution from the end effects become non-negligible everywhere in the domain, making comparisons to generic turbulence investigations dubious at best; however, torque measurements may be a very useful diagnostic for determining global properties of the flow such as drag.

The TCF apparatus used in this thesis was originally designed with the possibility of torque measurements in mind. Both inner and outer cylinders are driven by shafts that are split, allowing for a torque measurement to be made in the shaft itself. The torque measurement could be made in a similar fashion to Lathrop's design [224]. In this approach, the motor side of the shaft is coupled to the cylinder side of the shaft via a (or several) thin piece of metal. As the torque on the cylinder increases, the thin strip of metal will bend. By outfitting a strain gauge to either side of the metal arm, the deflection can be measured.

The signal coming from the strain gauges adhered to the thin metal coupling can be measured with relatively low noise by using a lock-in amplifier. The two strain gauges on either side of the metal arm will change their resistance in opposite directions, therefore,

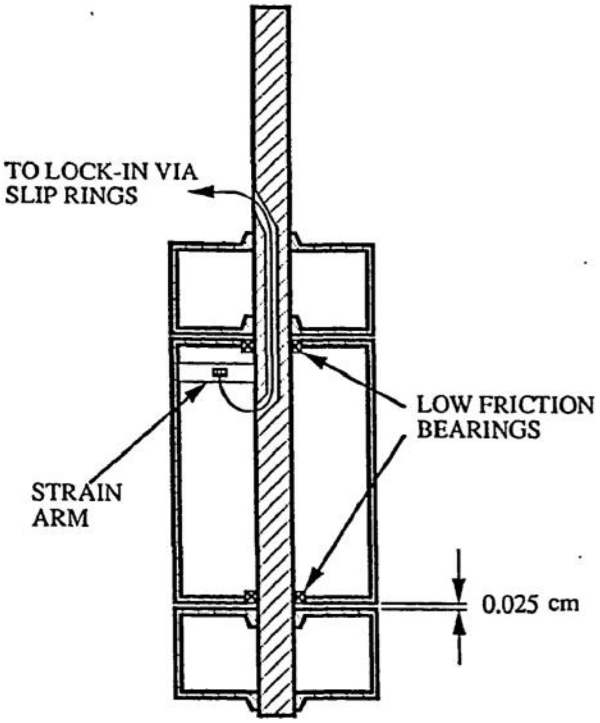

Figure C.1: Example split cylinder design for measuring torque. The middle portion of the inner cylinder is separated from the top and bottom portions and only coupled to the shaft through a strain gauge. This design allows for torque measurements of the center portion of the flow domain, where axial end effects are minimal. Figure taken from Lathrop (1992) [224].

by measuring the resistance in a Wheatstone bridge configuration, the resistance can be determined quite accurately. For more information on how this measurement is set up, see Chapter 4 of Lathrop's thesis [224].

In addition to the torque caused by the working fluid, there are three other sources of drag that need to be accounted for: bearing drag, drag from the working fluid in the thin gaps between the inner cylinder and the top/bottom end caps, and viscous drag from outer cylinder submerged in a cooling reservoir. The number of bearings in the design for the portion of the shaft between the strain gauges and the cylinder is minimized and the bearings are high quality, ceramic bearings which introduce very little friction. The gap between the inner cylinder and end caps is small (0.5 mm in the current construction), therefore, the flow in there will be laminar, and the drag can be calculated and corrected for. Bellow, in Section C.1, is a calculation of the viscous drag in this gap. The drag from the outer cylinder in the cooling reservoir is slightly more challenging to calculate due to its complicated geometry. The drag can easily be measured as a function of Re_o by running the system without working fluid or the inner cylinder present.

C.1 Contribution to torque from gap between inner cylinder and end caps

There is a small gap between the inner cylinder and the top and bottom end cap that is filled with the working fluid. The gap is small (about 0.5 mm in the current construction), so there will be drag and therefore it will contribute to any torque measurement. To calculate the approximate contribution to the torque measurement, the flow in the gap is assumed to be laminar, since the gap is small. For our geometry, the torque, T, can be calculated from the a drag force, F_drag, as

$$T = \int dr \left(r F_\text{drag}(r) \right). \tag{C.1}$$

The force of drag along an infinitesimal ring of radius r, $F_\text{drag}(r)$, can be calculated by integrating the shear stress, τ, along the circumference of the ring, which is simply

$$F_\text{drag}(r) = \int_0^{2\pi} d\theta r \tau = 2\pi r \tau. \tag{C.2}$$

For a Newtonian fluid, the shear stress is

$$\tau = \mu \partial_z v \tag{C.3}$$

and if the flow is laminar between the two surfaces, then this can be evaluated as a function of the relative velocity between the two surfaces, $v_{\theta,\text{tot.}}$, as

$$\begin{aligned}\partial_z v &= \frac{v_{\theta,\text{tot.}}}{\Delta z} \\ &= \frac{|v_{\theta,\text{i}}| + |v_{\theta,\text{o}}|}{\Delta z} \\ &= \frac{\left(|\omega_\text{i}| + |\omega_\text{o}|\right) r}{\Delta z}.\end{aligned} \tag{C.4}$$

In order to rewriting Equation C.4 in terms of Re_i and Re_o, the definition of Re for TCF is first inverted solving for ω_i and ω_o,

$$|\omega_\text{i}| = \frac{|Re_\text{i}|\nu}{r_\text{i}\left(r_\text{o} - r_\text{i}\right)} = \frac{|Re_\text{i}|\nu}{r_\text{i}^2\left(1/\eta - 1\right)} \tag{C.5}$$

and,

$$|\omega_\text{o}| = \frac{|Re_\text{o}|\nu}{r_\text{o}\left(r_\text{o} - r_\text{i}\right)} = \frac{|Re_\text{o}|\nu}{r_\text{i}^2 \frac{1}{\eta}\left(1/\eta - 1\right)}. \tag{C.6}$$

Then, substituting Equation C.5 and Equation C.6 into Equation C.4 gives,

$$v_{\theta,\text{tot.}}(r) = r\frac{\nu\left(|Re_\text{i}| + \eta|Re_\text{o}|\right)}{r_\text{i}^2\left(1/\eta - 1\right)}. \tag{C.7}$$

Finally, substituting Equation C.7 into Equation C.1 and Equation C.2, we get

$$\begin{aligned}T &= \int drr^3 2\pi\mu\frac{\nu\left(|Re_\text{i}| + \eta|Re_\text{o}|\right)}{\Delta z r_\text{i}^2\left(1/\eta - 1\right)} \\ &= \frac{\mu^2}{\rho}\frac{2\pi}{r_\text{i}^2\Delta z}\frac{\eta}{1-\eta}\left(|Re_\text{i}| + \eta|Re_\text{o}|\right)\int drr^3.\end{aligned} \tag{C.8}$$

The torque from the fluid drag between the inner cylinder and the bottom cap, we get by evaluating the integral in Equation C.8 from 0 to r_i. This gives us

$$\boxed{T_\text{bottom} = \frac{\mu^2}{\rho}\frac{\pi r_\text{i}^2}{2\Delta z_\text{bottom}}\frac{\eta}{1-\eta}\left(|Re_\text{i}| + \eta|Re_\text{o}|\right)} \tag{C.9}$$

Similarly, to find the torque from the drag on the top, we evaluate Equation C.8 from r_shaft to r_i and get

$$\boxed{T_\text{top} = \frac{\mu^2}{\rho} \frac{\pi}{2\Delta z_\text{top}} \left(r_\text{i}^2 - \frac{r_\text{shaft}^4}{r_\text{i}^2} \right) \frac{\eta}{1-\eta} \left(|Re_\text{i}| + \eta |Re_\text{o}| \right)} \tag{C.10}$$

Though these two are not explicitly the same, the main difference is $r_\text{shaft}^4 / r_\text{i}^2$, which for the current design of the system ($r_\text{shaft} = 12$ mm and $r_\text{i} = 50$ mm) is a 0.33 % correction. Therefore, this term can be neglected without incurring much error. The only other difference is gap width; however, because the distance between the top and bottom end caps are fixed, the sum of the two gap widths are a constant (i.e. $\Delta z_\text{top} + \Delta z_\text{bottom} = \Delta z$). When assembling the cell, the inner cylinders location in z is chosen such that it minimize the drag when it is spun. This means that, to good approximation, the gap widths are equal. Therefore, the total torque is

$$\boxed{T = \frac{\mu^2}{\rho} \frac{2\pi r_\text{i}^2}{\Delta z} \frac{\eta}{1-\eta} \left(|Re_\text{i}| + \eta |Re_\text{o}| \right)} \tag{C.11}$$

APPENDIX D

MECHANICAL DRAWINGS OF NEW TAYLOR-COUETTE APPARATUS

D.1 Camera mount adapters

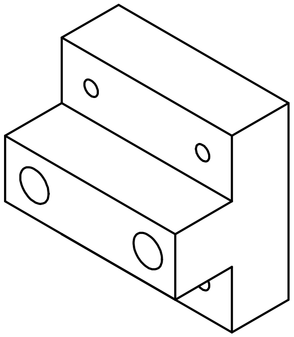

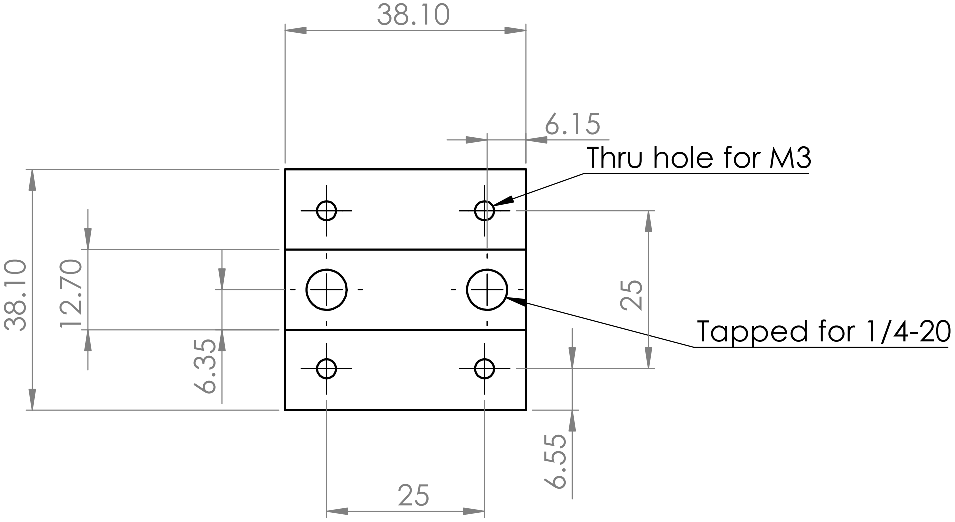

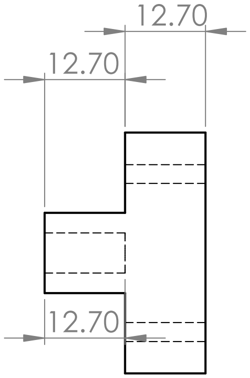

Part name:	Camera T-mount adapter
Material:	Aluminum
Units:	mm
Designer:	Chris Crowley

D.2 Split shaft assembly

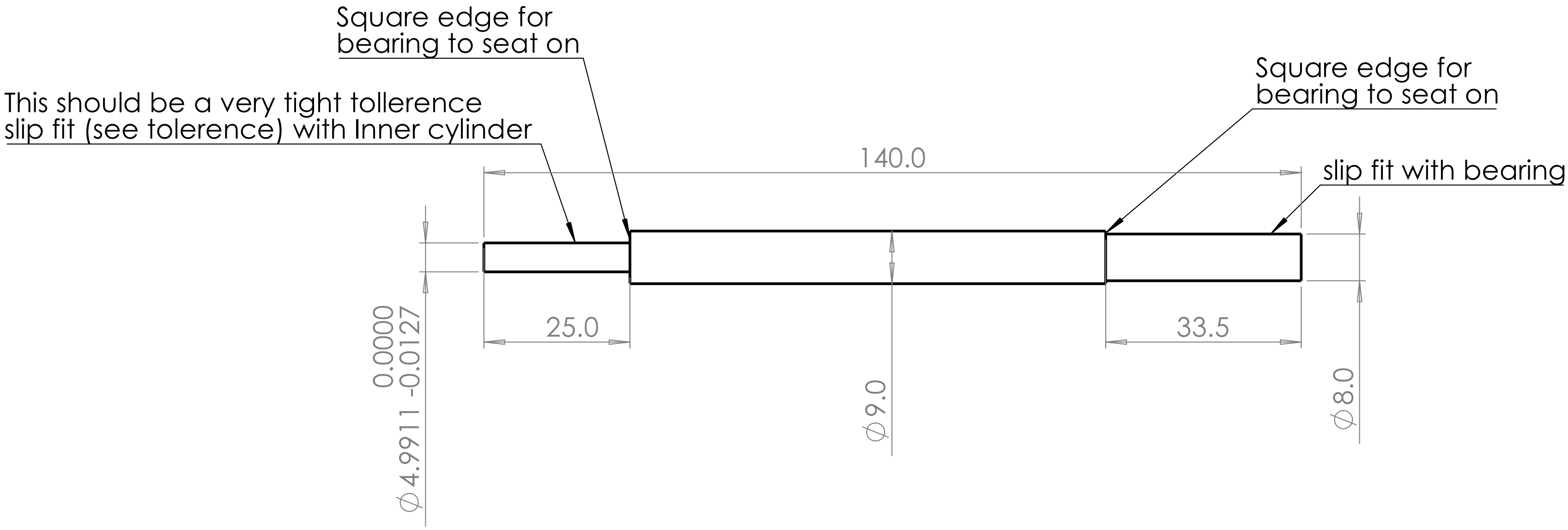

Square edge for bearing to seat on

This should be a very tight tollerence slip fit (see tolerence) with Inner cylinder

Square edge for bearing to seat on

slip fit with bearing

Part name:	Inner cylinder lower shaft (for split shaft assembly)
Material:	316 Stainless Steel
Units:	mm
Designer:	Chris Crowley

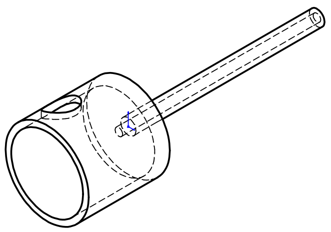

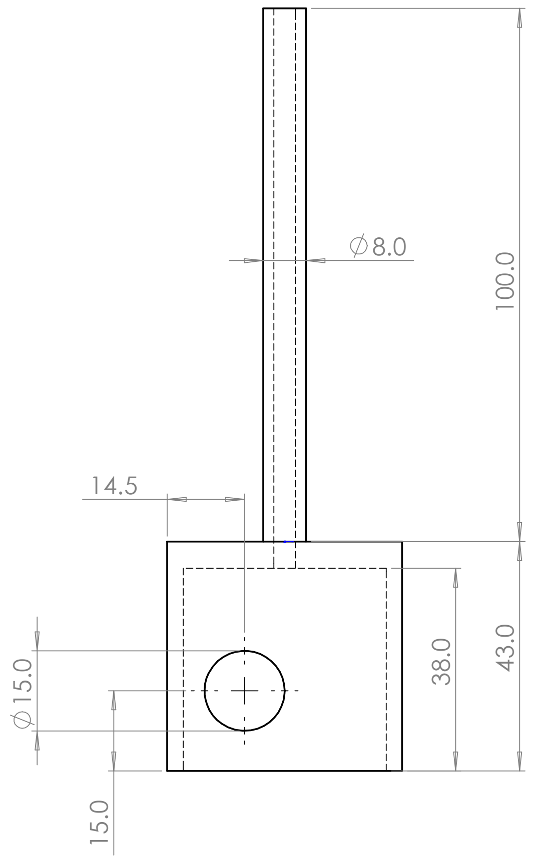

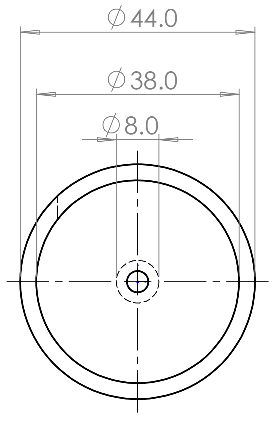

Part name:	Inner cylinder upper shaft (for split shaft assembly)
Material:	Aluminum
Units:	mm
Designer:	Chris Crowley

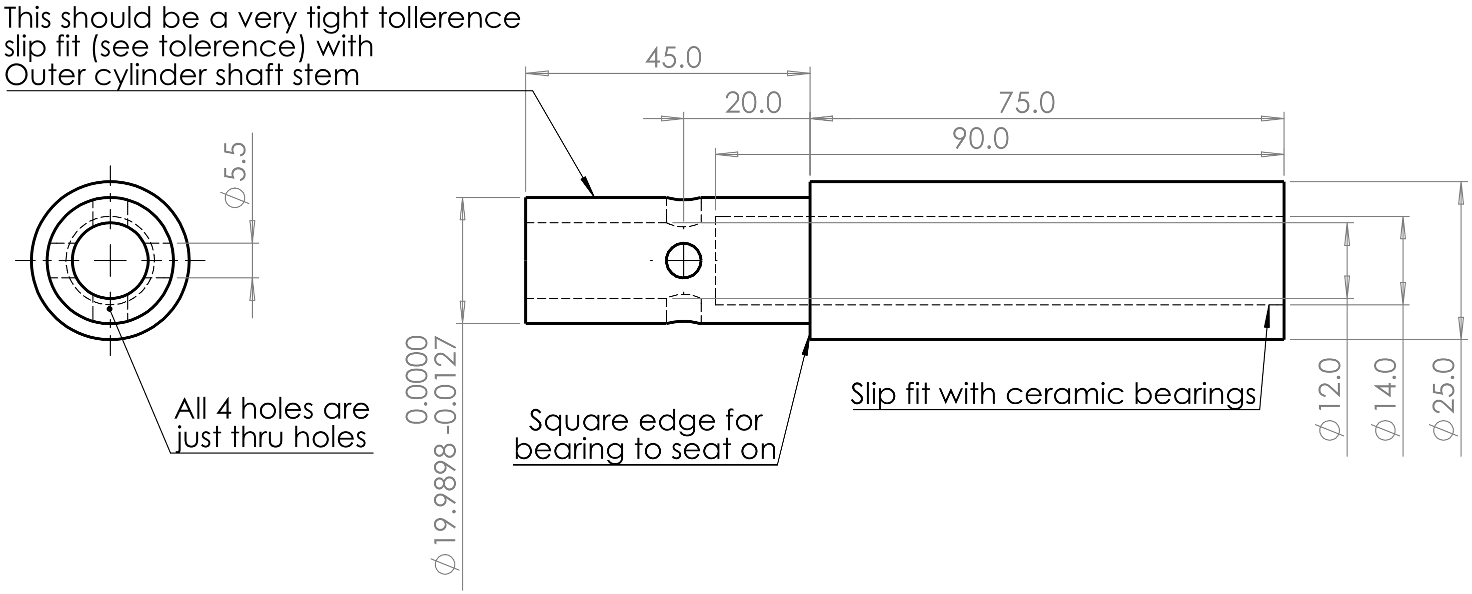

Part name:	Outer cylinder lower shaft (for split shaft assembly)
Material:	316 Stainless Steel
Units:	mm
Designer:	Chris Crowley

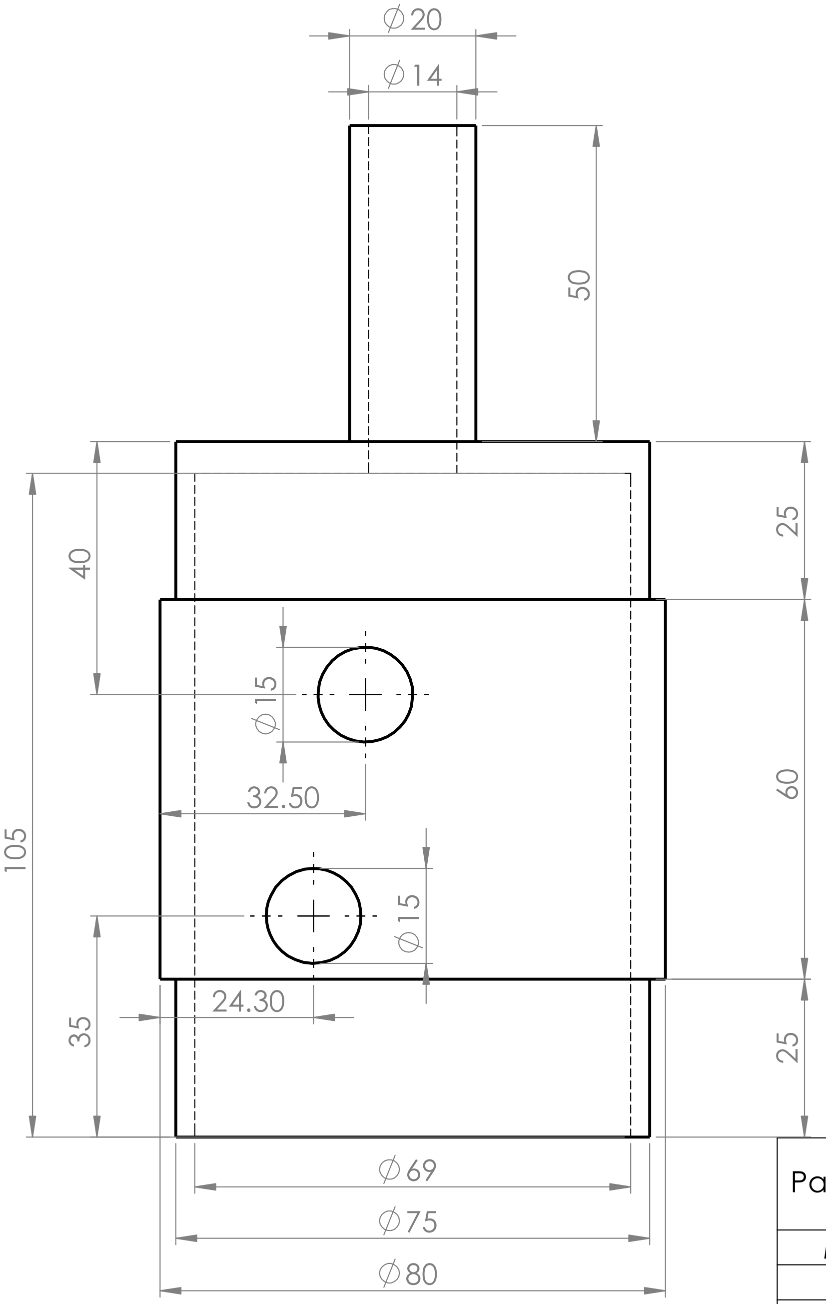

Part name:	Outer cylinder upper shaft (for split shaft assembly)
Material:	316 Stainless Steel
Units:	mm
Designer:	Chris Crowley

D.3 Cell parts

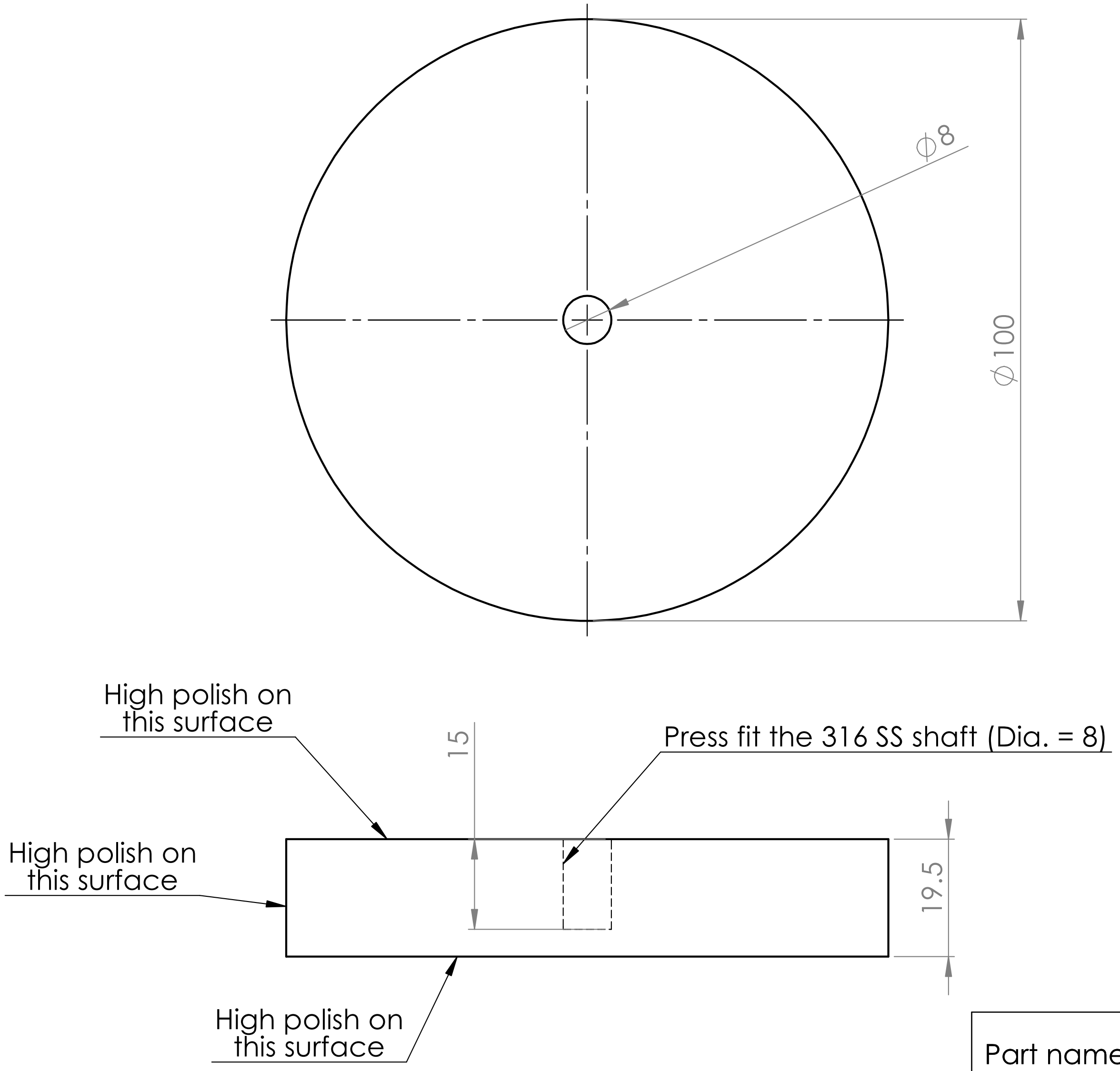

Part name:	Inner cylinder (eta = 0.71)
Material:	Cast Acrylic
Units:	mm
Designer:	Chris Crowley

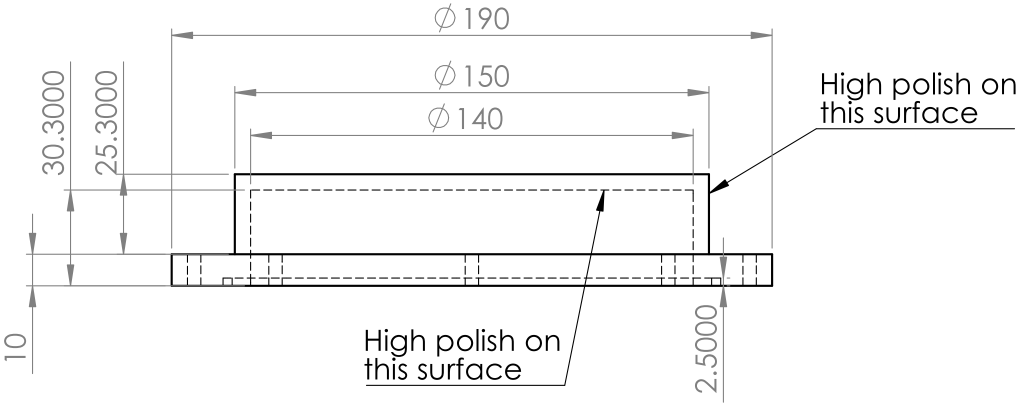

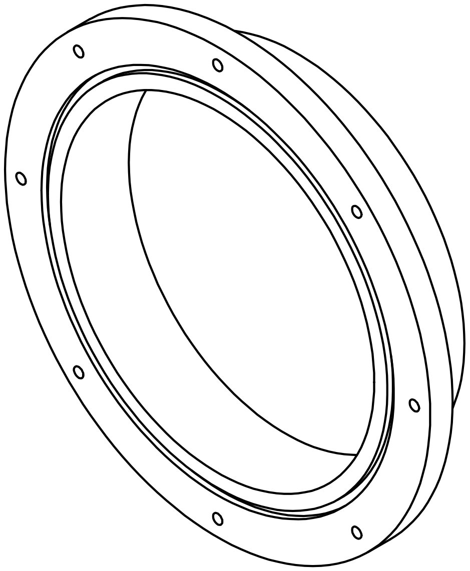

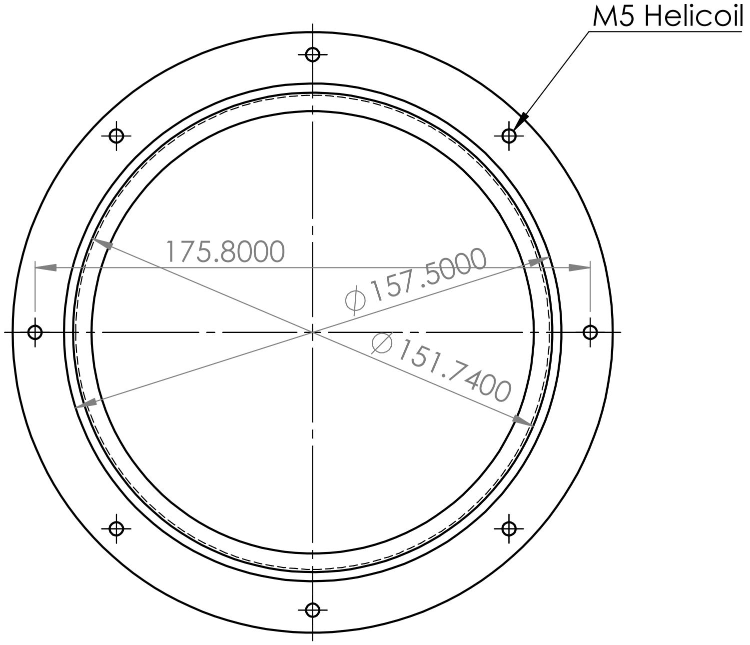

Part name:	Outer cylinder bottom (eta = 0.71)
Material:	Cast Acrylic
Units:	mm
Designer:	Chris Crowley

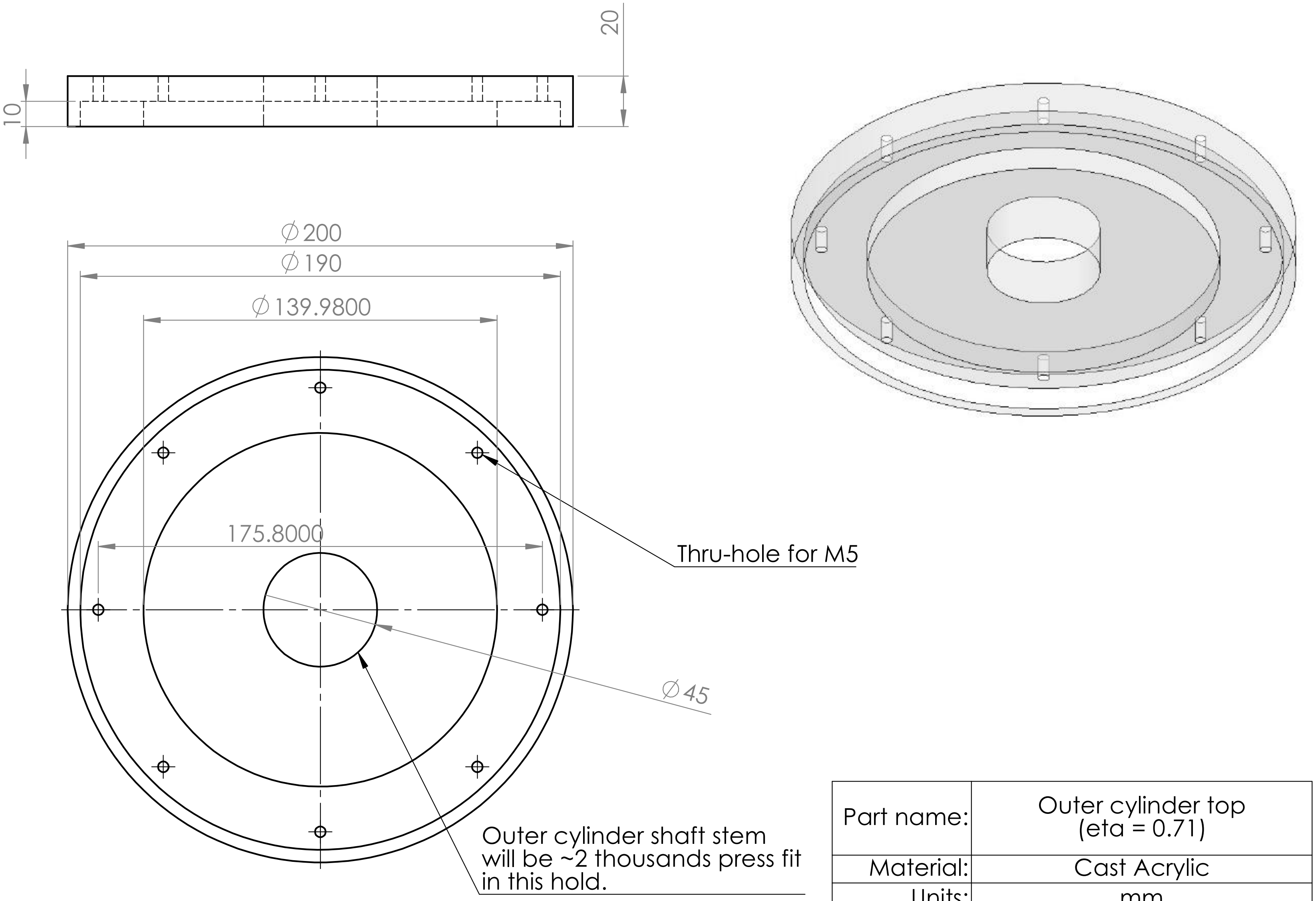

Part name:	Outer cylinder top (eta = 0.71)
Material:	Cast Acrylic
Units:	mm
Designer:	Chris Crowley

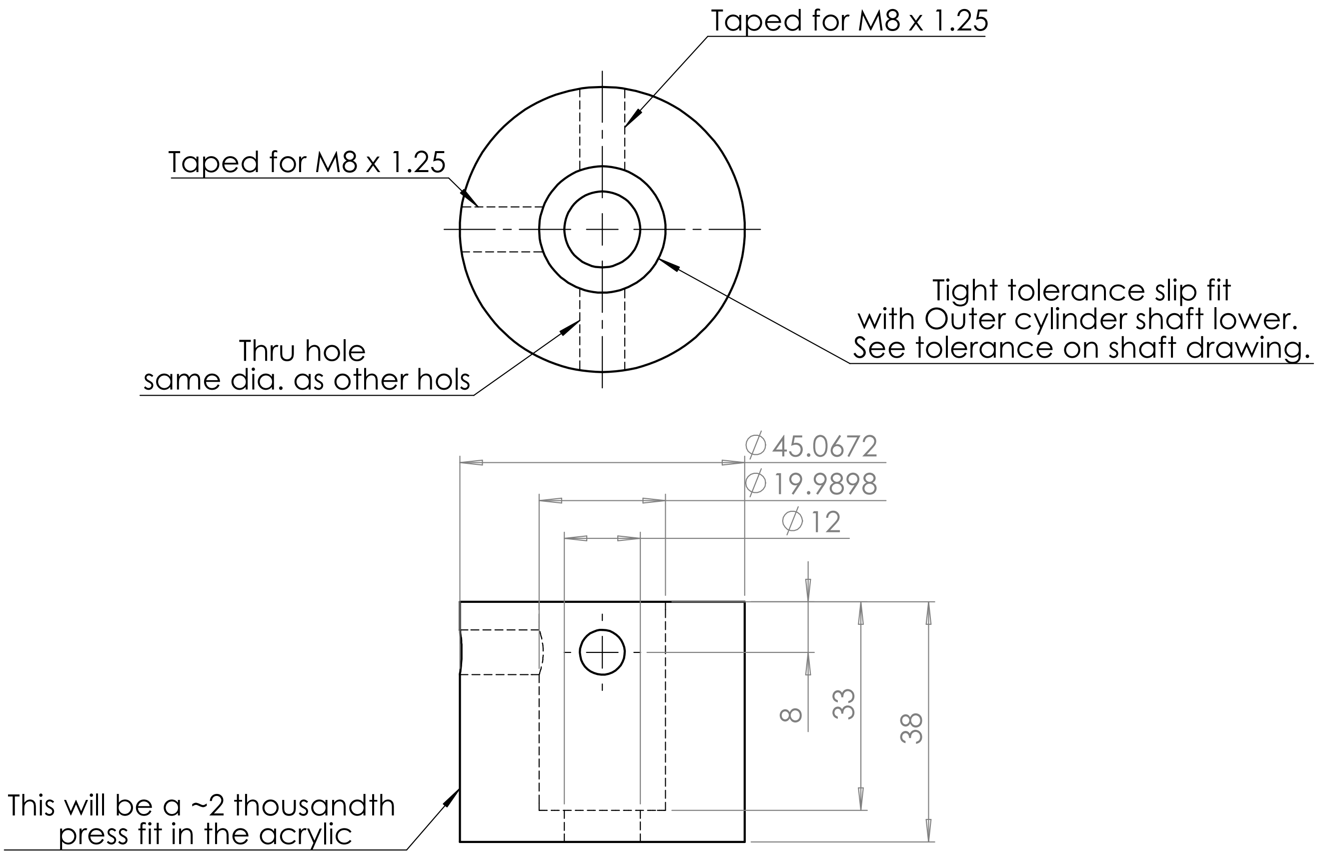

Part name:	Outer cylinder shaft sleve
Material:	316 Stainless Steel
Units:	mm
Designer:	Chris Crowley

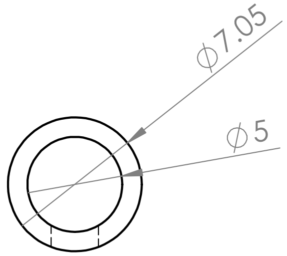

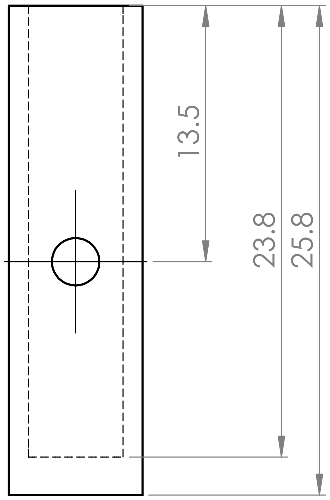

Part name:	Inner cylinder shaft sleve (for split shaft assembly)
Material:	Aluminum
Units:	mm
Designer:	Chris Crowley

D.4 Shaft mount assembly

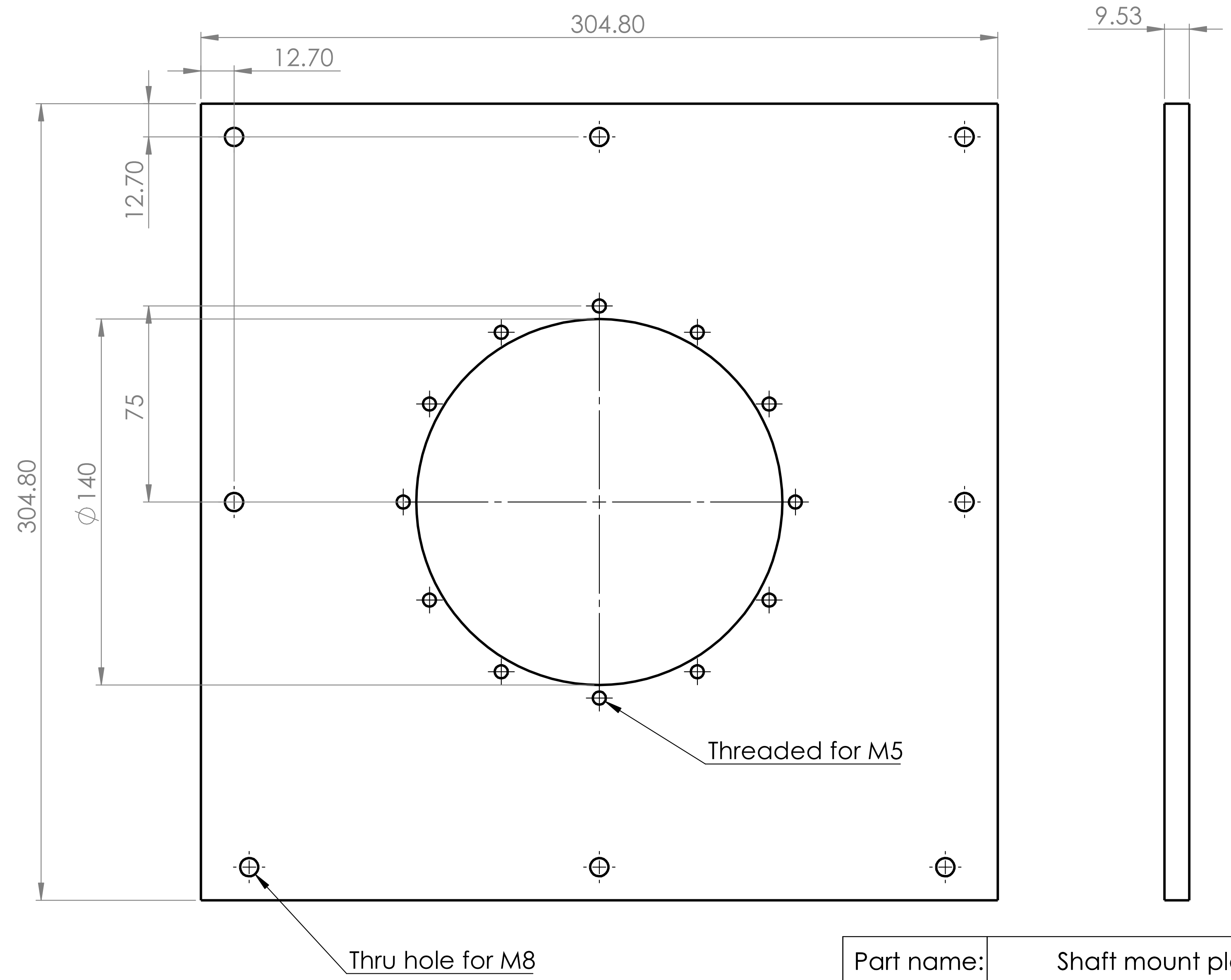

Part name:	Shaft mount plate
Material:	Aluminum
Units:	mm
Designer:	Chris Crowley

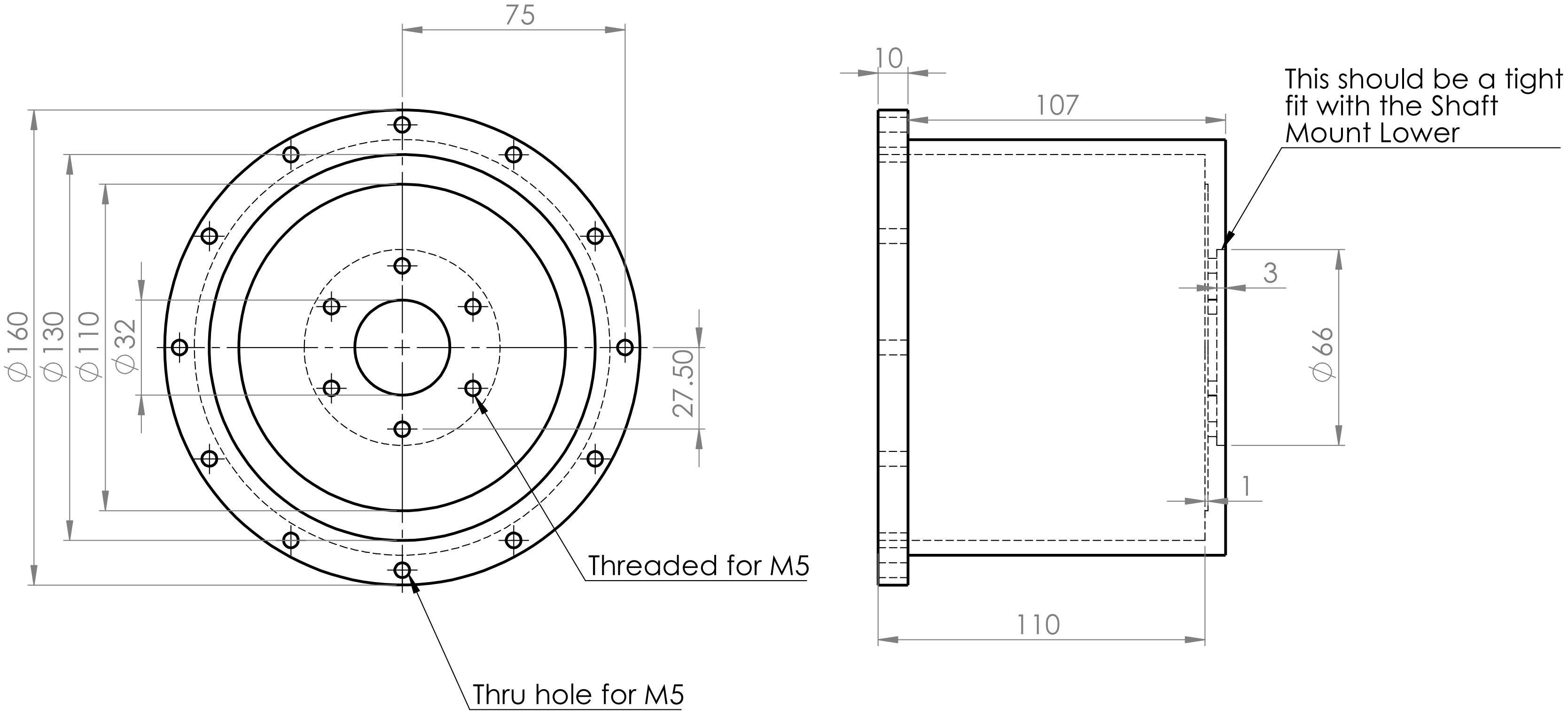

Part name:	Shaft mount upper
Material:	Aluminum
Units:	mm
Designer:	Chris Crowley

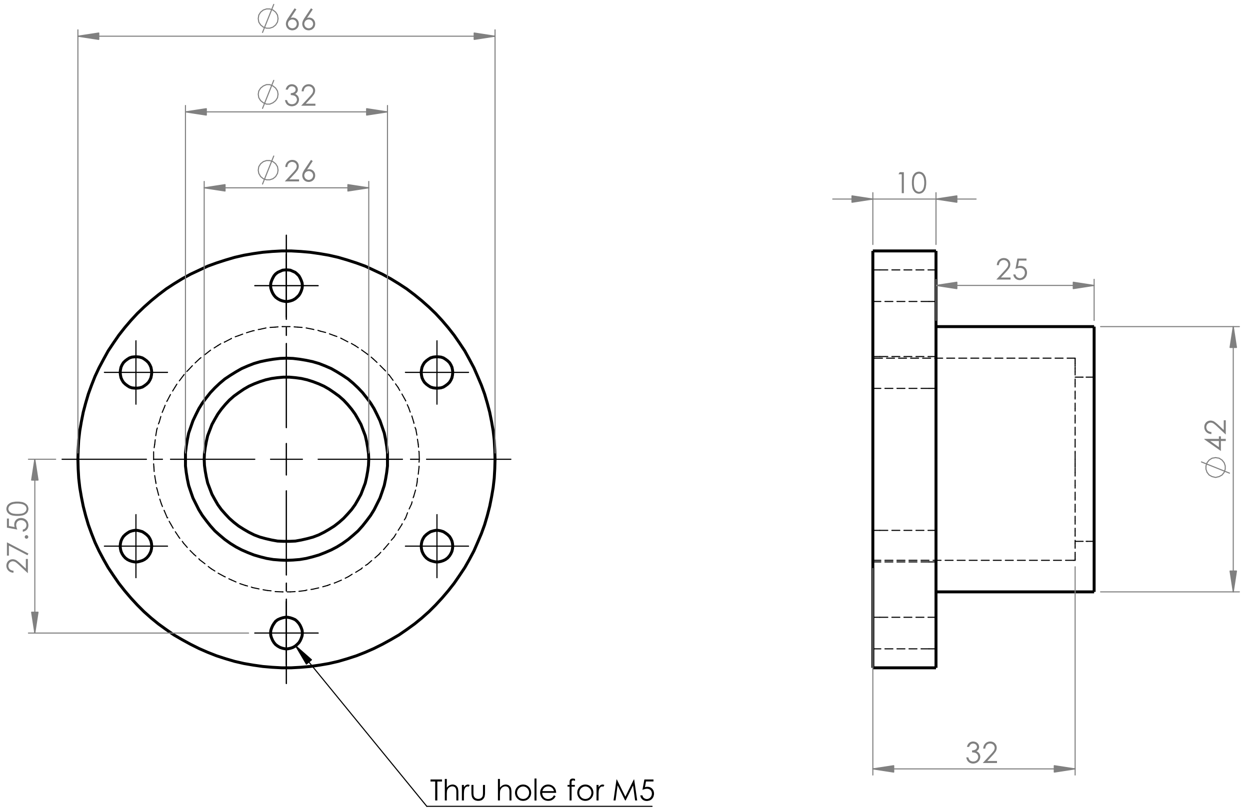

Part name:	Shaft mount lower
Material:	Aluminum
Units:	mm
Designer:	Chris Crowley

REFERENCES

[1] J. Lumley, “Some comments on turbulence,” *Physics of Fluids A: Fluid Dynamics*, vol. 4, no. 2, pp. 203–211, 1992.

[2] G. G. Stokes, “On the effect of the internal friction of fluids on the motion of pendulums,” in *Mathematical and Physical Papers*, ser. Cambridge Library Collection - Mathematics. Cambridge University Press, 2009, vol. 3, pp. 1–10.

[3] A. N. Kolmogorov, “The local structure of turbulence in incompressible viscous fluid for very large reynolds numbers,” *Cr. Acad. Sci. URSS*, vol. 30, pp. 301–305, 1941.

[4] G. I. Taylor, “Statistical theory of turbulence,” *Proceedings of the Royal Society of London. Series A-Mathematical and Physical Sciences*, vol. 151, no. 873, pp. 421–444, 1935.

[5] L. F. Moody, “Friction factors for pipe flow,” *Trans. Asme*, vol. 66, pp. 671–684, 1944.

[6] R. L. Panton, *Incompressible flow*. John Wiley & Sons, 2013.

[7] B. E. Launder, G. J. Reece, and W. Rodi, “Progress in the development of a Reynolds-stress turbulence closure,” *Journal of fluid mechanics*, vol. 68, no. 3, pp. 537–566, 1975.

[8] F. R. Hama, J. D. Long, and J. C. Hegarty, “On transition from laminar to turbulent flow,” *Journal of Applied Physics*, vol. 28, no. 4, pp. 388–394, 1957.

[9] A. F. Hussain, “Coherent structures-reality and myth,” *The Physics of fluids*, vol. 26, no. 10, pp. 2816–2850, 1983.

[10] W. Willmarth and B. J. Tu, “Structure of turbulence in the boundary layer near the wall,” *The Physics of Fluids*, vol. 10, no. 9, S134–S137, 1967.

[11] S. K. Robinson, “Coherent motions in the turbulent boundary layer,” *Annual Review of Fluid Mechanics*, vol. 23, no. 1, pp. 601–639, 1991.

[12] B. A. Singer and R. D. Joslin, “Metamorphosis of a hairpin vortex into a young turbulent spot,” *Physics of Fluids*, vol. 6, no. 11, pp. 3724–3736, 1994.

[13] D. Rockwell and E. Naudascher, “Self-sustained oscillations of impinging free shear layers,” *Annual Review of Fluid Mechanics*, vol. 11, no. 1, pp. 67–94, 1979.

[14] P. Cvitanović, R. Artuso, R. Mainieri, G. Tanner, and G. Vattay, *Chaos: Classical and Quantum*. Copenhagen: Niels Bohr Institute, 2016.

[15] J. Jiménez, "Coherent structures in wall-bounded turbulence," *Journal of Fluid Mechanics*, vol. 842, P1, 2018.

[16] F. Waleffe, "On a self-sustaining process in shear flows," *Physics of Fluids*, vol. 9, no. 4, pp. 883–900, 1997.

[17] ——, "Exact coherent structures in turbulent shear flows," in *Turbulence and Interactions*, M. Deville, T.-H. Lê, and P. Sagaut, Eds., Berlin, Heidelberg: Springer Berlin Heidelberg, 2009, pp. 139–158, ISBN: 978-3-642-00262-5.

[18] H. Faisst and B. Eckhardt, "Traveling waves in pipe flow," *Phys. Rev. Lett.*, vol. 91, p. 224 502, 22 Nov. 2003.

[19] M. Avila, F. Mellibovsky, N. Roland, and B. Hof, "Streamwise-localized solutions at the onset of turbulence in pipe flow," *Phyical Review Letters*, vol. 110, p. 224 502, 22 May 2013.

[20] K. Deguchi, A. Meseguer, and F. Mellibovsky, "Subcritical equilibria in Taylor-Couette flow," *Phys. Rev. Lett.*, vol. 112, p. 184 502, 18 May 2014.

[21] J. F. Gibson, J. Halcrow, and P. Cvitanović, "Equilibrium and travelling-wave solutions of plane Couette flow," *Journal of Fluid Mechanics*, vol. 638, pp. 243–266, 2009.

[22] T. M. Schneider, B. Eckhardt, and J. Vollmer, "Statistical analysis of coherent structures in transitional pipe flow," *Physical Review E*, vol. 75, no. 6, p. 066 313, 2007.

[23] E. Hopf, "Abzweigung einer periodischen lösung von einer stationären lösung eines differentialsystems," *Ber. Math.-Phys. Kl Sächs. Akad. Wiss. Leipzig*, vol. 94, pp. 1–22, 1942.

[24] H. Poincaré, *Les Méthodes Nouvelles de la Mécanique Céleste*. Gauthier-Villars, 1899, vol. 3.

[25] C. J. Crowley, M. C. Krygier, D. Borrero-Echeverry, R. O. Grigoriev, and M. F. Schatz, "A novel subcritical transition to turbulence in Taylor-Couette flow with counter-rotating cylinders," *Journal of Fluid Mechanics*, vol. 892, A12, 2020.

[26] H. Goldstein, C. Poole, and J. Safko, *Classical mechanics*, 2002.

[27] L. Landau and E. Lifshitz, “Chapter i - the equations of motion,” in *Mechanics (Third Edition)*, L. Landau and E. Lifshitz, Eds., Third Edition, Oxford: Butterworth-Heinemann, 1976, pp. 1–12, ISBN: 978-0-7506-2896-9.

[28] H. Poincaré, *New Methods of Celestial Mechanics*, 1st ed., ser. 13. Melville, NY: AIP-Press, 1992, ISBN: 978-1-56396-117-5.

[29] “Brief history of chaos,” in *Chaos: Classical and Quantum*, P. Cvitanović, R. Artuso, R. Mainieri, G. Tanner, and G. Vattay, Eds., 16th ed., Niels Bohr Institute, 2012, ch. A1.

[30] G. D. Birkhoff, *Dynamical systems*. American Mathematical Soc., 1927, vol. 9.

[31] S. Wiggins, S. Wiggins, and M. Golubitsky, *Introduction to applied nonlinear dynamical systems and chaos*, 3. Springer, 2003, vol. 2, ch. 1.

[32] ——, *Introduction to applied nonlinear dynamical systems and chaos*, 3. Springer, 2003, vol. 2, ch. 3.

[33] N. Bacaër, “Lotka, volterra and the predator–prey system (1920–1926),” in *A short history of mathematical population dynamics*, Springer, 2011, pp. 71–76.

[34] E. N. Lorenz and K. Haman, “The essence of chaos,” *Pure and Applied Geophysics*, vol. 147, no. 3, pp. 598–599, 1996.

[35] D. Richards, “Is strategic decision making chaotic?” *Behavioral Science*, vol. 35, no. 3, pp. 219–232, 1990.

[36] D. Ruelle and F. Takens, “On the nature of turbulence,” *Les rencontres physiciens-mathématiciens de Strasbourg-RCP25*, vol. 12, pp. 1–44, 1971.

[37] S. Smale, “Differentiable dynamical systems,” *Bulletin of the American mathematical Society*, vol. 73, no. 6, pp. 747–817, 1967.

[38] M. Viana, “What’s new on lorenz strange attractors?” *The Mathematical Intelligencer*, vol. 22, no. 3, pp. 6–19, 2000.

[39] W. Tucker, “The lorenz attractor exists,” *Comptes Rendus de l’Académie des Sciences-Series I-Mathematics*, vol. 328, no. 12, pp. 1197–1202, 1999.

[40] ——, “A rigorous ode solver and smale’s 14th problem,” *Foundations of Computational Mathematics*, vol. 2, no. 1, pp. 53–117, 2002.

[41] R. Artuso, E. Aurell, and P. Cvitanovic, “Recycling of strange sets: I. Cycle expansions,” *Nonlinearity*, vol. 3, no. 2, p. 325, 1990.

[42] D. Viswanath, "Symbolic dynamics and periodic orbits of the lorenz attractor," *Nonlinearity*, vol. 16, no. 3, p. 1035, 2003.

[43] G. Yalnız and N. B. Budanur, "Inferring symbolic dynamics of chaotic flows from persistence," *Chaos: An Interdisciplinary Journal of Nonlinear Science*, vol. 30, no. 3, p. 033 109, 2020.

[44] B. Suri, L. Kageorge, R. O. Grigoriev, and M. F. Schatz, "Capturing turbulent dynamics and statistics in experiments with unstable periodic orbits," *Phys. Rev. Lett.*, vol. 125, p. 064 501, 6 Aug. 2020.

[45] N. B. Budanur, K. Y. Short, M. Farazmand, A. P. Willis, and P. Cvitanović, "Relative periodic orbits form the backbone of turbulent pipe flow," *Journal of Fluid Mechanics*, vol. 833, pp. 274–301, 2017.

[46] L. Rayleigh, "On the dynamics of revolving fluids," *Proceedings of the Royal Society of London. Series A, Containing Papers of a Mathematical and Physical Character*, vol. 93, no. 648, pp. 148–154, 1917.

[47] S. Chandrasekhar, *Hydrodynamic and hydromagnetic stability*. Courier Corporation, 2013.

[48] G. I. Taylor, "Stability of a viscous liquid contained between two rotating cylinders," *Philosophical Transactions of the Royal Society of London. Series A, Containing Papers of a Mathematical or Physical Character*, vol. 223, p. 289, 1923.

[49] F. Schultz-Grunow and H. Hein, "Beitrag zur couettestromung," *Z. Flugwiss*, vol. 4, pp. 28–30, 1956.

[50] C. D. Andereck, S. S. Liu, and H. L. Swinney, "Flow regimes in a circular Couette system with independently rotating cylinders," *Journal of Fluid Mechanics*, vol. 164, p. 155, Apr. 1986.

[51] D. Borrero-Echeverry, C. J. Crowley, and T. P. Riddick, "Rheoscopic fluids in a post-Kalliroscope world," *Physics of Fluids*, vol. 30, p. 087 103, 2018.

[52] J. P. Gollub and H. L. Swinney, "Onset of turbulence in a rotating fluid," *Physical Review Letters*, vol. 35, no. 14, p. 927, 1975.

[53] P. W. Colovas and C. D. Andereck, "Turbulent bursting and spatiotemporal intermittency in the counterrotating Taylor-Couette system," *Physical Review E*, vol. 55, p. 2736, 3 Mar. 1997.

[54] A. Meseguer, F. Mellibovsky, M. Avila, and F. Marques, “Instability mechanisms and transition scenarios of spiral turbulence in Taylor-Couette flow,” *Physical Review E*, vol. 80, p. 046 315, 4 2009.

[55] S. G. Huisman, R. C. Van Der Veen, C. Sun, and D. Lohse, “Multiple states in highly turbulent Taylor–Couette flow,” *Nature communications*, vol. 5, no. 1, pp. 1–5, 2014.

[56] D. P. Van Gils, S. G. Huisman, G.-W. Bruggert, C. Sun, and D. Lohse, “Torque scaling in turbulent Taylor-Couette flow with co-and counterrotating cylinders,” *Physical review letters*, vol. 106, no. 2, p. 024 502, 2011.

[57] S. Grossmann, D. Lohse, and C. Sun, “High–Reynolds number Taylor-Couette turbulence,” *Annual review of fluid mechanics*, vol. 48, pp. 53–80, 2016.

[58] D. Coles, “Transition in circular Couette flow,” *Journal of Fluid Mechanics*, vol. 21, p. 385, 1965.

[59] A. Prigent and O. Dauchot, “Transition to versus from turbulence in subcritical Couette flows,” in *IUTAM Symposium on Laminar-Turbulent Transition and Finite Amplitude Solutions*, T. Mullin and R. Kerswell, Eds., Dordrecht: Springer Netherlands, 2005, p. 195, ISBN: 978-1-4020-4049-8.

[60] D. Borrero-Echeverry, M. F. Schatz, and R. Tagg, “Transient turbulence in Taylor-Couette flow,” *Physical Review E*, vol. 81, 025301(R), 2 Feb. 2010.

[61] T. B. Benjamin, “Bifurcation phenomena in steady flows of a viscous fluid ii. experiments,” *Proceedings of the Royal Society of London. A. Mathematical and Physical Sciences*, vol. 359, no. 1696, pp. 27–43, 1978.

[62] K. Cliffe, “Numerical calculations of two-cell and single-cell Taylor flows,” *Journal of Fluid Mechanics*, vol. 135, pp. 219–233, 1983.

[63] M. Lücke, M. Mihelcic, K. Wingerath, and G. Pfister, “Flow in a small annulus between concentric cylinders,” *Journal of Fluid Mechanics*, vol. 140, pp. 343–353, 1984.

[64] G. Pfister, H. Schmidt, K. A. Cliffe, and T. Mullin, “Bifurcation phenomena in Taylor-Couette flow in a very short annulus,” *Journal of Fluid Mechanics*, vol. 191, p. 1, 1988.

[65] A. Aitta, “Dynamics near a tricritical point in Couette-Taylor flow,” *Physical review letters*, vol. 62, no. 18, p. 2116, 1989.

[66] I. Nakamura and Y. Toya, “Existence of extra vortex and twin vortex of anomalous mode in Taylor vortex flow with a small aspect ratio,” *Acta mechanica*, vol. 117, no. 1, pp. 33–46, 1996.

[67] T. Mullin, Y. Toya, and S. Tavener, “Symmetry breaking and multiplicity of states in small aspect ratio Taylor–Couette flow,” *Physics of Fluids*, vol. 14, no. 8, pp. 2778–2787, 2002.

[68] H. Furukawa, T. Watanabe, Y. Toya, and I. Nakamura, “Flow pattern exchange in the Taylor-Couette system with a very small aspect ratio,” *Physical Review E*, vol. 65, no. 3, p. 036 306, 2002.

[69] F. Marques and J. Lopez, “Onset of three-dimensional unsteady states in small-aspect-ratio Taylor–Couette flow,” *Journal of Fluid Mechanics*, vol. 561, pp. 255–277, 2006.

[70] A. Schulz, G. Pfister, and S. Tavener, “The effect of outer cylinder rotation on Taylor–Couette flow at small aspect ratio,” *Physics of Fluids*, vol. 15, no. 2, pp. 417–425, 2003.

[71] C. F. Hamill, “Turbulent bursting in the Couette-Taylor system,” M.S. thesis, University of Texas at Austin, 1995.

[72] C. Crowley, I. I. Shinder, and M. R. Moldover, “The effect of turbulence on a multi-hole pitot calibration,” *Flow Measurement and Instrumentation*, vol. 33, pp. 106–109, 2013.

[73] B. K. Horn and B. G. Schunck, “Determining optical flow,” *Artificial intelligence*, vol. 17, no. 1-3, pp. 185–203, 1981.

[74] C. Liu, A. Torralba, W. T. Freeman, F. Durand, and E. H. Adelson, “Motion magnification,” *ACM transactions on graphics (TOG)*, vol. 24, no. 3, pp. 519–526, 2005.

[75] A. A. Adamczyk and L. Rimai, “2-dimensional particle tracking velocimetry (ptv): Technique and image processing algorithms,” *Experiments in Fluids*, vol. 6, no. 6, pp. 373–380, Jan. 1988.

[76] C. E. Willert and M. Gharib, “Digital particle image velocimetry,” *Experiments in fluids*, vol. 10, no. 4, pp. 181–193, 1991.

[77] M. Raffel, C. E. Willert, F. Scarano, C. J. Kähler, S. T. Wereley, and J. Kompenhans, *Particle image velocimetry: a practical guide*. Springer, 2018.

[78] L. Adrian, R. J. Adrian, and J. Westerweel, *Particle image velocimetry*, 30. Cambridge university press, 2011.

[79] J. Estevadeordal, C. Marks, R. Sondergaard, and M. Wolff, "Curved laser-sheet for conformal surface flow diagnostics," *Experiments in fluids*, vol. 50, no. 3, pp. 761–768, 2011.

[80] G. T. Herman and A. Lent, "Iterative reconstruction algorithms," *Computers in Biology and Medicine*, vol. 6, no. 4, pp. 273–294, 1976, Advances in Picture Reconstruction;Theory and Applications.

[81] B. Wieneke, "Iterative reconstruction of volumetric particle distribution," *Measurement Science and Technology*, vol. 24, no. 2, p. 024 008, Dec. 2012.

[82] G. E. Elsinga, F. Scarano, B. Wieneke, and B. W. van Oudheusden, "Tomographic particle image velocimetry," *Experiments in Fluids*, vol. 41, p. 933, 2006.

[83] G. E. Elsinga, B. Wieneke, F. Scarano, and A. Schröder, "Tomographic 3d-piv and applications," in *Particle Image Velocimetry: New Developments and Recent Applications*. Berlin, Heidelberg: Springer Berlin Heidelberg, 2008, pp. 103–125, ISBN: 978-3-540-73528-1.

[84] S. Discetti and T. Astarita, "Fast 3d piv with direct sparse cross-correlations," *Experiments in fluids*, vol. 53, no. 5, pp. 1437–1451, 2012.

[85] M. Novara, A. Ianiro, and F. Scarano, "Adaptive interrogation for 3d-PIV," *Measurement Science and Technology*, vol. 24, no. 2, p. 024 012, Dec. 2012.

[86] R. J. Donnelly, "Taylor–Couette flow: The early days," *Phys. Today*, vol. 44, no. 11, pp. 32–39, 1991.

[87] D. P. M. van Gils, G.-W. Bruggert, D. P. Lathrop, C. Sun, and D. Lohse, "The Twente turbulent Taylor-Couette (T3C) facility: Strongly turbulent (multiphase) flow between two independently rotating cylinders," *Review of Scientific Instruments*, vol. 82, no. 2, p. 025 105, 2011. eprint: https://doi.org/10.1063/1.3548924.

[88] S. G. Huisman, R. C. A. van der Veen, G.-W. H. Bruggert, D. Lohse, and C. Sun, "The boiling Twente Taylor-Couette (BTTC) facility: Temperature controlled turbulent flow between independently rotating, coaxial cylinders," *Review of Scientific Instruments*, vol. 86, no. 6, p. 065 108, 2015. eprint: https://doi.org/10.1063/1.4923082.

[89] D. Borrero-Echeverry, "Subcritical transition to turbulence in Taylor-Couette flow," Ph.D. dissertation, Georgia Institute of Technology, 2014.

[90] H. Ji, M. Burin, E. Schartman, and J. Goodman, "Hydrodynamic turbulence cannot transport angular momentum effectively in astrophysical disks," *Nature*, vol. 444, p. 343, 2006.

[91] G. Elsinga, J. Westerweel, F. Scarano, and M. Novara, “On the velocity of ghost particles and the bias errors in tomographic-piv,” *Experiments in fluids*, vol. 50, no. 4, pp. 825–838, 2011.

[92] F. Scarano and C. Poelma, “Three-dimensional vorticity patterns of cylinder wakes,” *Experiments in Fluids*, vol. 47, no. 1, pp. 69–83, 2009.

[93] D. Schanz, S. Gesemann, and A. Schröder, “Shake-the-box: Lagrangian particle tracking at high particle image densities,” *Experiments in Fluids*, vol. 57, no. 5, p. 70, Apr. 2016.

[94] S. Wiederseiner, N. Andreini, G. Epely-Chauvin, and C. Ancey, “Refractive-index and density matching in concentrated particle suspensions: A review,” *Experiments in fluids*, vol. 50, no. 5, pp. 1183–1206, 2011.

[95] J. Ostriker, “Viscous drag on an accretion disk due to an embedded stellar system,” *The Astrophysical Journal*, vol. 273, pp. 99–104, 1983.

[96] N. I. Shakura and R. A. Sunyaev, “Black holes in binary systems. observational appearance.,” *Astronomy and Astrophysics*, vol. 24, pp. 337–355, 1973.

[97] E. Palmén and H. Riehl, “Budget of angular momentum and energy in tropical cyclones,” *Journal of the Atmospheric Sciences*, vol. 14, no. 2, pp. 150–159, 1957.

[98] M. M. Couette, “Etudes sur le frottement des liquides,” *Annales de Chimie et de Physique*, vol. 20, p. 433, 1890.

[99] A. Mallock, “Experiments on fluid viscosity,” *Philosophical Transactions of the Royal Society A: Mathematical, Physical and Engineering Sciences*, vol. 1897, p. 41, 1896.

[100] M. Burin, E. Schartman, and H. Ji, “Local measurements of turbulent angular momentum transport in circular couette flow,” *Experiments in fluids*, vol. 48, no. 5, pp. 763–769, 2010.

[101] M. S. Paoletti and D. P. Lathrop, “Angular momentum transport in turbulent flow between independently rotating cylinders,” *Physical Review Letters*, vol. 106, p. 024 501, 2011.

[102] R. Ezeta, F. Sacco, D. Bakhuis, S. G. Huisman, R. Ostilla-Mónico, R. Verzicco, C. Sun, and D. Lohse, “Double maxima of angular momentum transport in small gap Taylor–Couette turbulence,” *Journal of fluid mechanics*, vol. 900, 2020.

[103] H. Wu, H. Xu, and E. Bodenschatz, "Measuring vorticity vector from the spinning of micro-sized mirror-encapsulated spherical particles in the flow," *Review of Scientific Instruments*, vol. 90, no. 11, p. 115 111, 2019.

[104] J. Hong, L. Feng, C. Panigrahi, R. Grazzini, *et al.*, "Direct measurement of vorticity using tracer particles with internal markers," in *APS Division of Fluid Dynamics Meeting Abstracts*, 2021, E20–005.

[105] S. G. Huisman, S. Scharnowski, C. Cierpka, C. J. Kähler, D. Lohse, and C. Sun, "Logarithmic boundary layers in strong Taylor-Couette turbulence," *Physical review letters*, vol. 110, no. 26, p. 264 501, 2013.

[106] M. Raffel, C. E. Willert, S. T. Wereley, and J. Kompenhans, "Image evaluation methods for piv," in *Particle Image Velocimetry*, Springer, 2007, pp. 123–176.

[107] A. Zangwill, *Modern electrodynamics*. Cambridge University Press, 2013.

[108] J. D. Jackson, *Classical electrodynamics*, 1999.

[109] A. Melling, "Tracer particles and seeding for particle image velocimetry," *Measurement science and technology*, vol. 8, no. 12, p. 1406, 1997.

[110] J. B. Will and D. Krug, "Rising and sinking in resonance: Mass distribution critically affects buoyancy-driven spheres via rotational dynamics," *Physical review letters*, vol. 126, no. 17, p. 174 502, 2021.

[111] M. Lyon and L. Leal, "An experimental study of the motion of concentrated suspensions in two-dimensional channel flow. part 1. monodisperse systems," *Journal of Fluid Mechanics*, vol. 363, pp. 25–56, 1998.

[112] D. Schwabe, A. Mizev, M. Udhayasankar, and S. Tanaka, "Formation of dynamic particle accumulation structures in oscillatory thermocapillary flow in liquid bridges," *Physics of Fluids*, vol. 19, no. 7, p. 072 102, 2007.

[113] T. Sakata, S. Terasaki, H. Saito, S. Fujimoto, I. Ueno, T. Yano, K. Nishino, Y. Kamotani, and S. Matsumoto, "Coherent structures of m= 1 by low-stokes-number particles suspended in a half-zone liquid bridge of high aspect ratio: Microgravity and terrestrial experiments," *Physical Review Fluids*, vol. 7, no. 1, p. 014 005, 2022.

[114] T.-S. Yang and S. S. Shy, "The preferential accumulation and the settling velocity of small heavy particles in Taylor–Couette flows," *Journal of Mechanics*, vol. 37, pp. 651–658, 2021.

[115] R. Mei, "Velocity fidelity of flow tracer particles," *Experiments in fluids*, vol. 22, no. 1, pp. 1–13, 1996.

[116] A. Kurian, N. A. George, B. Paul, V. Nampoori, and C. Vallabhan, “Studies on fluorescence efficiency and photodegradation of rhodamine 6g doped pmma using a dual beam thermal lens technique,” *Laser Chemistry*, vol. 20, no. 2-4, pp. 99–110, 2002.

[117] M. Fikry, M. Omar, and L. Z. Ismail, “Effect of host medium on the fluorescence emission intensity of rhodamine b in liquid and solid phase,” in *Modern Trends in Physics Research*, World Scientific, 2011, pp. 210–219.

[118] F. Pedocchi, J. E. Martin, and M. H. García, “Inexpensive fluorescent particles for large-scale experiments using particle image velocimetry,” *Experiments in Fluids*, vol. 45, no. 1, pp. 183–186, 2008.

[119] I. Uzelac, C. J. Crowley, S. Iravanian, T. Y. Kim, H. C. Cho, and F. H. Fenton, “Methodology for cross-talk elimination in simultaneous voltage and calcium optical mapping measurements with semasbestic wavelengths,” *Frontiers in physiology*, p. 3, 2022.

[120] H. Du, R.-C. A. Fuh, J. Li, L. A. Corkan, and J. S. Lindsey, “Photochemcad: A computer-aided design and research tool in photochemistry,” *Photochemistry and photobiology*, vol. 68, no. 2, pp. 141–142, 1998.

[121] “Photochemcad 2: A refined program with accompanying spectral databases for photochemical calculations¶,”

[122] R. Ahmed and M. Saif, “Optical properties of rhodamine b dye doped in transparent polymers for sensor application,” *chinese journal of physics*, vol. 51, no. 3, pp. 511–521, 2013.

[123] D. D. Cooke and M. Kerker, “Light scattering from long thin glass cylinders at oblique incidence,” *JOSA*, vol. 59, no. 1, pp. 43–48, 1969.

[124] H. Nobach and E. Bodenschatz, “Limitations of accuracy in piv due to individual variations of particle image intensities,” *Experiments in fluids*, vol. 47, no. 1, pp. 27–38, 2009.

[125] Michaelis, Dirk, *Product-manual for davis: Flowmaster shake-the-box (4d ptv)*, LaVision GmbH, Göttingen, Germany, 2016.

[126] W. Drotning and E. Roth, “Effects of moisture on the thermal expansion of poly (methylmethacrylate),” *Journal of materials science*, vol. 24, no. 9, pp. 3137–3140, 1989.

[127] D. Borrero-Echeverry and B. C. A. Morrison, "Aqueous ammonium thiocyanate solutions as refractive index-matching fluids with low density and viscosity," *Experiments in Fluids*, vol. 57, p. 123, 2016.

[128] B. Bailey and M. Yoda, "An aqueous low-viscosity density-and refractive index-matched suspension system," *Experiments in fluids*, vol. 35, no. 1, pp. 1–3, 2003.

[129] J.-M. Cariou, J. Dugas, L. Martin, and P. Michel, "Refractive-index variations with temperature of pmma and polycarbonate," *Applied optics*, vol. 25, no. 3, pp. 334–336, 1986.

[130] F. L. Arbeloa, P. R. Ojeda, and I. L. Arbeloa, "Flourescence self-quenching of the molecular forms of rhodamine b in aqueous and ethanolic solutions," *Journal of luminescence*, vol. 44, no. 1-2, pp. 105–112, 1989.

[131] R. M. Waxler, D. Horowitz, and A. Feldman, "Optical and physical parameters of plexiglas 55 and lexan," *Applied Optics*, vol. 18, no. 1, pp. 101–104, 1979.

[132] S. N. Kasarova, N. G. Sultanova, and I. D. Nikolov, "Temperature dependence of refractive characteristics of optical plastics," in *Journal of Physics-Conference Series*, vol. 253, 2010, p. 012 028.

[133] I. Thormählen, J. Straub, and U. Grigull, "Refractive index of water and its dependence on wavelength, temperature, and density," *Journal of Physical and Chemical Reference Data*, vol. 14, no. 4, pp. 933–945, 1985. eprint: https://doi.org/10.1063/1.555743.

[134] L. Ravald, J. Chilver, and R. Williams, "The corrosion of mild steel by aqueous ammonium thiocyanate," *Journal of Applied Chemistry*, vol. 7, no. 3, pp. 113–117, 1957.

[135] P. Degiampietro, E. Peheim, D. Drew, H. Graf, and J. Colombo, "Determination of thiocyanate in plasma and saliva without deproteinisation and its validation as a smoking parameter," 1987.

[136] J. Sommeria, S. D. Meyers, and H. L. Swinney, "Experiments on vortices and Rossby waves in eastward and westward jets," in *Nonlinear Topics in Ocean Physics*, A. Osborne, Ed., ser. Enrico Fermi International School of Physics, vol. 109, Amsterdam: North-Holland, 1991, p. 227.

[137] K. Bai and J. Katz, "On the refractive index of sodium iodide solutions for index matching in piv," *Experiments in fluids*, vol. 55, no. 4, pp. 1–6, 2014.

[138] F. L. Pedrotti, L. M. Pedrotti, and L. S. Pedrotti, *Introduction to optics*. Cambridge University Press, 2017.

[139] D. Fries, “Entrainment, mixing, and ignition in single and multiple jets in a supersonic crossflow,” Ph.D. dissertation, Georgia Institute of Technology, 2020.

[140] A. E. Siegman, *Lasers*. University science books, 1986.

[141] O. Gal, *Fit_ellipse*, https://www.mathworks.com/matlabcentral/fileexchange/3215-fit_ellipse, [MATLAB Central File Exchange. Retrieved September 8, 2021], 2003.

[142] F. Scarano, “Iterative image deformation methods in piv,” *Measurement science and technology*, vol. 13, no. 1, R1, 2001.

[143] H. W. Coleman and W. G. Steele, *Experimentation, validation, and uncertainty analysis for engineers*. John Wiley & Sons, 2018.

[144] B. N. Taylor, C. E. Kuyatt, *et al.*, *Guidelines for evaluating and expressing the uncertainty of NIST measurement results*. US Department of Commerce, Technology Administration, National Institute of . . ., 1994, vol. 1297.

[145] J. Jcgm *et al.*, “Evaluation of measurement data—guide to the expression of uncertainty in measurement,” *Int. Organ. Stand. Geneva ISBN*, vol. 50, p. 134, 2008.

[146] W. A. Fuller, *Measurement error models*. John Wiley & Sons, 1987.

[147] J. H. McLeod, “The axicon: A new type of optical element,” *JOSA*, vol. 44, no. 8, pp. 592–597, 1954.

[148] Z. Jaroszewicz, “Axicons: Design and propagation properties,” in *Research & Development Treatises*, M. Pluta, Ed., Warsaw, Poland: Institute of Applied Optics, 1997.

[149] *Model dm dual head laser installation and operation manual*, Photonics Industries, Ronkonkoma, NY, 2015.

[150] M. E. Davison, “The ill-conditioned nature of the limited angle tomography problem,” *SIAM Journal on Applied Mathematics*, vol. 43, no. 2, pp. 428–448, 1983.

[151] H. G. Maas, A. Gruen, and D. Papantoniou, “Particle tracking velocimetry in three-dimensional flows,” *Experiments in Fluids*, vol. 15, no. 2, pp. 133–146, Jul. 1993.

[152] B. Wieneke, “Stereo-piv using self-calibration on particle images,” *Experiments in fluids*, vol. 39, no. 2, pp. 267–280, 2005.

[153] Y. Abdel-Aziz and H. Karara, “Direct linear transformation into object space coordinates in close-range photogrammetry,” in *Proc. Symp. Close-Range Photogrammetry*, 1971, pp. 1–18.

[154] Y. Yakimovsky and R. Cunningham, “A system for extracting three-dimensional measurements from a stereo pair of tv cameras,” *Computer graphics and image processing*, vol. 7, no. 2, pp. 195–210, 1978.

[155] R. Tsai, “A versatile camera calibration technique for high-accuracy 3d machine vision metrology using off-the-shelf tv cameras and lenses,” *IEEE Journal on Robotics and Automation*, vol. 3, no. 4, pp. 323–344, 1987.

[156] A. K. Prasad, “Stereoscopic particle image velocimetry,” *Experiments in fluids*, vol. 29, no. 2, pp. 103–116, 2000.

[157] C. Willert, “Stereoscopic digital particle image velocimetry for application in wind tunnel flows,” *Measurement science and technology*, vol. 8, no. 12, p. 1465, 1997.

[158] F. Chen, X. Chen, X. Xie, X. Feng, and L. Yang, “Full-field 3d measurement using multi-camera digital image correlation system,” *Optics and Lasers in Engineering*, vol. 51, no. 9, pp. 1044–1052, 2013.

[159] S. M. Soloff, R. J. Adrian, and Z.-C. Liu, “Distortion compensation for generalized stereoscopic particle image velocimetry,” *Measurement science and technology*, vol. 8, no. 12, p. 1441, 1997.

[160] F. Pedersini, A. Sarti, and S. Tubaro, “Accurate and simple geometric calibration of multi-camera systems,” *Signal Processing*, vol. 77, no. 3, pp. 309–334, 1999.

[161] ——, “Multi-camera systems,” *IEEE Signal Processing Magazine*, vol. 16, no. 3, pp. 55–65, 1999.

[162] F. Scarano, L. David, M. Bsibsi, and D. Calluaud, “S-piv comparative assessment: Image dewarping+misalignment correction and pinhole+geometric back projection,” *Experiments in fluids*, vol. 39, no. 2, pp. 257–266, 2005.

[163] B. Wieneke, “Volume self-calibration for 3d particle image velocimetry,” *Experiments in fluids*, vol. 45, no. 4, pp. 549–556, 2008.

[164] ——, “Improvements for volume self-calibration,” *Measurement Science and Technology*, vol. 29, no. 8, p. 084 002, 2018.

[165] J. Westerweel, “Efficient detection of spurious vectors in particle image velocimetry data,” *Experiments in fluids*, vol. 16, no. 3, pp. 236–247, 1994.

[166] J. Nogueira, A. Lecuona, and P. Rodriguez, “Data validation, false vectors correction and derived magnitudes calculation on piv data,” *Measurement Science and Technology*, vol. 8, no. 12, p. 1493, 1997.

[167] J. Westerweel and F. Scarano, “Universal outlier detection for piv data,” *Experiments in fluids*, vol. 39, no. 6, pp. 1096–1100, 2005.

[168] E. Saredi, A. Sciacchitano, and F. Scarano, “Outlier detection for piv statistics based on turbulence transport,” *Experiments in Fluids*, vol. 63, no. 1, pp. 1–10, 2022.

[169] J. Duncan, D. Dabiri, J. Hove, and M. Gharib, “Universal outlier detection for particle image velocimetry (piv) and particle tracking velocimetry (ptv) data,” *Measurement Science and Technology*, vol. 21, no. 5, p. 057 002, 2010.

[170] C. J. Kähler, T. Astarita, P. P. Vlachos, J. Sakakibara, R. Hain, S. Discetti, R. La Foy, and C. Cierpka, “Main results of the 4th international piv challenge,” *Experiments in Fluids*, vol. 57, no. 6, pp. 1–71, 2016.

[171] P. Li, S. J. Eckels, G. W. Mann, and N. Zhang, “Experimental measurements in near-wall regions by particle image velocimetry (piv),” in *Fluids Engineering Division Summer Meeting*, American Society of Mechanical Engineers, vol. 46247, 2014, V01DT40A004.

[172] A. Sciacchitano, D. R. Neal, B. L. Smith, S. O. Warner, P. P. Vlachos, B. Wieneke, and F. Scarano, “Collaborative framework for piv uncertainty quantification: Comparative assessment of methods,” *Measurement Science and Technology*, vol. 26, no. 7, p. 074 004, 2015.

[173] B. H. Timmins, B. W. Wilson, B. L. Smith, and P. P. Vlachos, “A method for automatic estimation of instantaneous local uncertainty in particle image velocimetry measurements,” *Experiments in fluids*, vol. 53, no. 4, pp. 1133–1147, 2012.

[174] A. Sciacchitano, B. Wieneke, and F. Scarano, “Piv uncertainty quantification by image matching,” *Measurement Science and Technology*, vol. 24, no. 4, p. 045 302, 2013.

[175] J. J. Charonko and P. P. Vlachos, “Estimation of uncertainty bounds for individual particle image velocimetry measurements from cross-correlation peak ratio,” *Measurement Science and Technology*, vol. 24, no. 6, p. 065 301, 2013.

[176] B. Wieneke, “Piv uncertainty quantification from correlation statistics,” *Measurement Science and Technology*, vol. 26, no. 7, p. 074 002, 2015.

[177] A. Sciacchitano and B. Wieneke, “Piv uncertainty propagation,” *Measurement Science and Technology*, vol. 27, no. 8, p. 084 006, 2016.

[178] D. R. Neal, A. Sciacchitano, B. L. Smith, and F. Scarano, “Collaborative framework for piv uncertainty quantification: The experimental database,” *Measurement Science and Technology*, vol. 26, no. 7, p. 074 003, 2015.

[179] B. Wieneke, “Piv anisotropic denoising using uncertainty quantification,” *Experiments in Fluids*, vol. 58, no. 8, pp. 1–10, 2017.

[180] I. Amidror, “Scattered data interpolation methods for electronic imaging systems: A survey,” *Journal of electronic imaging*, vol. 11, no. 2, pp. 157–176, 2002.

[181] M. Avila, M. Grimes, J. M. Lopez, and F. Marques, “Global endwall effects on centrifugally stable flows,” *Physics of Fluids*, vol. 20, p. 104 104, 2008.

[182] I. Mercader, O. Batiste, and A. Alonso, “An efficient spectral code for incompressible flows in cylindrical geometries,” *Computers & Fluids*, vol. 39, p. 215, 2010.

[183] M. Avila, “Stability and angular-momentum transport of fluid flows between corotating cylinders,” *Physical Review Letters*, vol. 108, p. 124 501, 2012.

[184] A. Esser and S. Grossmann, “Analytic expression for Taylor-Couette stability boundary,” *Physics of Fluids*, vol. 8, p. 1814, 1996.

[185] S. Bottin and H. Chaté, “Statistical analysis of the transition to turbulence in plane Couette flow,” *The European Physical Journal B - Condensed Matter and Complex Systems*, vol. 6, p. 143, 1998.

[186] J. Peixinho and T. Mullin, “Decay of turbulence in pipe flow,” *Physical Review Letters*, vol. 96, p. 094 501, 2006.

[187] D. Moore and P. G. McCabe, *Introduction to the Practice of Statistics*, 3rd ed. W. H. Freeman, 1998, ISBN: 978-0716735021.

[188] L. P. Kadanoff and C. Tang, “Escape from strange repellers,” *Proceedings of the National Academy of Sciences*, vol. 81, p. 1276, 1984.

[189] H. Kantz and P. Grassberger, “Repellers, semi-attractors, and long-lived chaotic transients,” *Physica D: Nonlinear Phenomena*, vol. 17, p. 75, 1985.

[190] Y. Do and Y.-C. Lai, “Scaling laws for noise-induced superpersistent chaotic transients,” *Physical Review E*, vol. 71, p. 046 208, 4 2005.

[191] D. Coles, “A note on Taylor instability in circular Couette flow,” *Journal of Applied Mechanics*, vol. 34, p. 529, 1967.

[192] B. Eckhardt and D. Yao, “Local stability analysis along Lagrangian paths,” *Chaos, Solitons & Fractals*, vol. 5, p. 2073, 1995.

[193] A. Goharzadeh and I. Mutabazi, “Experimental characterization of intermittency regimes in the Couette-Taylor system,” *The European Physical Journal B - Condensed Matter and Complex Systems*, vol. 19, p. 157, 2001.

[194] K. Coughlin and P. S. Marcus, “Turbulent bursts in Couette-Taylor flow,” *Physical Review Letters*, vol. 77, p. 2214, 11 Sep. 1996.

[195] H. Faisst and B. Eckhardt, “Sensitive dependence on initial conditions in transition to turbulence in pipe flow,” *Journal of Fluid Mechanics*, vol. 504, p. 343, 2004.

[196] K. Avila, D. Moxey, A. de Lozar, M. Avila, D. Barkley, and B. Hof, “The onset of turbulence in pipe flow,” *Science*, vol. 333, p. 192, 2011.

[197] B. Hof, C. W. H. van Doorne, J. Westerweel, F. T. M. Nieuwstadt, H. Faisst, B. Eckhardt, H. Wedin, R. R. Kerswell, and F. Waleffe, “Experimental observation of nonlinear traveling waves in turbulent pipe flow,” *Science*, vol. 305, p. 1594, 2004.

[198] B. Suri, J. Tithof, R. O. Grigoriev, and M. F. Schatz, “Forecasting fluid flows using the geometry of turbulence,” *Physical Review Letters*, vol. 118, p. 114 501, 11 2017.

[199] P. Holmes, J. L. Lumley, G. Berkooz, and C. W. Rowley, *Turbulence, coherent structures, dynamical systems and symmetry*. Cambridge university press, 1945.

[200] D. Viswanath, “Recurrent motions within plane Couette turbulence,” *Journal of Fluid Mechanics*, vol. 580, pp. 339–358, 2007.

[201] B. Eckhardt and S. Zammert, “Small scale exact coherent structures at large reynolds numbers in plane couette flow,” *Nonlinearity*, vol. 31, no. 2, R66, 2018.

[202] A. de Lozar, F. Mellibovsky, M. Avila, and B. Hof, “Edge state in pipe flow experiments,” *Physical Review Letters*, vol. 108, no. 21, p. 214 502, 2012.

[203] G. Lemoult, K. Gumowski, J.-L. Aider, and J. E. Wesfreid, “Turbulent spots in channel flow: An experimental study,” *The European Physical Journal E*, vol. 37, no. 4, p. 25, 2014.

[204] J. S. Park and M. D. Graham, “Exact coherent states and connections to turbulent dynamics in minimal channel flow,” *Journal of Fluid Mechanics*, vol. 782, pp. 430–454, 2015.

[205] R. R. Kerswell and O. R. Tutty, “Recurrence of travelling waves in transitional pipe flow,” *Journal of Fluid Mechanics*, vol. 584, pp. 69–102, 2007.

[206] F. Mellibovsky, A. Meseguer, T. M. Schneider, and B. Eckhardt, “Transition in localized pipe flow turbulence,” *Physical Review Letters*, vol. 103, no. 5, p. 054 502, 2009.

[207] P. Cvitanović and J. Gibson, “Geometry of the turbulence in wall-bounded shear flows: Periodic orbits,” *Physica Scripta*, vol. 2010, no. T142, p. 014 007, 2010.

[208] G. Kawahara and S. Kida, “Periodic motion embedded in plane couette turbulence: Regeneration cycle and burst,” *Journal of Fluid Mechanics*, vol. 449, p. 291, 2001.

[209] M. C. Krygier, J. L. Pughe-Sanford, and R. O. Grigoriev, “Exact coherent structures and shadowing in turbulent Taylor–Couette flow,” *Journal of Fluid Mechanics*, vol. 923, A7, 2021.

[210] M. C. Krygier, “Exact coherent structures in turbulent small-aspect-ratio Taylor-Couette flow,” Ph.D. dissertation, Georgia Institute of Technology, 2019.

[211] G. J. Chandler and R. R. Kerswell, “Invariant recurrent solutions embedded in a turbulent two-dimensional kolmogorov flow,” *Journal of Fluid Mechanics*, vol. 722, pp. 554–595, 2013.

[212] Y. Kuramoto, “Diffusion-induced chaos in reaction systems,” *Progress of Theoretical Physics Supplement*, vol. 64, pp. 346–367, 1978.

[213] G. I. Sivashinsky, “Nonlinear analysis of hydrodynamic instability in laminar flames—i. derivation of basic equations,” *Acta astronautica*, vol. 4, no. 11, pp. 1177–1206, 1977.

[214] C. J. Crowley, J. P.-S. L., W. Toler, M. C. Krygier, R. O. Grigoriev, and M. F. Schatz, “Turbulence tracks recurrent solutions,” *Proceedings of the National Academy of Sciences*, 2022.

[215] Å. Fredriksen, C. Riccardi, L. Cartegni, and H. Pécseli, “Coherent structures, transport and intermittency in a magnetized plasma,” *Plasma Physics and Controlled Fusion*, vol. 45, no. 5, p. 721, 2003.

[216] P. Cvitanović, “Chaotic field theory: A sketch,” *Physica A*, vol. 288, p. 61, 2000.

[217] C. D. Marcotte and R. O. Grigoriev, “Unstable spiral waves and local euclidean symmetry in a model of cardiac tissue,” *Chaos: An Interdisciplinary Journal of Nonlinear Science*, vol. 25, no. 6, p. 063 116, 2015.

[218] S. Amari, “Dynamics of pattern formation in lateral-inhibition type neural fields,” *Biological Cybernetics*, vol. 27, no. 2, pp. 77–87, 1977.

[219] N. Sambelashvili, A. Lau, and D. Cai, "Dynamics of bacterial flow: Emergence of spatiotemporal coherent structures," *Physics Letters A*, vol. 360, no. 4-5, pp. 507–511, 2007.

[220] J.-M. Lavest, M. Viala, and M. Dhome, "Do we really need an accurate calibration pattern to achieve a reliable camera calibration?" In *European Conference on Computer Vision*, Springer, 1998, pp. 158–174.

[221] J. Zhang, J. Zhu, H. Deng, Z. Chai, M. Ma, and X. Zhong, "Multi-camera calibration method based on a multi-plane stereo target," *Applied Optics*, vol. 58, no. 34, pp. 9353–9359, 2019.

[222] E. Zalnezhad, A. A. Sarhan, and M. Hamdi, "Investigating the effects of hard anodizing parameters on surface hardness of hard anodized aerospace al7075-t6 alloy using fuzzy logic approach for fretting fatigue application," *The International Journal of Advanced Manufacturing Technology*, vol. 68, no. 1, pp. 453–464, 2013.

[223] D. P. Lathrop, J. Fineberg, and H. L. Swinney, "Transition to shear-driven turbulence in Couette-Taylor flow," *Physical Review A*, vol. 46, no. 10, p. 6390, 1992.

[224] D. P. Lathrop, "Turbulent drag and transport in high reynolds number couette-taylor flow," Ph.D. dissertation, The University of Texas at Austin, 1992.